

2

AD-A257 902



PL-TR-92-2178

ANALYSIS OF IMAGES AND SPECTRA OF SPACECRAFT-INDUCED RADIATIONS

D. L. A. Rall  
I. L. Kofsky  
J. A. Gardner, II

PhotoMetrics, Inc.  
4 Arrow Drive  
Woburn, MA 01801-2067

DTIC  
ELECTE  
DEC 7 1992  
S c D

17 July 1992

Scientific Report No. 2

APPROVED FOR PUBLIC RELEASE; DISTRIBUTION UNLIMITED



PHILLIPS LABORATORY  
AIR FORCE MATERIEL COMMAND  
HANSCOM AFB, MASSACHUSETTS 01731-5000



92-30898

**Best  
Available  
Copy**

This technical report has been reviewed and is approved from publication.

  
TERRY L. THIEM, Capt, USAF  
Contract Manager

  
CHARLES P. PIKE, Branch Chief  
Spacecraft Interactions Branch

This document has been reviewed by the ESC Public Affairs Office (PA) and is releasable to the National Technical Information Service (NTIS).

Qualified requestors may obtain additional copies from the Defense Technical Information Center. All others should apply to the National Technical Information Service.

If your address has changed, or you wish to be removed from the mailing list, or if the addressee is no longer employed by your organization, please notify PL/TSI, Hanscom AFB, MA 01731-5000. This will assist us in maintaining a current mailing list.

Do not return this report unless contractual obligations or notices on a specific document requires that it be returned.

| REPORT DOCUMENTATION PAGE   |   |  | Form Approved<br>OMB No 0704-0188    |  |
|---|---|--|--------------------------------------|--|
| Public reporting burden for this collection of information is estimated to average 1 hour per response, including the time for reviewing instructions, searching existing data sources, gathering and maintaining the data needed and completing and reviewing the collection of information. Send comments regarding this burden estimate or any other aspect of this collection of information, including suggestions for reducing this burden to Washington Headquarters Services, Directorate for Information Operations and Reports, 1215 Jefferson Davis Highway, Suite 1204, Arlington, VA 22202-4302, and to the Office of Management and Budget, Paperwork Reduction Project (0704-0188), Washington, DC 20503.  |   |  |                                      |  |
| 1. AGENCY USE ONLY (Leave blank)  | 2. REPORT DATE<br>17 July 1992                              | 3. REPORT TYPE AND DATES COVERED<br>Scientific Report No. 2            |                                      |  |
| 4. TITLE AND SUBTITLE<br>Analysis of Images and Spectra of Spacecraft-Induced Radiations  |   | 5. FUNDING NUMBERS<br>PE 621C1F<br>PR 7601 TR 30 WVCP                  |                                      |  |
| 6. AUTHOR(S)<br>D. L. A. Rall<br>I. I. Kofsky<br>J. A. Gardner, II  |   | Contract No.<br>F19628-91-C-0061                                       |                                      |  |
| 7. PERFORMING ORGANIZATION NAME(S) AND ADDRESS(ES)<br>PhotoMetrics, Inc.<br>4 Arrow Drive<br>Woburn, MA 01801-2067  |   | 8. PERFORMING ORGANIZATION<br>REPORT NUMBER                            |                                      |  |
| 9. SPONSORING/MONITORING AGENCY NAME(S) AND ADDRESS(ES)<br>Phillips Laboratory<br>Hanscom AFB, MA 01731-5000<br><br>Contract Manager: Capt. Terry Thiem/WSSI  |   | 10. SPONSORING/MONITORING<br>AGENCY REPORT NUMBER<br><br>PL-TR-91-2178 |                                      |  |
| 11. SUPPLEMENTARY NOTES   |   |  |                                      |  |
| 12a. DISTRIBUTION/AVAILABILITY STATEMENT<br><br>APPROVED FOR PUBLIC RELEASE: DISTRIBUTION UNLIMITED   |   |  | 12b. DISTRIBUTION CODE               |  |
| 13. ABSTRACT (Maximum 200 words)<br><br>The visible and short wavelength infrared emissions excited from the ~110-km altitude atmosphere by the exhaust of solid composite rocket motors of the Bow Shock 2 Experiment (18 Feb 1991) are analyzed and interpreted, and assistance with laboratory measurements of the excitative reactions with ionospheric species of gases from space vehicle operations is reported. A ~10 s-persisting visible wake trail with relatively stable geometry photographed from the 350 km distant Air Force Maui Optical Site is found to be produced by chemiluminescent reactions of a minor Al atom-containing combustion product molecule with ambient oxygen atoms. The much shorter-lived and smaller-volume but several orders of magnitude brighter expanding SWIR glow that Phillips Laboratory/WSSI imaged with a PtSi-photocathode camera at AMOS is identified as the high temperature contact surface with swept-out air of the posigrade-directed thruster exhaust gas. The development of both emitting regions is found to be reasonably well predicted by similarity hydrodynamics for static explosions in the high atmosphere. Absolute optical radiance distributions and yields, and prescriptions for scaling to other exhaust energy deposition rates and altitudes, are presented. |   |  |                                      |  |
| 14. SUBJECT TERMS<br>Rocket exhaust reactions<br>Solid propellant thruster engines<br>Spacecraft contamination  |   |  | 15. NUMBER OF PAGES<br>84            |  |
| Bow Shocks<br>Infrared radiometry<br>Chemical kinetics<br>Video photometry  |   |  | 16. PRICE CODE                       |  |
| 17. SECURITY CLASSIFICATION<br>OF REPORT<br>UNCLASSIFIED  | 18. SECURITY CLASSIFICATION<br>OF THIS PAGE<br>UNCLASSIFIED | 19. SECURITY CLASSIFICATION<br>OF ABSTRACT<br>UNCLASSIFIED             | 20. LIMITATION OF<br>ABSTRACT<br>SAR |  |

## FOREWORD

This report covers the principal tasks performed in the first year of USAF Phillips Laboratory/Weapons and Survivability Directorate contract F19628-91-C-0065, for analysis of spacecraft imagery and related optical measurements (Sections 1 and 2) and laboratory research in ion-neutral reactions (Section 3). Recent previous PhotoMetrics investigations of the foregrounds contaminating remote sensing from spaceborne platforms (in particular space shuttle), in conjunction with the Spacecraft Interactions Branch (WSSI) of PL, appear in contract-report References 1 - 4 and journal-literature References 5 - 7 (among others).

Section 1 is a detailed analysis and scaling of the persisting visible radiation that was produced when the energetic combustion gases from solid composite-propellant rocket motors interacted with the -110 km atmosphere. The interpretation draws heavily on experience from experiments involving releases of chemicals at thermospheric altitudes that had been performed by Weapons and Survivability's predecessor organizations. This material is currently under review by PL for journal submission. Section 2 reports and interprets the short wavelength-infrared radiation that develops when this supersonic-velocity gas is reheated in its "bow shock" or contact surface with the atmosphere. These two chemically-unrelated emissions, which represent targets for surveillance as well as optical contamination, appear not to have been previously characterized. Section 3 reports measurements of ionic-reaction cross-sections of spacecraft exhaust and outgas species.

Several other tasks, some still in progress and others reported informally (in memorandums), were also performed. A paper on planning for further experimental investigation of the phenomenology of high vapor pressure liquids released into the low orbital environment was presented at a technical meeting (Ref 8), and a paper on the infrared-foreground implications of ventings of water was prepared for a forthcoming conference. An Interim Technical Report in PL format (25 pp, not yet assigned an identifying number) was submitted on the infrared radiations from Shuttle Orbiter control rocket exhaust gases, as measured from onboard by USAF's Infrared Background Survey Spectrometer. We also contributed to forthcoming WSSI journal publications on the spectrum of visible radiations excited from the atmosphere by energetic rocket exhaust, and to those referenced in Section 3.

Mrs. Natalie Bennett was responsible for typing and editing the manuscript. Some of the image data reduction was performed by D. B. Kenny and D. F. Frohman. Valuable assistance was provided by our PhotoMetrics colleagues R. C. Garner, P. J. McNicholl, and C. A. Trowbridge, by M. A. MacLeod of PI/GP and A. Setayesh of Radex, Inc. The authors gratefully acknowledge the encouragement and technical leadership of WSSI staff members E. Murad, D. J. Knecht, R. A. Viereck, C. P. Pike, and Capt T. Thiem.

Class For  
UNCLASS  
TAG  
downed  
collection

|                |            |
|----------------|------------|
| Distribution/  |            |
| Availability 0 |            |
| Dist           | Avail and/ |
|                | Special    |
| A-1            |            |

# TABLE OF CONTENTS

|  | <u>PAGE</u> |
|--|-------------|
| FOREWORD   | iii         |
| LIST OF FIGURES  | v           |
| LIST OF TABLES   | vii         |
| <u>SECTION</u>   |             |
| 1    VISIBLE RADIATION FROM INTERACTION OF THE<br>EXHAUST GASES FROM SOLID-PROPELLANT ROCKETS<br>WITH THE ATMOSPHERE | 1           |
| Introduction   | 1           |
| Experiment   | 1           |
| Overview of the Video Data   | 5           |
| Data Reduction   | 9           |
| Numerical Results  | 10          |
| Antares Burn Period  | 10          |
| Antares After-Burn   | 16          |
| Star-27  | 18          |
| Interpretation of the Luminosity   | 19          |
| Excitation Mechanism   | 19          |
| Exhaust Transport and Scaling  | 20          |
| Chemiluminous Reaction   | 24          |
| Concluding Comments  | 26          |
| 2    INFRARED RADIATION FROM INTERACTION OF THE<br>ROCKET EXHAUST GASES WITH THE ATMOSPHERE                          | 29          |
| Introduction   | 29          |
| Experiment   | 29          |
| Flight Parameters  | 29          |
| Thruster Engine  | 32          |
| Onboard and Spaceborne Optical Sensors   | 37          |
| Infrared Camera  | 38          |
| Visible Light-Sensitive Cameras  | 41          |
| Theoretical Background   | 41          |
| Image Data   | 43          |
| Qualitative Overview   | 43          |
| Reduction-Analysis of a Typical PtSi Camera Frame  | 47          |
| Frames at Other Strypi Velocities-Air Densities  | 52          |
| Interpretation   | 56          |
| Background   | 56          |
| Excitation Processes   | 59          |
| Radiating Species  | 61          |
| Hydrodynamics  | 63          |
| Concluding Comments  | 66          |
| 3    LABORATORY EXPERIMENTS  | 68          |
| Overview   | 68          |
| OH $A^2\Sigma^+ \rightarrow X^2\Pi$ Chemiluminescence  | 68          |
| Reactions of $N_2H_4$ with $O^+$   | 70          |
| REFERENCES   | 73          |

## LIST OF FIGURES

| <u>FIGURE</u> |  | <u>PAGE</u> |
|---------------|--|-------------|
| 1.            | Montage of video photographs of the luminous wake trail left by the Antares rocket engine of Bow Shock 2.  | 2           |
| 2.            | View of the trajectory of the Strypi-XI of Bow Shock 2.  | 4           |
| 3.            | Atmospheric species concentrations and temperature during the experiment.  | 7           |
| 4.            | Crosswise photocurrent profiles 3 s after passage of the Antares thruster engine.  | 10          |
| 5.            | Transverse-summed photocurrent profiles along the long axis of the exhaust trail.  | 11          |
| 6.            | Longitudinal summed-photocurrent profile at 37 s after ignition.   | 12          |
| 7.            | Transverse photocurrent traces across the trail at 35 s after ignition.  | 14          |
| 8.            | Abel inversions of the photocurrent traces in Fig. 7.  | 14          |
| 9.            | Spatially-summed photocurrents in a fixed rectangular image area.  | 15          |
| 10.           | Transverse photocurrent traces across the Antares trail at 108.2 km altitude.  | 15          |
| 11.           | Equi-photocurrent contour plot of a region of trail image.   | 16          |
| 12.           | a) Photocurrent traces in the Antares smolder area, b) Square of widths at 1/e-maximum photocurrent, c) Total emission rate per unit length.   | 17          |
| 13.           | Transverse photocurrent traces across the Star-27 wake trail.  | 19          |
| 14.           | Spectral response of the sensors used to view the Antares trail compared with the spectrum of emission from the reaction of methyl aluminum with atomic oxygen.  | 26          |
| 15.           | Typical photocurrent-contoured PtSi CCD images of the outer glow and alumina-particulate exhaust from the Strypi-XI thruster engines and intensified video photographs of this particle cloud and the persisting wake trail. | 30          |
| 16.           | Composite infrared and visible-light AMOS photograph of Star 27 Frame E, with other radiances measured during engine operation.  | 31          |
| 17.           | View of the trajectory of the Star 27 engine burn.   | 33          |

## LIST OF FIGURES (continued)

| <u>FIGURE</u>  | <u>PAGE</u> |
|--|-------------|
| 18. Strypi-XI flight parameters during the Star 27 burn.   | 33          |
| 19. Star 27 engine thrust profile.   | 34          |
| 20. Angles between the long axis and trajectory direction of the Strypi-XI during Star 27 operation.   | 34          |
| 21. Densities of atmospheric species during the Bow Shock 2 experiment.  | 35          |
| 22. Elevation view of the Strypi-XI body and pointing of optical sensors.  | 35          |
| 23. a) Intrinsic spectral response of the PtSi photodetector and transmission of the atmosphere above AMOS. b) Camera system sensitivity.  | 39          |
| 24. Photocurrents in scans perpendicular to the symmetry axis of the outer glow in Frame E.  | 45          |
| 25. a) Position, b) Magnitude of the low-altitude side radiance maxima in Frame E.   | 46          |
| 26. Manual overlay of the radiance maxima in Frames B - F.   | 48          |
| 27. Lateral displacements of the radiance maxima from the symmetry axis of the particulate exhaust.  | 49          |
| 28. Lateral displacement of the radiance maxima from the symmetry axis of the outer infrared glow.   | 50          |
| 29. Transverse scans of Frames A - F at 75 m behind the exhaust exit plane.  | 51          |
| 30. Maximum SWIR radiances at 75 m retrograde distance.  | 53          |
| 31. Transverse displacement of the radiance maxima from the symmetry axis at 0.015 s after passage of the Strypi-XI plotted against the similarity-theoretical expansion radius. | 54          |
| 32. Angles of the maximum radiance line as a function of Mach number.  | 54          |
| 33. Response of the PtSi camera system to two of the candidate vibrational bands.  | 62          |
| 34. Distance to radiance minima compared with theoretical predictions.   | 65          |



## LIST OF FIGURES (concluded)

| <u>FIGURE</u> |   | <u>PAGE</u> |
|---------------|---|-------------|
| 35.           | Dependence of rotational temperature on collision energy in simulation of the OH A $\rightarrow$ X chemiluminescence spectra.   | 69          |
| 36.           | Energy dependence of the reaction cross sections for production of $\text{N}_2\text{H}_3^+$ and $\text{N}_2\text{H}_4^+$ in reactions of $\text{O}^+$ and $\text{CO}_2^+$ with $\text{N}_2\text{H}_4$ . | 71          |
| 37.           | Wavelength dependence of quantum efficiencies of the CCD and OMA detectors.   | 72          |

## LIST OF TABLES

| <u>TABLE</u> |   | <u>PAGE</u> |
|--------------|---|-------------|
| 1.           | Strypi-XI trajectory parameters.  | 4           |
| 2.           | Characteristics of the ANTARES II rocket engine.  | 6           |
| 3.           | Star 27 trajectory parameters.  | 36          |
| 4.           | Candidate infrared radiation-producing exhaust molecules.                                       | 58          |
| 5.           | Vibrational excitation coefficients between major exhaust and atmosphere constituents at 2500K. | 60          |

## SECTION 1

### VISIBLE RADIATION FROM INTERACTION OF THE EXHAUST GASES FROM SOLID-PROPELLANT ROCKETS WITH THE ATMOSPHERE

#### Introduction

The Bow Shock 2 or UV Diagnostic Experiment (Ref's 9, 10) of 18 February 1991 was performed primarily to determine the ultraviolet radiation signature of hypersonic-velocity missiles at re-entry altitudes. The second of three propulsion stages was a solid-composite Antares IIa rocket engine that operated over a low-elevation trajectory between 105 and 111 km altitude and then smoldered up to at least 118 km which PL/WSSI photographed with a long focal-length video camera at the ~350 km-distant US Air Force Maui Optical Site (Ref's 1,2,6,7,11). A selfluminous visible trail persisted along the flight path of its Strypi-XI vehicle, representative images are presented in Fig. 1. We report and interpret in this Section the spatial distribution and lifetimes of this reactive-flow volume, which is a potential foreground obscurant to spaceborne optical sensing as well as a surveillance target. Section 2 of this report describes a short wavelength-infrared glow near the suborbital Strypi-XI that is excited by a different chemical process, but nonetheless is physically related to the longer-lived visible (and as we will see, near-UV and -IR) wake trail.

We determined the efficiency with which energy of the thruster engine is converted to  $\sim 0.4 - 0.7 \mu\text{m}$  photons by photometrically calibrating the electronically intensified camera against known stars. The measured (absolute) brightness distributions are consistent with the interpretation that the persisting radiation is chemiluminescence from reactions of minor Al atom-containing species in the combustion-product gas with O atoms of the ambient lower thermosphere; the liquid/solid  $\text{Al}_2\text{O}_3$  particles, which are well known to dominate the infrared signature of the exhaust of aluminized thrusters (see for example Ref's 12,13), play no part. A similar selfluminous trail, whose hydrodynamics scales satisfactorily to that from the Antares, was left by the lower-power third stage solid rocket motor, and indeed this long-lived emission may be a general feature of heterogeneous composite propellants based on aluminum granule fuel and ammonium perchlorate oxidizer traversing the oxygen atom-rich altitudes of the atmosphere.

#### Experiment

Figure 2 shows schematically the flight path of the Strypi-XI relative to the mountaintop camera station (AMOS; 20.71°N, 156.26°W; 3050 m altitude; 394 km from the launch site), and Table 1 lists its altitude and velocity, elevation-azimuth and slant range, and



angle between trajectory vector and line of sight during the Antares burn and smolder periods. (Further particulars of the flight, which apply primarily to analysis of the above-mentioned infrared glow, appear in Section 2; the shallow minimum in aspect near 165 s after launch is due to curvature of the vehicle track in the horizontal direction.) The ranges in Table 1 indicate that the image scale in the montage of Fig. 1 is monotonically decreasing (by 14%) during the 35.4 s-duration burn, and in addition changes in right ascension on the camera's astronomical mount have the effect of shifting the apparent direction of the trajectory. A non-standard tracking method was devised by the AMOS staff to enable the Acquisition Telescope System (AATS) finder for the main "MOTIF" 1.6 m telescope to operate at the unusually high zenith angles of the flight path. This f/5, 15-cm clear aperture video camera has a 40 mm-diameter Intensified Silicon Intensifier Target photodetector with S-20R spectral sensitivity (FWHM response is  $3800\text{-}\text{\AA}$ ). Its  $3.0^\circ$ -diagonal field was fixed on the initial segment of the trail until 16 s after the Antares ignited, and then was tracked to keep the overexposed image volume near the rocket in view; refer to Fig. 1.

The Strypi-XI was launched at an azimuth of  $202^\circ$  from the USAF's Kauai (Hawaii) Test Facility ( $22.07^\circ\text{N}$ ,  $159.75^\circ\text{W}$ ) at 14:18:35.0 UT (03:18:35 local standard time), with the moon below the horizon; refer to Fig. 2. After its first-(Castor) stage booster burned out near 40 km altitude, it coasted at a high elevation angle as it was being reoriented so that its second stage, which ignited at 105.2 km - 155.1 s after launch, produced a trajectory azimuth near  $143^\circ$  (toward the southeast). This flight path resulted in  $35^\circ$  -  $40^\circ$  nose-on view aspect angles from Maui during the Antares burn, which increased to  $\sim 55^\circ$  during its smolder period. For this report of the emissions produced by its exhaust we measure times starting at this engine turnon. The spin rate about the long axis of the vehicle was 0.7 revolutions/s, and its angle of attack rapidly decreased from  $66^\circ$  at ignition to  $25^\circ$  10 s later and then to  $12^\circ$  in another 10 s, after which this angle decreased slowly to  $8^\circ$  at burnout.

After another  $48\frac{1}{2}$  s a third-stage "Star 27" (Morton-Thiokol TE-M-616) solid-composite rocket motor with approximately  $\frac{1}{4}$  as much thrust (particulars are in Section 2) propelled the Strypi-XI generally downward from 119 km. The broadly similar formulation of this engine (whose binder is carboxy-terminated polybutadiene, and whose calculated mole fractions of combustion products are given in Table 4 of Section 2) also left a persisting glow tangential to the trajectory, less bright and with sensibly uniform diameter even near the ignition altitude; an example image is in later Fig. 15. Although the velocity across the camera field of the precisely-tracked and -centered vehicle was then too high for reliable determination of decay times, radiance distributions transverse to the trajectory such as those shown in Fig. 13 could be readily measured. The Star 27 thruster, whose power output is intermediate between the

Table 1. Strypi-XI trajectory parameters

| Time [s]                | Range [km] <sup>a</sup> | Alt [km] | el [deg] <sup>a</sup> | az [deg] <sup>a</sup> | [ km s <sup>-1</sup> ] <sup>b</sup> | aspect [deg] <sup>a</sup> |
|-------------------------|-------------------------|----------|-----------------------|-----------------------|-------------------------------------|---------------------------|
| 140.0                   | 476.4                   | 102.4    | 8.1                   | 292.2                 | 0.371                               | 50.2                      |
| 150.0                   | 457.6                   | 104.4    | 9.4                   | 290.0                 | 0.317                               | 43.1                      |
| 155.1-0 <sup>c</sup>    | 448.4                   | 105.2    | 10.1                  | 290.0                 | 0.310                               | 38.9                      |
| 160.0                   | 439.2                   | 105.8    | 10.7                  | 289.2                 | 0.391                               | 35.1                      |
| 165.0                   | 430.1                   | 106.1    | 11.4                  | 288.4                 | 0.618                               | 34.4                      |
| 170.0                   | 421.2                   | 106.7    | 12.1                  | 287.5                 | 0.904                               | 35.1                      |
| 175.0                   | 412.3                   | 107.5    | 12.7                  | 286.6                 | 1.250                               | 35.4                      |
| 180.0                   | 403.5                   | 108.2    | 13.4                  | 285.6                 | 1.618                               | 36.8                      |
| 185.0                   | 394.8                   | 109.3    | 14.0                  | 284.5                 | 2.050                               | 37.8                      |
| 190.5-35.4 <sup>c</sup> | 386.2                   | 110.9    | 14.6                  | 283.6                 | 2.567                               | 39.3                      |
| 195.0                   | 377.7                   | 112.5    | 15.3                  | 282.5                 | 2.634                               | 40.7                      |
| 205.0 <sup>d</sup>      | 361.1                   | 115.3    | 16.5                  | 280.0                 | 2.621                               | 43.7                      |
| 215.0                   | 344.9                   | 117.3    | 17.6                  | 277.4                 | 2.610                               | 47.0                      |
| 225.0                   | 329.4                   | 118.2    | 18.7                  | 274.4                 | 2.600                               | 50.9                      |
| 235.0                   | 314.5                   | 118.8    | 19.6                  | 271.1                 | 2.606                               | 55.2                      |
| 239.0 <sup>e</sup>      | 308.8                   | 118.8    | 19.9                  | 269.7                 | 2.616                               | 57.7                      |
| 245 <sup>f</sup>        | 300.4                   | 118.4    | 20.4                  | 267.4                 | 2.836                               | 61.6                      |

<sup>a</sup>From AMOS

<sup>b</sup>Scalar speed of the Strypi-XI

<sup>c</sup>Antares ignition and burnout

<sup>d</sup>After-burn, Fig. 12

<sup>e</sup>Star 27 engine ignition

<sup>f</sup>Star 27, Fig. 13 and Section 2

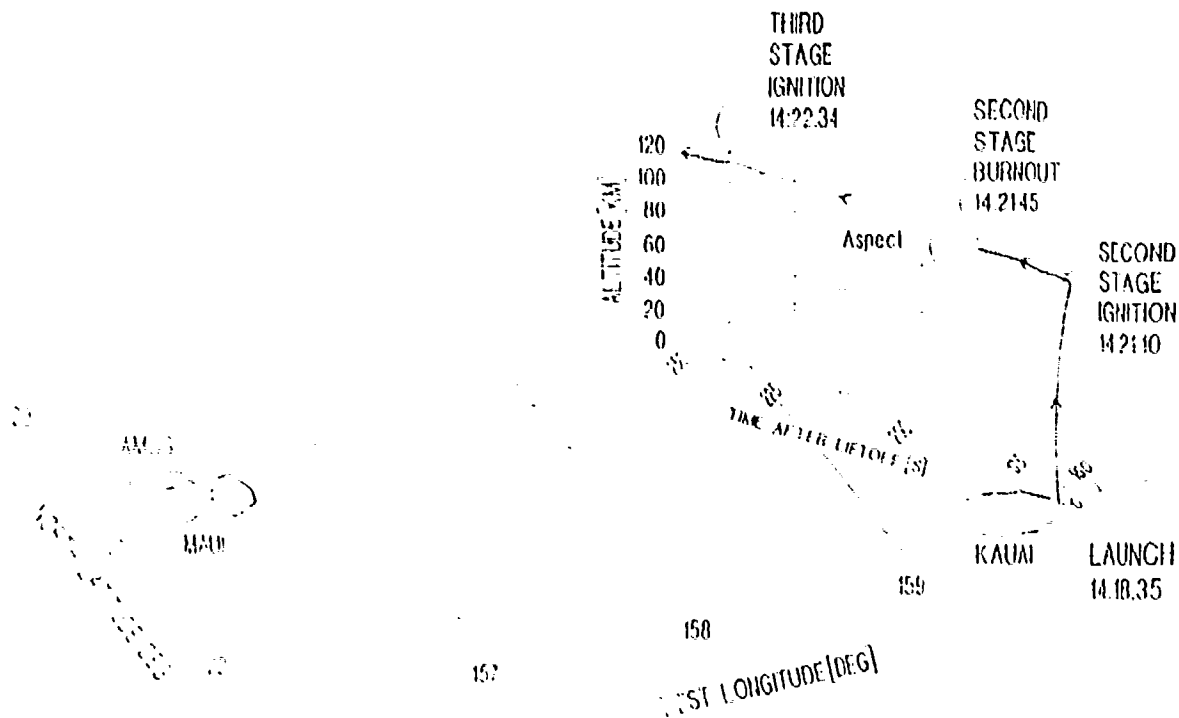


Figure 2. South-looking view of the trajectory of the Strypi-XI with the projection from AMOS.

operating and nominally burned-out Antares, thus represents a third sample in the exhaust data set.

Table 2 lists the physical, chemical, and performance properties of the Antares IIa (Hercules X259A2) engine. Its propellant grain is poured around a central cylindrical gap with 60°-120° X-shaped slots parallel to its containing wall. Actual thrust reached 90% of rating value within  $< 1/3$  s after ignition, then after this usually-observed initial transient decreased 15% by 1.6 s, then went back up to a flat 9800-kgf maximum near 18 s, and then had decreased 10% by 31 s. (Since the variations in this engine thrust do not qualitatively alter the visible wake glow, we have not reproduced its measured profile; it is similar to that of the Star 27 shown in Fig. 19.) Experience with other aluminized-solid formulations has shown that in addition to the major gaseous components listed in Table 2 measurable amounts of Al and  $\text{Al}_2\text{O}_3$ ,  $\text{AlCl}$  and  $\text{AlCl}_3$ , and OH vapor, as well as trace amounts of other gases, may be exhausted (Ref 14). Furthermore, some of these low-concentration molecules can be expected to be hydrated or weakly chemically bonded to other exhaust species.

Figure 3 is a plot of the kinetic temperature and densities of atomic oxygen and all atmospheric species over the altitude range at which the engine burned and smoldered, derived from an MSIS calculation (Ref 15) for the geophysical conditions of the Bow Shock 2/UV Diagnostic Experiment (minor lower-thermospheric species are shown in Fig. 18). The predicted concentration of the reactive  $\text{O}(^3\text{P})$  atoms varies by less than a factor of 2 over the Antares operation period. As the order of 1 m collision mean free paths at these lower-thermosphere altitudes are much less than the characteristic dimensions of the radiating volumes, continuum flow conditions obtain.

The persisting trail of the Antares burn was also photographed in ~15 km-long segments from the Naval Research Laboratory's "LACE" satellite (Ref 16), by an intensified charge-coupled device "tracker" camera with a relatively flat spectral response between 3000 and 4400Å and extending to 2500 and 4500Å (and thus overlapping that of the AMOS system). Other ("plume") cameras onboard sensitive in narrower wavelength spans below 3400Å failed to detect this glow; and furthermore the signal from the Antares smolder appears to be below all thresholds. The LACE images released so far provide principally corroboration of the data we have extracted from the higher spatial resolution groundbased visible-light images, and we will refer to the information contained in them in our analysis.

### Overview of the Video Data

The instrumentally-bloomed area at the head of the wake trail is the thermally-radiating microns-scale  $\text{Al}_2\text{O}_3$  particles of the rocket exhaust (the nozzle cone opening to the bright engine combustion volume itself is directed away from the AMOS sensors). Its shape is

Table 2. Characteristics of the ANTARES II (X259A6) rocket engine

**a) Dimensions<sup>a</sup>**

|                                |          |
|--------------------------------|----------|
| Length (including exit cone)   | 289 cm   |
| Diameter                       | 76.5 cm  |
| Diameter of throat             | 16.94 cm |
| Half-angle of nozzle exit cone | 15°      |

**b) Propellant<sup>a</sup>**

|   |               |
|---|---------------|
| Weight (0.91 of total thruster motor)   | 1167 kg       |
| Composition, nominal weight percent   |               |
| Al, <i>fuel</i>   | 20.6          |
| Ammonium perchlorate, <i>oxidizer</i>   | 7.5           |
| Cyclotetramethylnetetranitramine, <i>oxidizer</i> , HMX                             | 15.0          |
| Nitrocellulose, <i>oxidizer-binder</i>  | 22.5          |
| Nitroglycerine, <i>oxidizer-plasticizer</i>   | 26.3          |
| Triacetin, resorcinol, and 2-Nitro-diphenylamine, <i>plasticizer and stabilizer</i> | 8.1           |
| Heat of explosion (calculated)  | 1642 cal/g    |
| Grain segment pattern   | 2 × 120°, 60° |

**c) Exhaust (calculated)<sup>a</sup>**

|  |                                   |                  |       |
|--|-----------------------------------|------------------|-------|
| Temperature (chamber)                      | 3756K                             |                  |       |
| Temperature (exit plane)                   | 2139K                             |                  |       |
| Average mass outflow rate                  | 33.3 kg/s                         |                  |       |
| Mean molecular weight of gases             | 19.7 g/mole                       |                  |       |
| Molecule exhaustion rate                   | 2½ x 10 <sup>21</sup> per cm path |                  |       |
| Composition, moles/100 g of propellant     |                                   |                  |       |
| Al <sub>2</sub> O <sub>3</sub> (particles) | 0.367                             | H <sub>2</sub> O | 0.171 |
| CO   | 1.392                             | HCl              | 0.060 |
| H <sub>2</sub>                             | 0.985                             | CO <sub>2</sub>  | 0.043 |
| N <sub>2</sub>                             | 0.513                             | H                | 0.018 |

AlCl<sub>3</sub>, AlCl, AlO, Al<sub>2</sub>O, OH,... *See text*

**d) Performance (see text for further details)**

|  |                        |
|--|------------------------|
| Duration of burn                                       | 35 s                   |
| Average thrust (measured, to 35.0 s)                   | 9370 kgf               |
| Exhaust velocity (calculated as thrust/mass loss rate) | 2.65 km/s <sup>b</sup> |

<sup>a</sup>Manufacturer's data: Hercules, Inc., Cumberland, MD, 1966, and Ref 12.

<sup>b</sup>Calculated (Ref 12); compare the rocket velocities in Table 1.

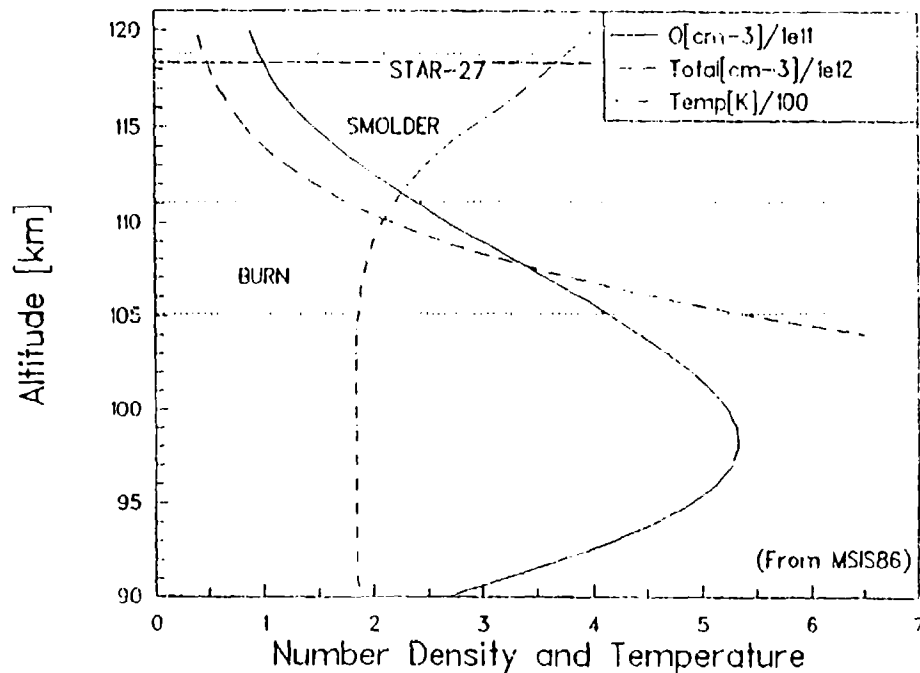


Figure 3. Atmospheric species concentrations and temperature during the Bow Shock 2/UV Diagnostic Experiment.

apparent in the infrared and other visible images in Fig. 15. This feature can be seen to break away from the broader glowing glow area in the video frame at 35-11/30 s after ignition; while its apparent diameter is decreasing, it remains larger than the instrumentally-smeared "image" of a sixth-magnitude star and saturated near its center when it goes out of the corner of the field of view at 27/30 s after; and no intensification at the head of the luminous trail from this particulate is detectable when the Strypi-XI comes back into the field after another 3-28/30 s after. When camera pointing was changed after 16 s from staring to viewing the rocket body (albeit not precisely tracking it), the luminous regions in the earlier images go below the camera field.

The persisting trail itself can be seen in Fig. 1 to consist of 1) a highly irregular area that develops within 1 s after engine ignition, followed by 2) a smooth region that is bifurcated and shows strong limb-brightening up to at least 14 s. After about 25 s, when the camera re-acquired the Strypi-XI, this latter volume takes on 3) a somewhat "billowed" longitudinal structure with sensibly constant 1.2-km width along its ~25 m length within the image field. The surface radiance of the initially-produced rough volume varies over a range of almost a factor 3, with no single characteristic cell size (at least in this view projection). It shows some evidence of initially rotating about the trajectory direction--most probably due to the rotation of the Strypi-XI-- and its maximum width perpendicular to the trajectory increases by only a



factor about two (to 5 km) between 2 and 16 s. A lower-edge "finger" also about  $1\frac{1}{2}$  km across and with a mean velocity of  $300 \pm 50$  m/s extends to 5 km down the retrograde trajectory direction from this initial volume. This protuberance is also brightened along its outer borders, and furthermore gives the impression of breaking into two overlying quasicylinders.

While the initial radial expansion rate of the luminous column cannot be accurately measured from these video images because of blooming from the hot exhaust particles, a rough estimate of 4 km/s can be made from the less-exposed frames near thruster burnout. (This important issue treated in Section 2; see in particular Fig's. 27 and 28.) No overshoot or oscillation of this hard-edged volume can be detected at the spatial and temporal resolution of the photographs, and as shown later its width changes little at later times. The very rapid initial outward expansion is strong evidence that the persisting luminosity is due to gases rather than related to the condensed aluminum oxide exhaust droplets, which besides thermally radiating at visible wavelengths in the  $\ll 1$  s before they cool (see the narrow camera field image in Fig. 15) could in principle be serving as recombination surfaces for the exhaust gas species. These particles would not undergo so large a lateral scattering in  $< 1$  s, or pile into an irregular volume part of which moves backward along the trajectory at near the velocity of sound at the Antares altitude, nor would they move coherently horizontally at a typical E-region wind speed, as the luminous trail is seen to do in the -25 - 37 s video images. Indeed, both simple aerodynamic drag arguments and a computational fluid dynamical model of the two components of the exhaust flow (Ref 12) show that the condensed particles travel largely unimpeded from the  $\pm 15^\circ$  engine exhaust cone.

The initial optical yield rates per unit rocket path during the  $> 40$  s-long after-burn period (final two frames in Fig. 1) are between one and two orders of magnitude lower than those from engine operation. In contrast to the glow that is produced during firings, this smaller-radius (and higher-altitude) volume becomes noticeably broader within a few s. A more or less regular-appearing longitudinal variation of initial width during this period is most probably due to the azimuthal asymmetry of smolder-exhaust flow as the vehicle, whose angle of attack is then between  $10^\circ$  and  $15^\circ$  (Fig. 20), rotates about its long axis; however this spatial structure is not sufficiently distinct to allow a reliable period to be extracted. Similarly, as mentioned just above, the longitudinal radiances in the original video images of the trail between -25 and 35 s show a weak modulation near the Strypi-XI, with the 1 - 2 km characteristic length that would be associated with its rotation. These low-contrast, poorly-defined cells give the appearance of remaining stationary (an estimated upper limit to their retrograde velocity is 300 m/s).

### Data Reduction

To compensate for discrete manual adjustments of the gain of the intensified AMOS camera that were made while the thruster was firing (as in its previous operation, Ref's 2,6,7), we calibrated separately sets of frames against the photocurrents from stars of known magnitude and spectral class. The irradiances within the FWHM response of the camera from individual stars that we identified from standard charts and the SkyMap listing (Ref 17) were corrected for the small attenuation by the atmosphere above AMOS by the method in (for example) Ref's 1 and 6. We digitized the photocurrents from the analog videotape to eight bits (these numbers are labeled PV--pixel value--in some of the Figures), and then summed these currents above the dark-noise baseline in the instrument-spread "images" of the calibrating point sources. The effective halfwidths of these blur spots serve to convert the irradiance distribution at the focal plane from each star to its equivalent peak "radiance" in object space, to which the output currents in the images of the exhaust are referenced. The absolute radiances outside the atmosphere (in Fig.'s 9 and 11) refer to the 3800-6700Å photon FWHM of the camera system. Their estimated overall accuracy, taking into account the difference in spectral distributions from the ~6000K blackbody calibration sources and the glow (whose emission spectrum, while not measured, is probably the continuum described later), possible nonlinearity of the AMOS camera's response, and uncertainties from attenuation by aerosols along the low elevation angle sight path above the mountaintop optical station, is  $\pm$  a factor  $2\frac{1}{2}$ .

We determined the dependence of the optical yield rates on time after the Antares exhaust was deposited by measuring both their decrease in successive video frames at a fixed position in space (to the extent allowed by the data) and in single frames at a series of down-trail--retrograde--positions that correspond to times at which the thruster had passed. The first measurement refers to a single narrow altitude range, while the second averages over altitude. In the static frame of reference of the atmosphere the mass of combustion products exhausted per unit length remains constant within the error of the video measurements, at an average of 8 g of gases/m. Furthermore, the longitudinal transport of this material does not change substantially with altitude, as evidenced by the nearly constant cross-track extent of the trail and the aforementioned slow (if any) downstream motion of its low-contrast internal structure. Thus the space rate of deposition of exhaust reactant(s) is an almost stationary factor in the process that excites visible radiation.

### Numerical Results

**Antares Burn Period.** Figure 4 is a set of transverse profiles of the gain-standardized photocurrents (averaged over six adjoining longitudinal pixels to improve signal/noise) at 3.0 s after passage of the Antares, at altitudes between 105.8 and 110.9 km. The uncertainty in absolute radiometric calibration at each of the individual video gain settings precludes quantitative intercomparison of the total yield rates per unit length along the trajectory (the area under these curves). Figure 5 is a series of summed photocurrents from transverse profiles at a fixed gain (i.e., area integrals of traces such as those of Fig. 4 at the same ratio of radiance to photocurrent), over a 3-3/8 s time span after the engine had turned off. The

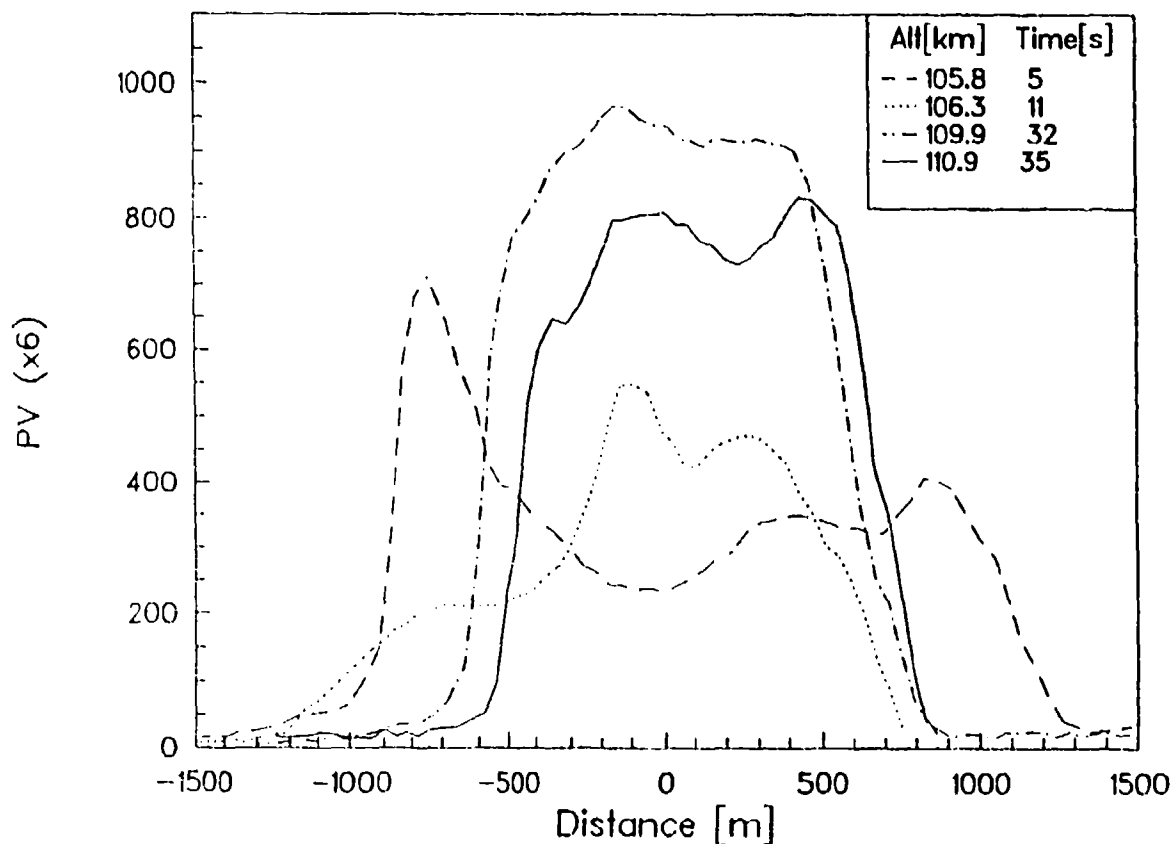


Figure 4. Crosswise photocurrent (pixel value PV) profiles 3 s after passage of the Antares thruster engine, normalized to fixed camera gain. The times stated refer to this passage. Representative trace lines are indicated on the images at 8 and 14 s (referring to 5 and 11 s in the Figure) in Fig. 1.

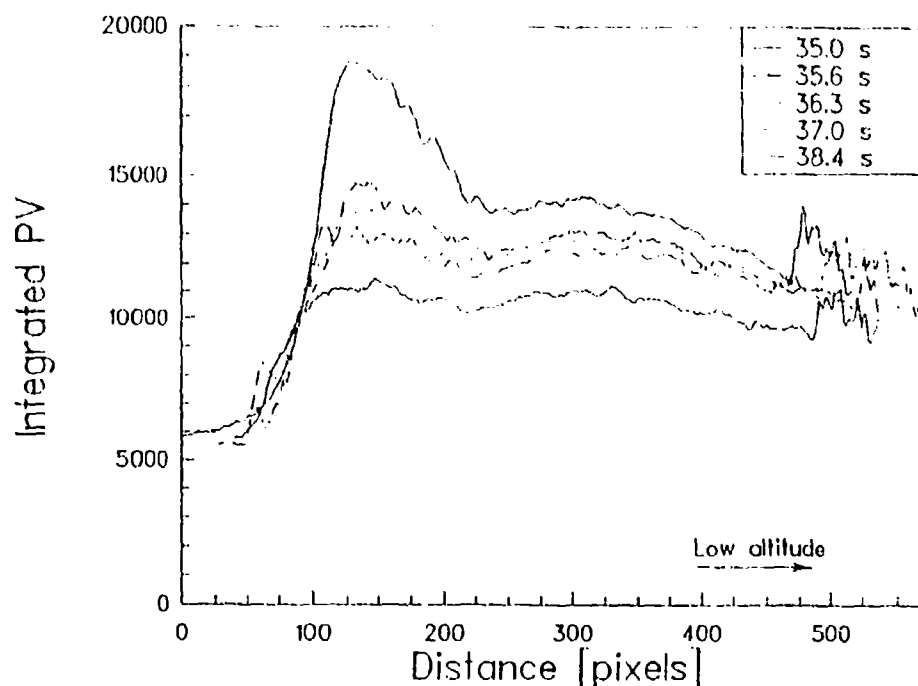


Figure 5. Transverse-summed photocurrent profiles along the long axis of the exhaust trail, starting near engine shutoff. The broad peak in the image at 35 s is thermal radiation from the exhausted  $\text{Al}_2\text{O}_3$  particles.

emission rates can be seen to decrease with time at each retrograde position considered, which is to say, at all altitudes along this segment of trail. Figure 6 first corrects the crosswise-integrated photocurrents at 2 s after burnout for the monotonically increasing velocity of the rocket--placing them on a time-since-deposition scale--, and then normalizes this output signal to the undisturbed concentration of atomic oxygen--applying the hypothesis that O is the rate-limiting factor in chemiluminescence of the exhaust gas (more on this critical point below). The thus-interpreted decrease in output current is exponential within the resolution of the measurements, with an e-folding time between 11 and 15 s. (These low signal/noise data can of course be fit by other functional forms, including even a straight line.)

This derived time represents the mean characteristic decay period of the total visible-light yield rate per unit length over the 108 to 111-km altitude range, in the first ~14 s after passage of the thruster. Since, as we will show, physical transport of the reactants plays an important part in the luminescence process, this figure is not a chemical-reaction or exhaust molecule-depletion, or peak surface brightness-decay time. Furthermore this characteristic time would be expected to decrease as the exhaust volume becomes more intermixed with the ambient atmospheric gas as it ages. A similar reduction-analysis of the summed radiances from traces across the trail at 35 s at five previous deposition times up to 13.3 s (those in

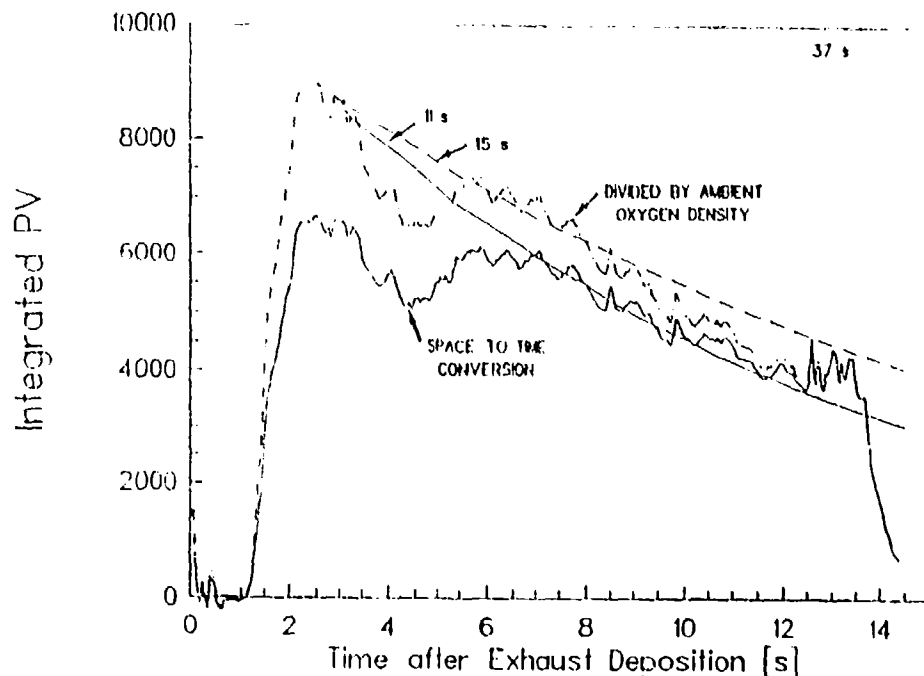


Figure 6. Longitudinal summed-photocurrent profile at 37 s corrected to derive an effective exponential lifetime of the total emission rate per unit path averaged over 108.2 - 110.9 km altitude.

Fig. 7) gave a best-fit exponential time constant of 13 s, consistent with the result in the paragraph above from the frame 2 s later. Figure 8 shows the volume emission rates derived from these crosswise profiles as described below.

We also determined this initial decay time at a narrow span of altitudes, by staring at the series of images recorded between 35 and 38 s. Figure 9 shows the resulting sums of photocurrents in the rectangular area indicated in Fig. 1, which bounds  $108.2 \pm 0.2$  km. The least-squares best fit exponential slope of these yield rates is 13 s. This agreement with the result for the wider range of altitudes (in Fig. 6) gives credence to our normalization of the emission to the concentration of atomic oxygen, and thus to the idea that O--or another atmospheric species with a similar scale height--is participating in the reaction(s) that produce the visible luminosity.

At 8 s after exhaust is deposited the visible-light power radiated near 108.2 km altitude is 6 kilowatts per km along the trajectory. With the approximation that the fractional decrease rate remains exponential at  $1/13 \text{ s}^{-1}$  this figure leads to a total light output of 140 kilojoules/km. This optical yield may be compared with the total energy of the thruster, 10,000 megajoules expended over about 50 km flight path  $\approx 200,000$  kilojoules/km. Thus the efficiency with which the chemical energy of the solid propellant is converted to visible

photons at this altitude--albeit through what we are interpreting to be a reaction of its combustion product(s) with a labile species in the atmosphere--is 0.07%.

The series of image scale-corrected photocurrent traces across a single photograph between 5.2 and 13.3 s after exhaust is deposited in Fig. 7 shows little difference in the projected widths of the radiating volume. (These times also represent a range of atmospheric altitudes.) Figure 10 plots the similar transverse radiances at the fixed altitude 108.2 km over a 3½-s period; again the video data fail to resolve a significant change in width of the visible afterglow. To assess the transverse growth in the absence of chemical consumption we applied a simple transport-only model in which the laterally-expanded exhaust gas interdiffuses with ambient air that it has initially compressed and heated (Ref 18), as is further described below. Adoption of an effective diffusion coefficient 2 - 3 times that for the undisturbed atmosphere at 108 km which is,  $2 \times 10^6 \text{ cm}^2/\text{s}$  (Ref 19), leads to the prediction that the widths would increase by about 250 m in 8 s or 170 m in 3½ s. The fact that the volume from which glow arises is expanding at a substantially slower rate--if at all--is evidence that the concentration of exhaust reactant(s) is being eroded at a much greater than  $1/13 \text{ s}^{-1}$  fractional rate where it contacts the swept-out, overdense local air.

The coherent movement of the luminous region relative to stars observed in the video images (not discernible in Fig. 1) corresponds to a horizontal velocity of 70 m/s in the direction perpendicular to the camera line of sight (azimuth 285°). This figure is within the normal range of atmospheric wind speeds at the Antares altitude. This transport further emphasizes that the radiation is coming from a gas rather than -microns particles, which would not follow the wind field. Since a star shows through the glow volume (see Fig. 11), it must be optically thin over at least part of the visible wavelength range.

The relatively flat tops of the transverse traces in Figs. 7 and 10 show that the visible emission is arising principally from near the outer edges of the image-producing volume, which we interpret as being essentially cylindrical on the basis of the single camera projection and simple growth-symmetry arguments. This limb enhancement is quantitatively evidenced by the emission rates per unit volume in Fig. 8, which we derived from Abel inversions of the set of radiances at 35 s. The inversion procedure applies the physically reasonable assumption that these rates depend only on radial distance from a symmetry axis in half-cylinders on either side of the plane defined by the lines of sight from the camera through this axis (and that the volume is optically thin to its own radiation). Since Abel inversion involves differencing, noise in Fig. 7 is amplified in Fig. 8, so that the depths of the troughs and the widths of the edge regions are inexact. Figure 11 is an isophote contour plot that includes one of the 1-D scans that were inverted, with an absolute radiometric calibration from the procedure described above.

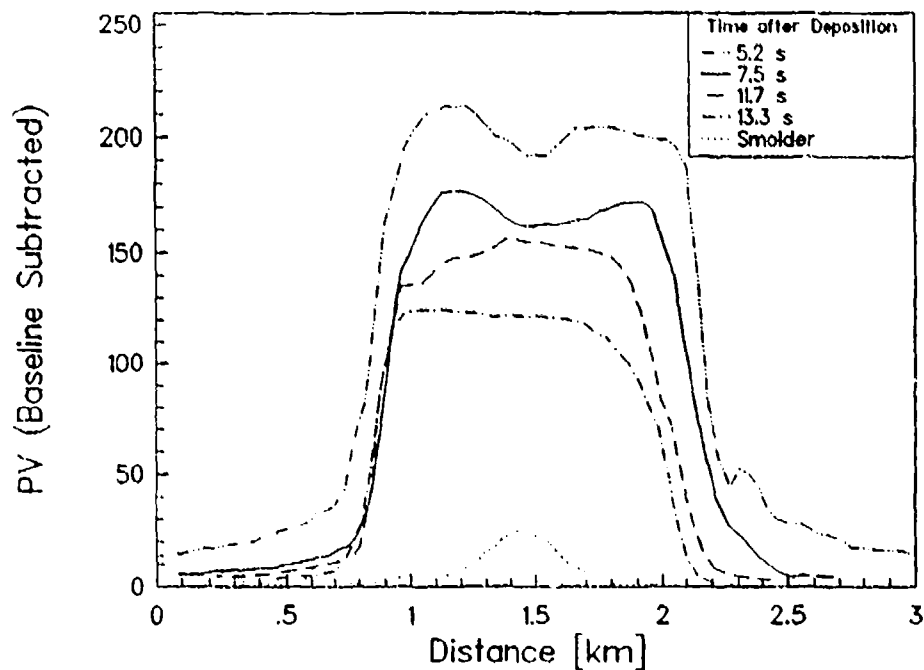


Figure 7. Transverse photocurrent traces across the trail at 35 s.

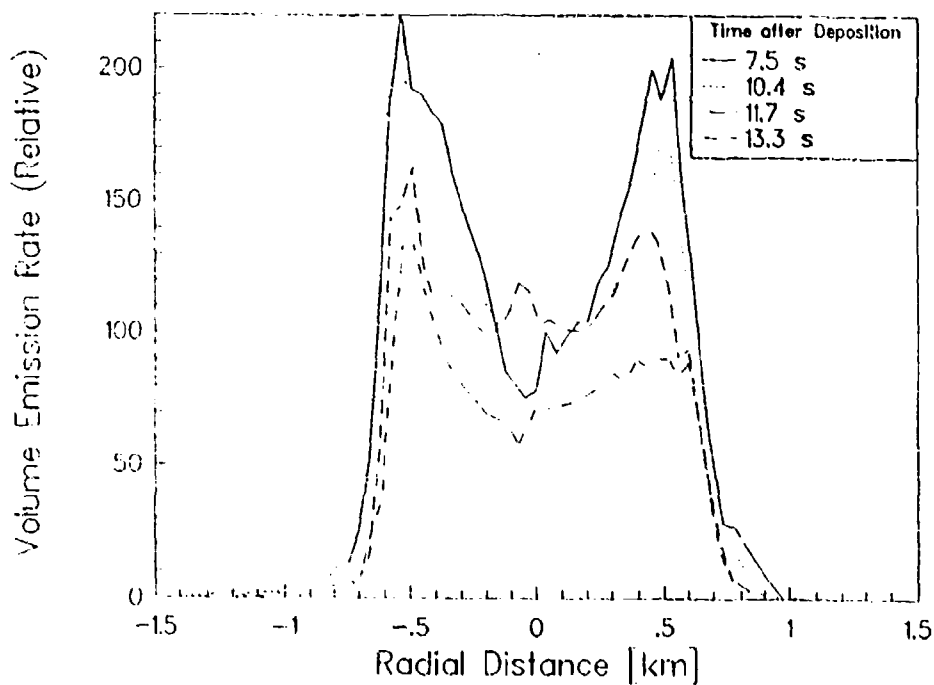


Figure 8. Abel inversions of the photocurrent traces in Fig. 7.

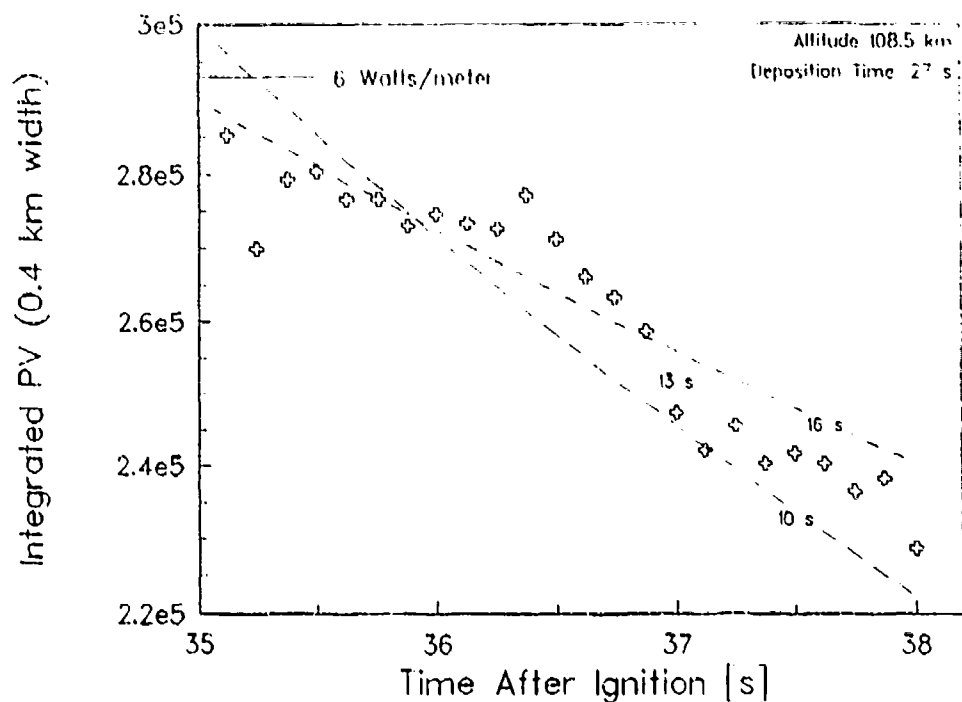


Figure 9. Spatially-summed photocurrents in the fixed rectangular image area near the bottom of the trail indicated in Fig. 1 (altitude range  $108.4 \pm 0.2$  km), with exponential lifetimes indicated.

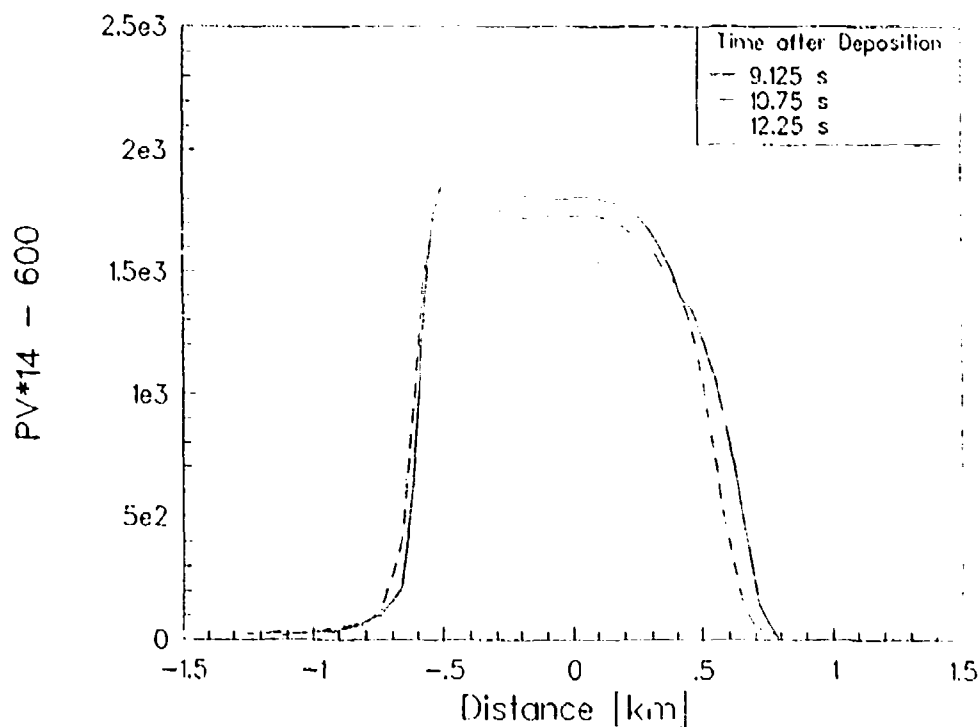


Figure 10. Transverse photocurrent traces across the Antares trail at 108.2 km altitude at three times after exhaust is deposited.



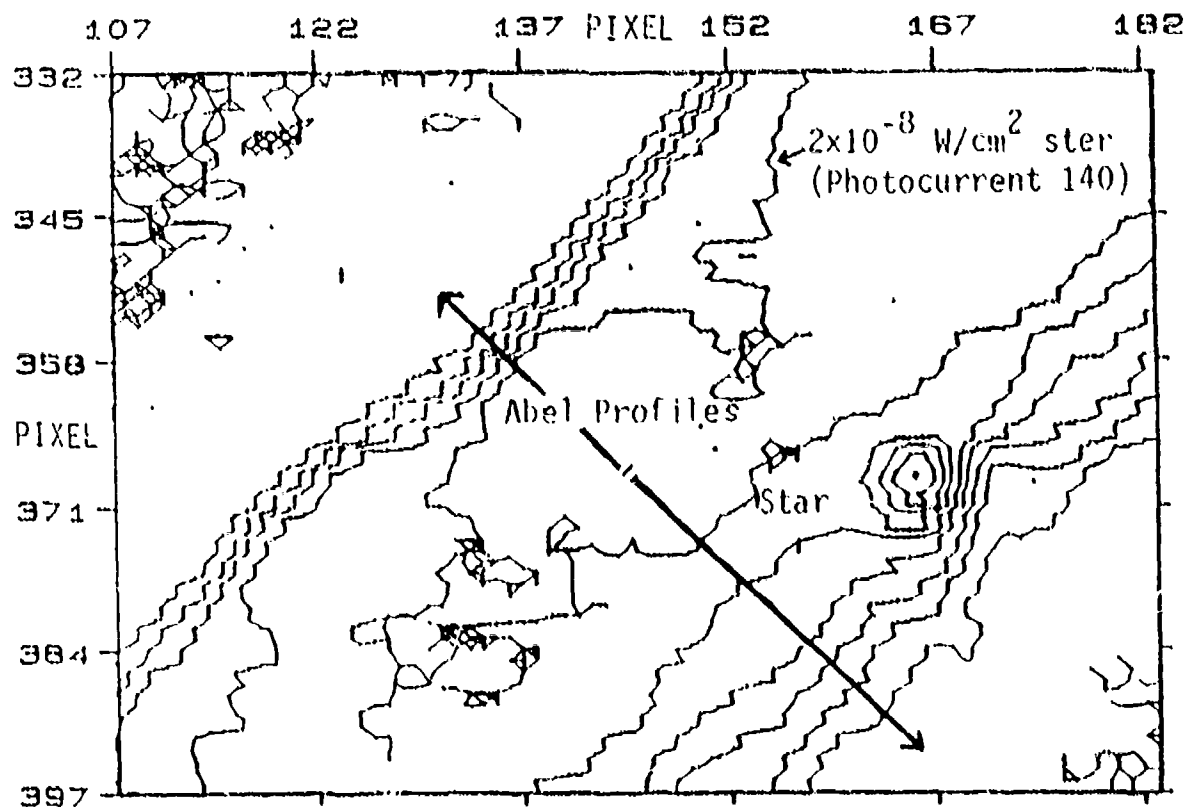


Figure 11. Equi-photocurrent contour plot of the region of image within the rectangular area centered at 108.4 km, at 37 s. The (linear) contour interval is 20 photocurrent units.

Limb brightening is also obvious in both the irregular and relatively-smooth radiating regions that develop before 16 s; refer again to Fig. 1. As the exhaust trail ages, the surface brightnesses (in Figs. 7 and 10) exhibit less spatial modulation, and in addition its high volume emission rate outer annular regions (in Fig. 8) broaden and flatten. This damping/smoothing is expected from the diffusion lengths estimated just above, which would be of the same order within the exhaust gas as where it is mixing with the air that it has displaced.

**Antares After-Burn.** A similar analysis of the luminosity associated with smolder of the Antares engine is summarized in Fig. 12. Using a bright star on each side of the trail as position references (refer to the 49-s frame in Fig. 1), we were able to stare for 3 s at a fixed 0.5 km-long segment of this glow centered at 114.5 km altitude. The radiating region appears Gaussian-shaped even at the earliest times after rocket passage, with a characteristic width that increases with  $(\text{time})^{1/2}$ . Applying the theory of a reacting (or inert) species diffusing into a uniform, isothermal, undepleted atmosphere (Ref 20), we find that the slope of the plot in Fig. 12b leads to a diffusion coefficient of  $9 \pm 2 \times 10^6 \text{ cm}^2/\text{s}$ . This is roughly three times the

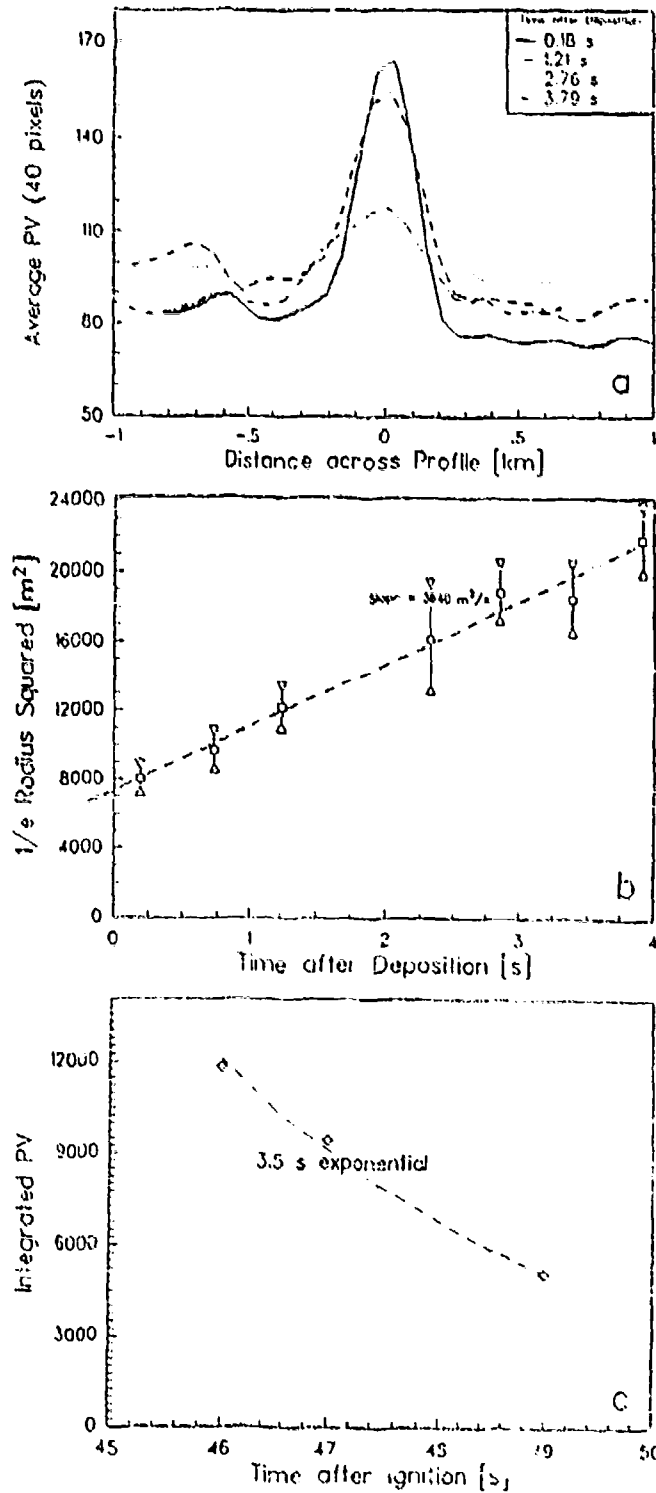


Figure 12. a) Photocurrent traces in the Antares smolder area at 114.5 km. b) Square of widths at  $1/e$ -maximum photocurrents, with least-squares straight line best fit (the triangles represent  $1\sigma$  error from a regression analysis). c) Total emission rate per unit length along the trajectory path.

small-molecule diffusion coefficient in the undisturbed atmosphere (Ref 19), an increase most likely due to the initially high mean temperature of the exhaust gas and surrounding air (Ref's 12,18). An extrapolation to zero time (following the procedure developed for analyzing the growth of chemical-release clouds at thermospheric altitudes, Ref 20) gives an initial Gaussian full width of 0.18 km.

The exponential decay period of the total emission rate per unit length along the trajectory is  $3.5 \pm 1$  s (Fig. 12c). This is about one-quarter of the characteristic time we derived for the afterglow of the thruster burn, despite the concentration of the putative rate-controlling species atomic oxygen being almost a factor 2 lower at 114.5 km than at 108.2 km. This difference is a result of the hydrodynamics of the combustion product gases--the less dense smolder exhaust does not physically displace the local oxygen atoms, but merely intermixes with them--, as we explain in the next subsection.

A comparison of transverse traces in Fig. 7 just before and after the rocket propellant was nominally consumed shows that the exponential decay-corrected rate of emission of visible light per unit path early in the smolder phase is a factor 20 smaller than during engine burn. (While the Antares motor is known to have finite residual thrust during this period, this thrust can not be quantified from the radar tracking of the Strypi-XI or other trajectory data.) As in Fig. 12, which refers to a 3.4-km higher altitude and 12-s later time after burnout, the radiance pattern has an essentially Gaussian shape rather than the hard, ("shock"-like) edge that results from full thruster operation.

**Star 27.** Figure 13 shows three transverse traces from the similar selfluminous trail left by the ~2750-kgf thrust third-stage motor, extending over 0.8 s near 118½ km altitude. (The trajectory of the Strypi-XI is then nearly horizontal, as Fig. 2 shows.) A typical photograph of the glow pattern appears at top left of Fig. 15. As at this time the period during which identifiable emitting segments remain in the camera field is shortened by the increased tangential velocity of the Strypi-XI (see Table 1) and its tracking position being at the center of the video frames, the video data do not allow staring at fixed radiating downstream volumes for long enough to determine reliable decay times. Nonetheless this period appears to be substantially longer than the 3½ s of the lower-altitude (and higher oxygen atom density) glow from the Antares after-burn. As with the Antares operational burn, no lateral growth of the luminous trail is detectable; indeed, its "width" may be decreasing, or even oscillating. Abel inversions of these noisy Star 27 traces show a relatively flat volume emission rate, with some evidence of limb brightening.

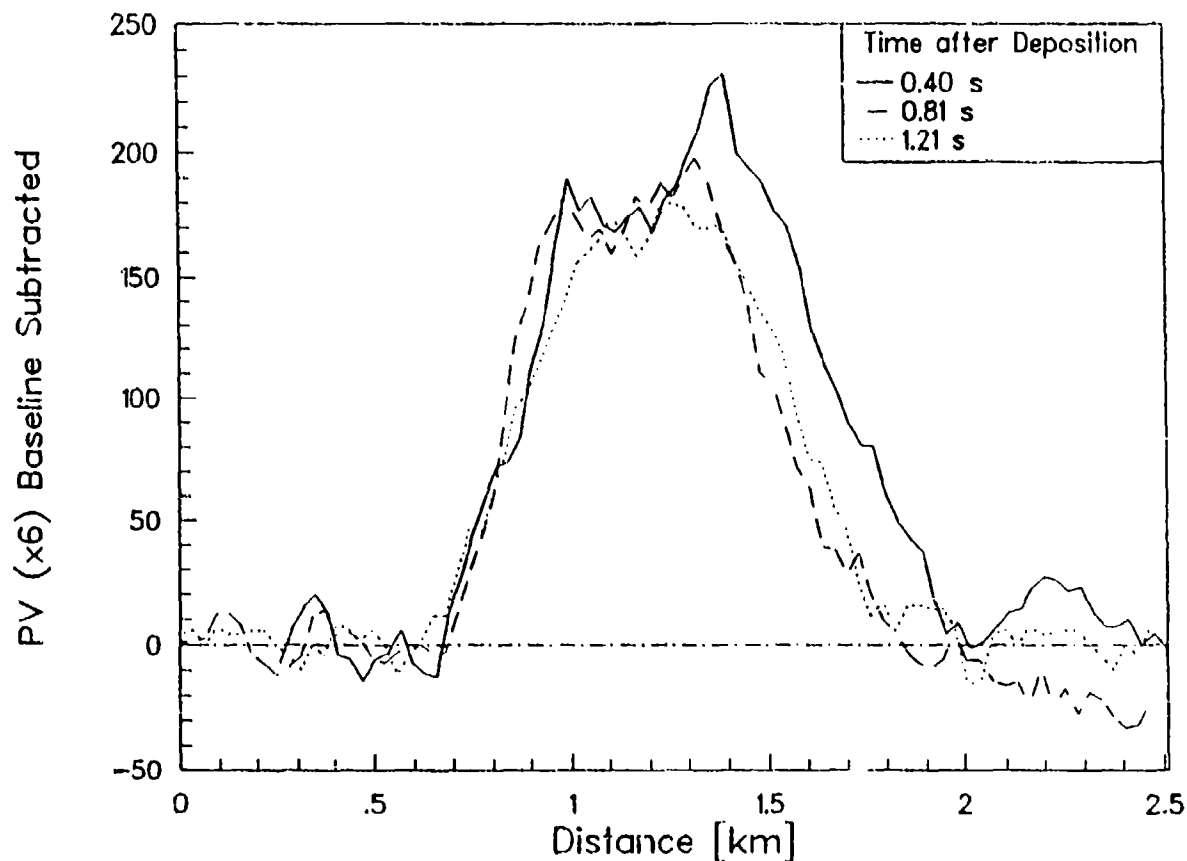


Figure 13. Transverse photocurrent traces across the Star 27 wake trail at three times after exhaust deposition (altitudes 118.6 - 118.4 km).

### Interpretation of the Luminosity

**Excitation Mechanism.** Thermal (gray-body) emission from the microns-scale condensed  $\text{Al}_2\text{O}_3$  exhausted from the rocket motor cannot be responsible for the persisting luminosity, not only for the "geometry" reasons stated above but also because (as straightforward radiative loss calculations show) these droplets cool in only 1/10 s to temperatures at which emission rates of visible photons become negligible. Furthermore, the angular divergence and velocity of such particles (see Fig. 15) preclude the interpretation that their surfaces are serving to catalyze excitative chemical reactions of combustion products with atmospheric species, or among exhaust (or for that matter ambient) gases.

We therefore consider the hypotheses that the radiation is due to homogeneous reactions among exhaust molecules cooled by expansion or, as we have in fact already shown: to agree with observation, of one or more such species with the local atmospheric gas.

Arguing against the first idea are the fact that no chemiluminous reaction is known to proceed at a significant rate at the relatively low temperatures (Ref 18) of the expanded combustion gases after a few s, and that the volume emission rates are highest near the outer edges of such glows where the densities of this gas are much lower than toward their center (Ref's 12,18,21,22). (This latter finding also rules against radiation from a metastable exhaust species.) In consequence we pursue the hypothesis that the luminosity is due to a reaction of a lower-thermospheric component such as the highly labile, abundant  $O(^3P)$  atoms with either one of the major combustion products in Table 2c or exhaust constituents present at lower concentrations.

Excitative reaction of atomic oxygen with an aluminum compound outgassing from smoldering solid-composite propellant has in fact been advanced (Ref 23) to explain the geometrically and temporally similar visible glow produced by a Nike-Hydac engine (Lockheed Propulsion 9.4-KS-10200, 5700 kgf thrust) well after burnout. This booster stage of the "Precede" experiment left a photographable wake trail after it reached ~88 km. (A preliminary analysis of the partially-documented data set suggests that the persistence of the glow depends on the total air density as well as  $[O]$ , that is, that the radiating species is collisionally quenched at the lower excitation altitudes.)

A comparison of the visible-radiance distributions measured at AMOS furthermore implicitly assumes that the spectral distribution of the emission is about the same while both thrusters were operating and during the Antares after-burn, that is, that the excitation process remains the same for the conditions. This assumption is justified if 1) the two solid propellants exhaust the same relative amount(s) of chemiluminescent-reaction species, and 2) the products of smolder are evolved primarily from continuing combustion of pieces of the previously-continuous solid composite (the inner propellant-container lining of fiberglass and buna rubber also slowly "burns").

**Exhaust Transport and Scaling.** To address properly this chemiluminescence issue, information about the spatial distribution of the combustion gases is needed. Guidance is available from standard explosion theory, as well as from numerical calculations of the transport of rocket exhaust gases; Ref 12, for example, refers specifically to the early hydrodynamics of the Antares exhaust (but does not lend itself to heuristic scaling of the flow to later times). Particularly applicable are the similarity solutions for chemical explosions at high altitudes (Ref's 18,24) (which agree with the photographic observations of for example aluminized grenades (Ref 25)), and models of releases of gas from high-velocity spacecraft (Ref 22).

Above a critical ratio of [explosion energy released per unit ambient pressure]<sup>1/3</sup> to [collision mean free path], a Rankine-Hugoniot shock forms; the energetic self-colliding explosion-product gas, whose density and temperature decrease outward, sweeps out (and in doing so heats) virtually all the air in a volume proportional to [energy/pressure]; and the later transport of the explosion and background gases is essentially diffusive. In spherically-symmetric blasts (Ref's 18,26,27) the radius of this initial-scale or pressures-equalization volume, after a few moderate-amplitude oscillations, reaches  $0.21 \cdot [\text{energy/pressure}]^{1/3}$ . As input energy decreases and altitude--i.e., mean free path--increases the shock becomes thicker, increasing the fractional volume of the explosion gas in contact with the atmosphere; and eventually this boundary becomes undefined.

This relatively standard continuum-flow modeling (all flow quantities varying similarly with distance from the explosion, Ref's 18,24,26) has been found to give reasonably accurate predictions of the hydrodynamic growth of chemical--and even nuclear--explosions in the atmosphere. (For example, in experiment "Firefly Jeannie" (Ref 18) 18 kg of cyclotrimethylenetrinitramine ("RDX"-CsNO<sub>3</sub>-Al) was exploded at 108.7 km altitude; this pressures-equalization radius (interpreted as  $1/2\sqrt{2}$  times the stationary width of a decaying Gaussian radiance distribution whose total enclosed area is preserved) was 0.47 km. With the energy released by this explosive taken as the expected 800 cal/g, 0.47 km is in accord with the model prediction. The theory can be extended to transport of the rocket-combustion products by considering the burn as a "line" explosion with cylindrical symmetry (Ref's 27,28). Since the average outward speed at which the initial-scale radius is established exceeds the velocity of the Strypi-XI during the Antares operation and smolder (and also during much of the Star 27 burn), this approach can be expected to be only approximate; that is, the line does not detonate simultaneously everywhere, but the processes also have attributes of a temporal sequence of point (spherically-symmetric) explosions, in part into already-disturbed air.

With this straightforward approach the initial equilibration radius becomes proportional to [energy released per unit length/ambient pressure]<sup>1/2</sup> (Ref's 27,28). Applying this dependence to the Antares exhaust volume between 108.2 and 110.9 km altitude (taking into account the aforementioned measured decrease in engine thrust over this 25- to 30-s burn period), we find that this radius would increase by only about 15%. Such a small change is within the error of definition of the "edges" of the transverse photocurrent traces across the aged trail in Fig. 7, which are being altered by diffusion with simultaneous chemical consumption--and, perhaps more importantly, represent line-of-sight column sums of products of concentrations of the two reactive gases (weighted by a perhaps temperature-dependent rate coefficient) rather than solely of combustion-product molecule concentrations. Similarly the

profiles of the 3 s-old volumes over the broader range of deposition altitudes (in Fig. 4) agree with this simple scaling rule within the accuracy with which they can be measured. (The bifurcated glowing region up to 25 s after ignition, since it stems from the initial azimuthal nonuniformity of the propellant burn pattern--as we hypothesize later--, would not be expected to show the same scaled lateral dimensions.)

More significantly, this scaling applied to the transverse extent of visible glow from the lower-power, higher-altitude Star 27 gives agreement with this average from the late Antares burn. If we interpret the pressure-equilibration radii as the intercepts of lines tangent to the straight segments of the radiance profiles on the dark-current baseline (a plausible definition of the "contact surface" separating the two gases), the observed mean proportionality factors for the Antares averaged over 108.2 - 110.8 km and for the Star 27 at 118.5 km are 0.21<sub>5</sub> and 0.19 respectively. In view of the potential error from this definition of the radius at which the two gases contact and in measuring these positions from the noisy video images, as well as from the model atmosphere and the energy deposition rates along the trajectory (which we took from post-flight rocket thrust profiles), the match can be considered satisfactory. The fact that this experimentally-determined proportionality factor is close to the 0.21 observed from spherically-symmetric blasts (Ref 18) (even when the small correction for the difference in radius increment that produces the same change in gas volume is applied) reinforces the above-mentioned idea that combustion of the rocket propellant exhibits characteristics of a sequence of point shock-producing explosions. This numerical factor should be interpreted only as a heuristic, lumped-parameter figure for scaling the emitting volume.

Extension of this principle to the Antares smolder is hampered by both the energy deposition rates being only approximately known and the fact that the outward distance over which the gas diffuses very quickly becomes comparable with the observed small initial radius (so that this equilibration radius is not well defined experimentally). An estimate of the longitudinal deposition rate, which implicitly assumes that the ratio of engine power output to mass of glow-producing reactant exhausted per second is the same after and before burnout, can be made from the measured visible light emission rates (which are in the ratio 1:20) and decay lifetimes. If we take the radiation time scales to be dominated by chemical consumption in the smolder volume and by fluid-flow from burn, and assume the residual thrust to remain the same at 114.5 km as near 111 km, the energy deposited per unit length at 114.5 km would be closely  $(1/20) \cdot (3.5/13)$  times the average between 108.2 and 110.8 km. Following the procedure for chemical trail releases in the upper atmosphere (Ref 20), we adopt the intercept on the ordinate in Fig. 12b to define the transverse distance at which the pressures equilibrate. The ratio of this radius to  $[\text{smolder energy deposition}/114.5\text{-km air pressure}]^{1/2}$  is then 0.17. (The reasonable agreement of this proportionality factor with that derived for operation of the

solid rocket motors should not be given too much credence, as it is based on a not fully deionizable exhaust energy deposition rate.)

The luminous volume resulting from the much weaker and somewhat higher-altitude "explosion" of smolder almost immediately exhibits a rounded profile because the contact surface with ambient air is many  $\sim 3$ -m collision mean free paths thick (Ref's 21,26); in contrast with the propellant burns, the reservoir of dense exhaust gas near the rocket trajectory almost immediately encounters reactive O atoms. Hence the depletion rate of the chemiluminescence-producing combustion species is greater than when an atmosphere-sweeping-out front develops, in which case chemical consumption must await diffusive intermixing of the two gases. This principle is further supported by the observation by the satellite-borne ultraviolet camera of a several 10's-second (exponential) decay of peak radiance in the large initial exhaust-deposition region (Ref 16), which is in the direction expected from its low ratio of surface to volume.

We ascribe this early-developing irregular luminosity and succeeding few seconds of transversely separated but otherwise relatively smooth glow (refer to Fig. 1) to nonuniform combustion of the Antares propellant. Indeed, the number of discrete-appearing "cells" in the prominent and persisting rough-surfaced region is comparable with the number of points in the cross-section of the propellant grain. (No change in velocity that would lead to a transition from turbulent to laminar flow into the stationary atmosphere is taking place during this initial burn period.) The edges of this region move outward at much less than molecular-diffusion speeds because, like those of the smoother luminescence, they are being chemically eroded. A rudimentary such initial bright patch appears in the video photographs of the Star 27 burn (see Fig. 15), nonuniform in radiance but with about the same diameter as the later-developing exhaust column; presumably, this smaller thruster engine had relatively weaker startup transients.

The rounded finger that extends from the irregular region as a seeming retrograde extension of the early-developing quasicylinder(s) is due to the high-pressure exhaust gas expanding axially into undisturbed air, at or near the sound speed. This gas is confined radially by the background air that it has compressed.

We note that not only would solid-composite motors having other chemical compositions and grain configurations exhibit both different residual thrusts and relative outputs of reactive molecules, but also individual Antares (and Star 27) units would be expected to burn somewhat differently. The hydrodynamic scaling here would apply to the pre- and post-diffusion-period radius of the visible glow for a given spatial rate of energy deposition, and only indirectly addresses the issue of light yields.



**Chemiluminous Reaction.** We look, then, for reaction processes of one or more exhaust species that lead to the following measurements.

1) Lifetime against chemical consumption  $3\frac{1}{2}$  s at 114½ km altitude (where the smolder gases can be considered uniformly mixed with the atmosphere). If the ambient reactant is O, whose concentration is  $2 \times 10^{11}$  atoms  $\text{cm}^{-3}$ , this figure would indicate a bimolecular rate coefficient for disappearance of the exhaust reactant of  $([2 \times 10^{11} \text{ cm}^{-3}] \cdot [3.5 \text{ s}])^{-1} \approx 1\frac{1}{2} \times 10^{-12} \text{ cm}^3 \text{ s}^{-1}$ .

2) Column visible-light emission rates from Antares burn of order  $10^{-8} \text{ W/cm}^2 \text{ sr} \approx 2 \times 10^{11}$  photons/ $\text{cm}^2$ -column s (see Fig. 11). This figure indicates volume emission rates in the outer "annulus" near  $5 \times 10^6$  photons  $\text{cm}^{-3} \text{ s}^{-1}$ .

A further observation, from Ref 16, is

3) Column blue and near-ultraviolet emission rates somewhat less than  $10^{-8} \text{ W/cm}^2 \text{ sr}$ . In view of the higher mean photon energies in this  $<4500\text{\AA}$  wavelength region, the corresponding yield of photons is less than that in the visible region to which the AMOS camera responds.

A further useful input to the analysis is the concentration of all exhaust molecules in the essentially stable, 1.2 km-diameter Antares cylinder (see Table 2c). This concentration initially decreases rapidly with radial distance from the trajectory (Ref 18) and has a mean of  $(2 \times 10^{21} \text{ per cm of trajectory})/(\pi [1.2/2]^2 \text{ km}^2) \approx 8 \times 10^{11} \text{ cm}^{-3}$ .

A review of the chemiluminous reactions of the more abundant combustion products of solid composite motors with oxygen and nitrogen failed to identify any that proceed sufficiently rapidly at the low temperatures reached in the expanded exhaust to agree with these observations. While radiation from  $\text{CO}_2$  ( ${}^1\text{B}_2 \rightarrow \tilde{\text{X}}\text{ }^1\Sigma$ ) results when CO combines with O, this "blue flame" pseudocontinuum is brightest in the near-ultraviolet, and--more important--the rate coefficient for even the non-luminous three-body reaction (Ref 29) falls several orders of magnitude short of producing the volume emission rates measured by both the AMOS and LACE cameras. Similarly the well-known yellow-green glow from recombination to  $\text{NO}_2^*$  can be ruled out because it would require unrealistically large amounts of NO in the exhaust.

In contrast, some small molecules that contain Al atoms are known to react exothermically with oxygen in both the atmosphere (Ref's 25,30) and laboratory (Ref's 31,32) to produce closely-packed electronic bands (they resemble a continuum) that extend from the near-infrared to a short wavelength cutoff just below  $3400\text{\AA}$  (3.7 eV). This limit corresponds to the association energy of AlO molecules with ground-state O atoms to form  $\text{AlO}_2$ . As Fig. 14 shows, the spectral distribution resulting from this process is consistent with the

above-mentioned observation that the wake trail emits more energy at the S-20R wavelengths to which the AMOS camera responds than in the blue and near-UV where the LACE satellite ("tracker") camera is sensitive. (Furthermore the cutoff is to the red of the response region of the inherently less-sensitive LACE "plume" cameras, which as mentioned failed to detect a wake trail from the Antares.)

Radiation with sensibly the same spectrum and persistence ( $\sim 2 - 100$  s) was observed when Al was released between  $\sim 90$  and  $200$  km at night 1) bound in trimethyl aluminum ( $\text{Al}(\text{CH}_3)_3$ ), 2) as a component of  $\text{CsNO}_3$  aluminum-powder burners (which are in effect miniaturized solid composite rocket motors), and 3) contained in explosives (Ref's 25,30). (Control TNT/RDX grenades without Al granules produced no such glow.) In addition, as best as can be determined from the uncalibrated images reported in Ref 23 the exponential lifetime of the aforementioned chemiluminescent wake of the burned-out Nike-Hydrac solid-propellant motor was  $\frac{1}{2}$  s at  $102$  km and  $1$  s at  $108$  km; these are consistent with the  $3\frac{1}{2}$  s "chemical" lifetime that we measured at about a scale height above the latter reaction altitude.

The current conclusion (Ref 32) from these in-atmosphere experiments and supporting laboratory measurements is that the upper state(s) of the transition is excited in a substitution reaction  $\text{XAlO} + \text{O} \rightarrow \text{AlO}_2(^1\text{B}_2) + \text{X}$ . The weakly-coupled adduct X is thought to derive from reaction-generated or rocket-contaminant  $\text{H}_2\text{O}$  (Ref 31) (insofar as the visible glow is prominent in the presence of water vapor). Other candidate reaction-stabilizing species that may be bound to AlO are OH, Cl compounds, H, or even another AlO molecule.

A lower limit to the effective rate coefficient for producing visible radiation from this reaction is  $10^{-13} \text{ cm}^3/\text{s}$  (Ref 32). This figure is as expected less than the  $1\frac{1}{2} \times 10^{-12} \text{ cm}^3/\text{s}$  that we derived from the rate of decrease (in item 1) on p. 24), which refers to the consumption reactions of the trace exhaust species, only some fraction of which would be expected to result in population of excited electronic state(s) of the product. An extrapolation from the visible emission spectrum of  $\text{AlO}_2$  formed by recombination-substitution (and experience with other triatomic oxides) leads to the prediction that an about equal number of photons is emitted in the near infrared; refer to Fig. 14. In addition the AMOS camera also does not respond to the  $\sim 5\%$  (of the total) ultraviolet photons. Thus the ratio of inferred rate coefficient for consumption of XAlO to the rate coefficient for producing photons in the visible wavelength range has an upper limit of somewhat under 10. Combining these figures and those stated above, we find that an upper limit to the mean initial concentration of XAlO in the exhaust "column" is  $2.1 \cdot 10 \cdot (5 \times 10^6 \text{ photons cm}^{-3} \text{ s}^{-1}) \cdot (3.5 \text{ s}) \approx 4 \times 10^8 \text{ cm}^{-3}$ . This approximate figure represents  $5 \times 10^{-4}$  of all the molecules exhausted from the engine, which is in the range expected for "trace" combustion species.

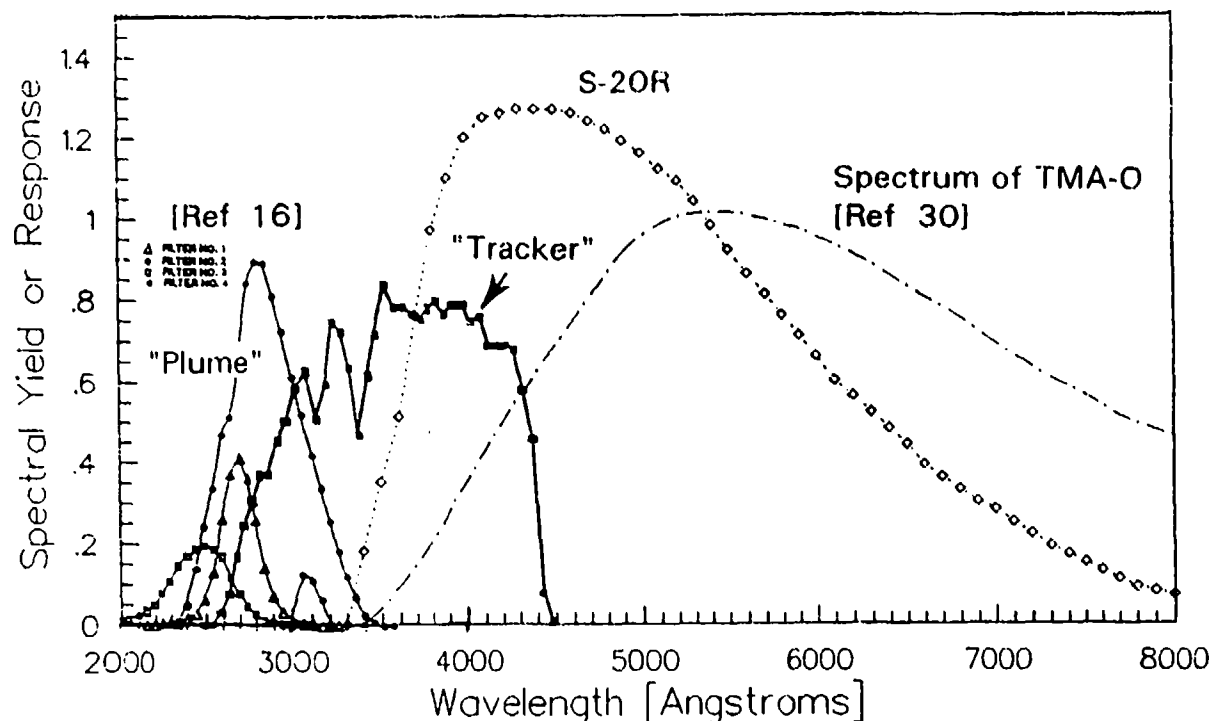


Figure 14. Relative spectral response in photon units of the various instruments used to view the Antares trail compared with the spectrum of emission from the reaction of TMA with atomic oxygen. The S-20R response includes atmospheric transmission from space to AMOS.

Such very low absolute concentrations relative to ambient O (see Fig. 3) show that the luminescence-producing reactant being depleted is  $\text{XAlO}$  (or its precursor). Furthermore the high radiances measured rule against a significant contribution from reactions involving minor atmospheric species (such as  $\text{O}_3$ ). We note also that the resulting concentrations of ground-state  $\text{AlO}_2$  are orders of magnitude too low to make the exhaust volumes optically thick to the multiple overlapping band radiations; the obvious limb brightenings are further evidence that the glow is optically thin (as assumed in this analysis).

### Concluding Comments

Chemiluminescent reactions of an incompletely identified polyatomic minor species in their exhaust gas is the source of the ~10-s persisting visible wake trail from the Strypi-XI solid thrusters as they traverse the oxygen atom-rich lower thermosphere. A similar glow along the trajectory of (at least) one further broadly similar rocket engine has also been photographed, and may be common to aluminum-granule fuel propellants. The light yields would of course depend on the output of the reactant(s) from the high-temperature combustion

(or later reactions among the cooler exhaust gases). For Antares the fractional concentration of this chemiluminous species is less than  $5 \times 10^{-4}$  and the time-integrated energy yield (including that from the near-IR and -UV transitions in the quasicontinuum from  $\text{AlO}_2^*$ ) is 0.15 %, with estimated accuracy  $\pm$  a factor  $2^{1/2}$ .

The lateral dimensions of such glows scale to the power output and pressure altitude of the rocket motor roughly as predicted from "similarity" hydrodynamics of static explosions in the high atmosphere (Ref 18). The surface brightnesses of the trail are controlled by reactive flow of the exhaust gas and the ambient  $\text{O}(^3\text{P})$  atoms, which are pushed out by the exhaust of full engine burn but are almost immediately intermixed with smolder exhaust [at the altitudes of the Bow Shock 2/UV Diagnostic Experiment]. Antares developed a broad, irregular luminous region surrounding the  $\sim 2$  km of its flight path just after ignition (most probably stemming from engine startup transients), and later showed a relatively smooth and stable column along its trajectory (and also extending several km in the retrograde direction). The quite obvious limb enhancements and longer than "chemical" decay times of the surface radiances are due to sweepout of the atmospheric reactant by the denser exhaust gas.

The absolute visible radiances that we measured from AMOS, with the generally lower blue and near-ultraviolet radiances from the spaceborne camera, are consistent with the interpretation that  $\text{AlO}_2(^1\text{B}_2)$  is responsible for the luminosity. A comparable number of  $11\text{-}\mu\text{m}$  asymmetric-stretch ( $\nu_3$ ) cascade photons would also be emitted, since a large fraction of the transitions to the ground electronic state of  $\text{AlO}_2$  terminate on its vibrationally excited states; thus this LWIR radiance component is of order  $2 \times 10^{-10} \text{ W/cm}^2 \text{ sr}$ . However as the rate of pumping of  $\text{AlO}_2^\dagger$  by earthshine and solar radiation is low due to the small oscillator strengths of its vibrational fundamentals (for 001-000,  $\sim 10^{-7}$ ), any persisting infrared background from this minor species would be weak.

The absolute brightnesses and rates of emission per unit axial length indicated in Fig's. 11 and 16 quantify the scene presented by the Antares combustion to surveillance/tracking sensors between  $0.38$  and  $0.67 \mu\text{m}$ , and are a basis for estimates of the accompanying infrared radiant intensities from  $\text{AlO}_2$ . These yield rates initially decrease with exponential lifetimes near  $10 \text{ s}$  at the atmospheric pressures and oxygen atom concentrations of the Strypi-XI. Since they depend on the altitude profile of  $[\text{O}]$ , they would vary with geophysical conditions (and furthermore they may decrease with decreasing altitude due to quenching of  $\text{AlO}_2^*$  by collisions with  $\text{N}_2$ ,  $\text{O}_2$ , and  $\text{O}$ ). This scale time would later decrease, by somewhat less than an order of magnitude, as the emission process becomes dominated by chemical reactions rather than physical transport, as at very early times in the wake trail produced by the Antares after-burn.

The amplitudes and characteristic scale lengths of the fluctuations in visible-near IR radiance of the trail ("clutter") can be directly taken from these AMOS video images, and also lend themselves to extrapolation to longer wavelengths. In addition a straightforward extension of the hydrodynamic calculations applied here would provide the distributions in space and time of density and temperature of the combustion gases, which with their relative concentrations of the several infrared-active molecules in Table 2c leads directly to the thermal spectral radiances of the exhaust volumes. That is, "calibration" of the cylindrical-symmetry reactive flow model from these visible-emission data applies in determining the persisting infrared signature of the trail left by the Strypi-XI (and similar) solid thruster engines.

Rocket experiments over a broader range of exhaust deposition altitudes, with much longer-duration staring and wider field camera views (plus of course measurement of the emission spectrum), would further validate the dependence of the radiance distributions and lifetimes on  $[O]$ , total air density, and thruster power output.

## SECTION 2

### INFRARED RADIATION FROM INTERACTION OF THE ROCKET EXHAUST GASES WITH THE ATMOSPHERE

#### Introduction

The Strypi-XI carrying the Bow Shock 2/UV Diagnostic Experiment produced the short wavelength infrared radiation pattern shown in Fig. 15 (as well the visible wake addressed in Section 1) during its third-stage engine burn, when it reached its highest velocities. PL/WSSI photographed this short-lived glow from AMOS with a long-focus PtSi photodiode array camera separately tracked from the 3°-field video camera that photographed the wake trail. The representative SWIR frames show a feature that gives the initial impression of being shocked air surrounding the substantially brighter cloud of hot alumina particles exhausted from the heterogeneous solid-composite Star 27 thruster then operating. Included for reference in Fig. 15 are images of the visible thermal emission from this droplet trail made with a 3.0° diagonal field video camera coaligned with the infrared imager, and of the less intense but much more widespread and persisting chemiluminescent wake trail from the Star 27 burn. The limb-enhanced outer radiating volume can be seen to be above the threshold of the PtSi remote sensor only when the velocity of the Strypi-XI exceeded 3.3 km/s (at 118½ km altitude) and --in particular--its thruster engine was operating.

We report in this Section the phenomenology and radiance distributions of this outer infrared glow--as we will designate it prior to showing that it indicates the "bow shock" of posigrade-directed rocket exhaust gas--, and interpret how it is excited. That the SWIR emission is related to the much larger wake from primarily-visible chemiluminescence of a component of this gas, rather than due to heating and concomitant changes in state of ambient air associated with the flowfield around the hard Strypi-XI body, is illustrated by the composite photograph from the two coaligned cameras Fig. 16. While the similarity solution for high altitude explosions introduced in Section 1 provides useful physical insight into the interaction of the energetic exhaust gases with the atmosphere, we have limited its application here pending receipt of detailed numerical flowfield calculations specific to the Star 27 firing and trajectory conditions (which in Ref 12 are stated as having been completed).

#### Experiment

Flight Parameters. As mentioned in Section 1, the Strypi-XI assembly consisted of a Castor 1 booster augmented by two small thrusters, Antares IIa second stage (both of which separated after burnout), and Star 27 (Morton Thiokol TE-M-616) third stage. This last metallized solid

MATS Visible 242 s

PtSi Antares 181 s

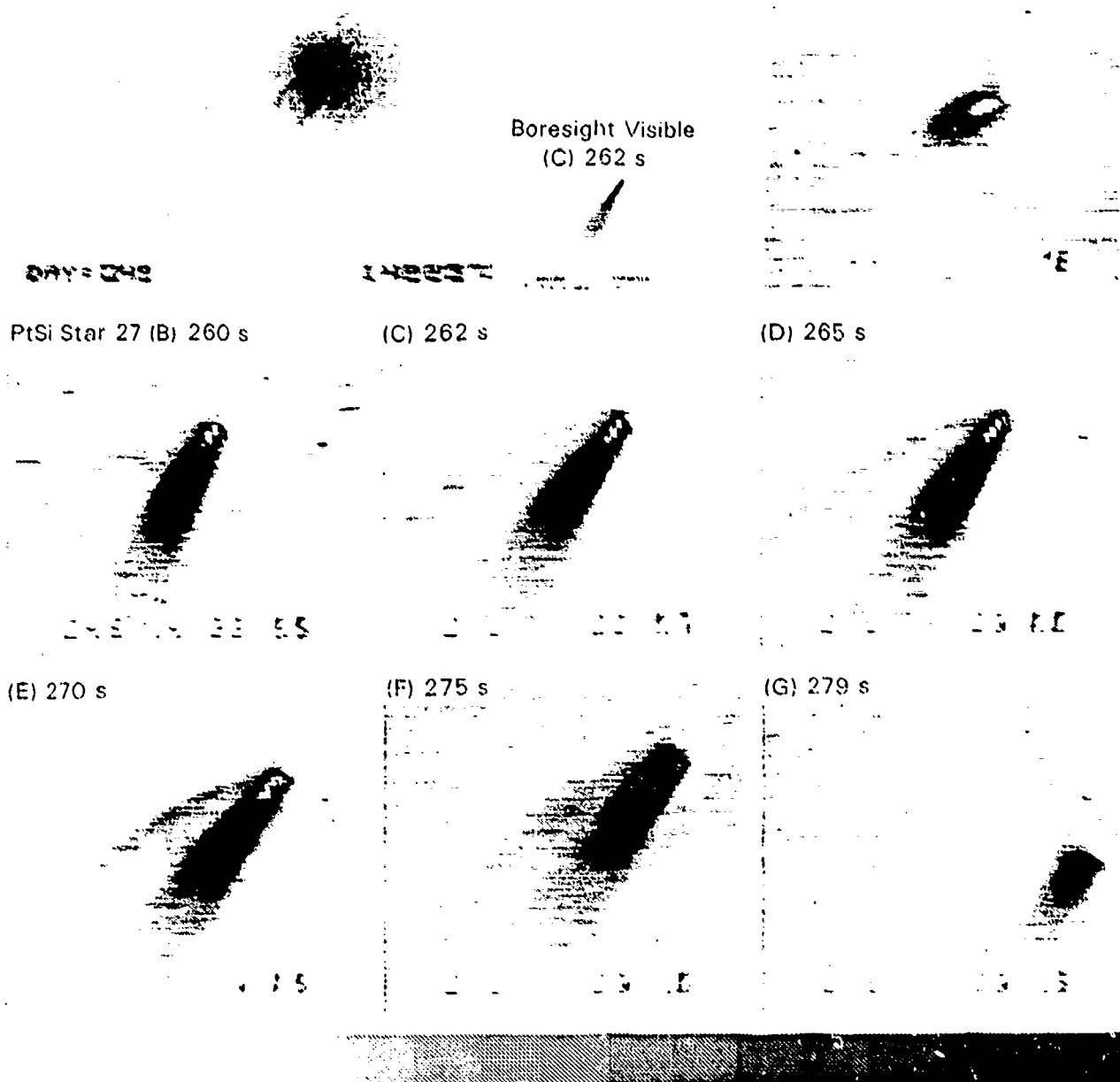


Figure 15. Typical photocurrent-contoured platinum silicide CCD images of the outer glow and alumina-particulate exhaust from the Strypi-XI thruster engines, with intensified video photographs of this particle cloud and (at larger scale and lower radiance threshold) the persisting wake trail. The diagonal field of view of the infrared tracking camera averages 250 m at the range of the trajectory, whose direction is within  $20^\circ$  from normal to the line of sight from the AMOS optical station. Individual frames from the Star 27 burn are identified in Table 3 and Fig's 18 - 21, and the wavelength range of these images is shown in Fig. 23.

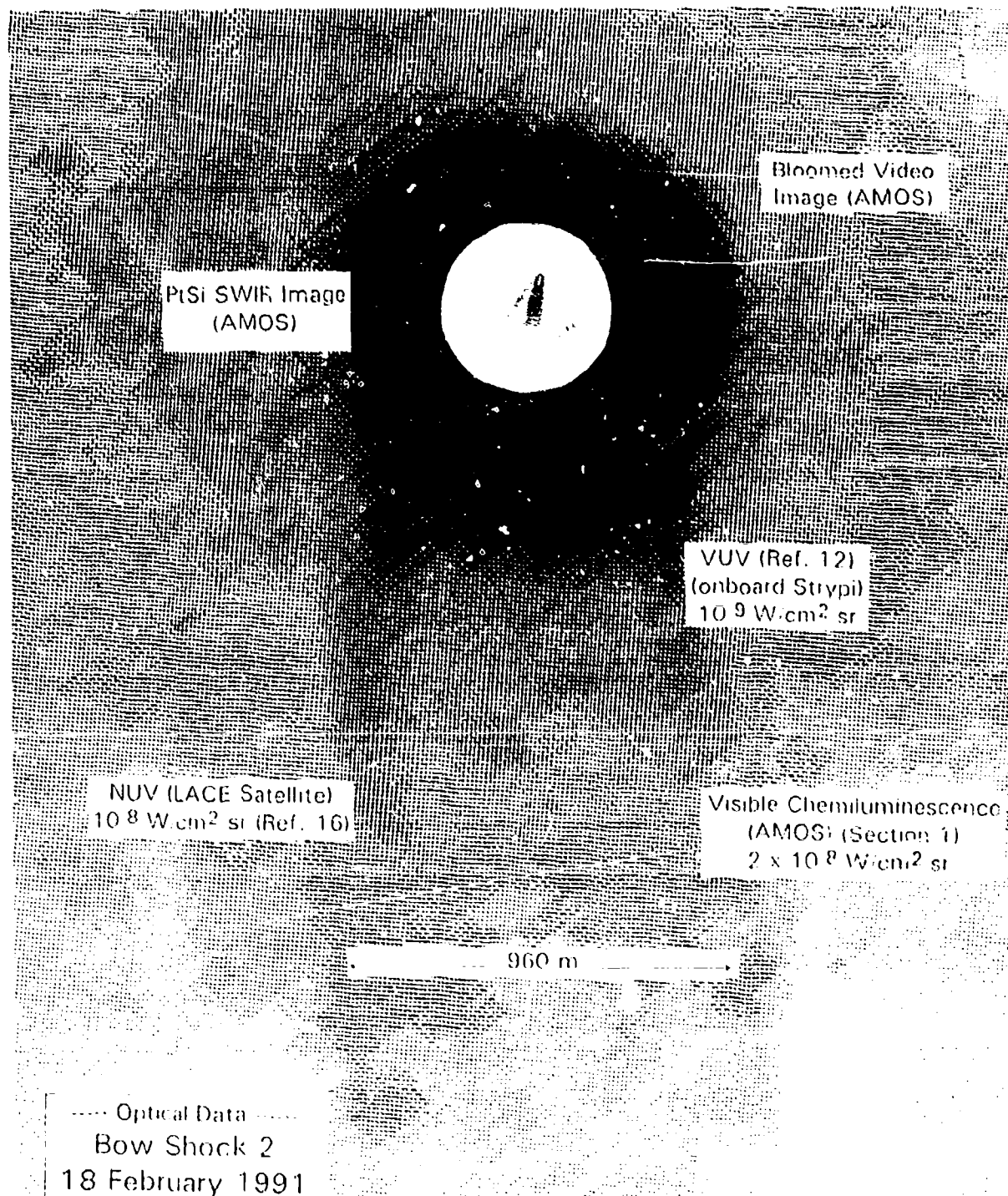


Figure 16. Composite AMOS photograph of Star 27 Frame 1, with visible and ultraviolet (NUV and VUV) radiances measured during operation of the Antares stage. The mean column emission rate from the much larger, limb brightened visible glow region is a factor  $\sim 10^3$  less than that of the outer short wavelength infrared glow excited by the Star 27 exhaust.



rocket motor propelled the vehicle at closely 3° depression angle from 119 km altitude, in a flight path with view projections from AMOS illustrated in Fig. 17 (an extension of Fig. 2). After coasting to 105 km, the Strypi-XI executed an about right angle turn to the southeast that took its powered trajectory between 22° and -8½° from normal to the groundbased PtSi imager's line of sight at elevation angles -19° and range ~250 km during the 22 s that the infrared glow remained above detection threshold.

Figures 18 - 21 and Table 3 are plots and a tabulation of the dependence on altitude (or where more appropriate time after ignition or launch) of experiment parameters that could affect the measured infrared radiance patterns: *Strypi-XI* velocity and Mach number, engine thrust, and pitch/yaw/total angle of attack (the spin rate about its long axis was 1.56 revs/s); *ambient-atmosphere* density, concentrations of oxygen atoms and vibrationally-radiative minor species (expanding on the plot in Fig. 3), and sound speed; and *camera* slant range and view aspect angle to the trajectory (i.e., not to the long axis of the vehicle; see Fig's. 20 and 22). We calculated the primary altitude profiles in Fig. 21 from the MSIS model (Ref 15) for the geophysical conditions of Bow Shock 2 (as in Fig. 3), and took concentrations of the less-abundant nonhomopolar molecules from the literature compilation in Ref 33. The mean free path averaged over ambient species at the 115 km "midrange" altitude of the Star 27, scaled from the U.S. Standard Atmosphere listing to the total air density predicted by MSIS is 2.0 m (Ref 19; this atmosphere model assumes velocity-independent hard sphere collisions, and so may underestimate this important quantity at elevated temperatures); the corresponding averaged diffusion coefficient in the undisturbed atmosphere at 115 km is closely  $10 \times 10^6$  cm<sup>2</sup>/s. Trajectory and related supporting information comes from the post-flight housekeeping data distributed to the Bow Shock 2/UV Diagnostic Experiment participants.

**Thruster Engine.** The Star 27 propellant consists of 72% by weight ammonium perchlorate oxidizer and 16% aluminum-granule fuel in 12% carboxy-terminated polybutadiene binder cured with epoxy resin and MAPO. Its calculated exhaust properties (by engine-performance models that assume thermal equilibrium at the exit plane; see Ref 12) are in later Table 4. Major combustion products are 31% by weight Al<sub>2</sub>O<sub>3</sub> in ~microns-diameter liquid/solid particles and (in decreasing mole fraction) H<sub>2</sub>, CO, H<sub>2</sub>O, HCl, N<sub>2</sub>, and CO<sub>2</sub> molecules; the minor species mentioned in Section 1 (see Table 2) are also expected to be present. A mass flow rate that averaged 9.2 kg/s (including the condensed alumina particles) at 2.93 km/s relative to the engine produced the thrust profile shown in Fig. 19, which was determined by the field support group from the measured acceleration and calculated remaining mass of the Strypi-XI.

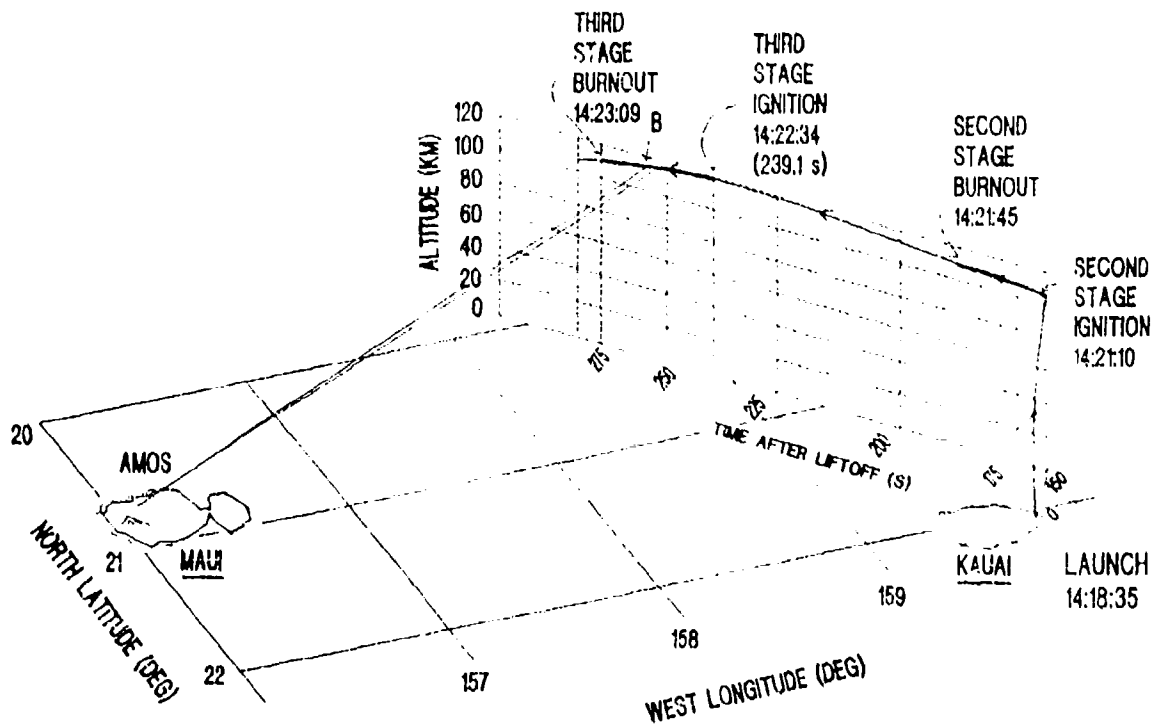


Figure 17. South-looking view of the trajectory in the Bow Shock 2/UV Diagnostic Experiment. (More detailed flight data are in Table 3 and Fig's 18 - 21.) The Star 27 burns at ~100 km closer to AMOS than the Antares (see Fig. 2).

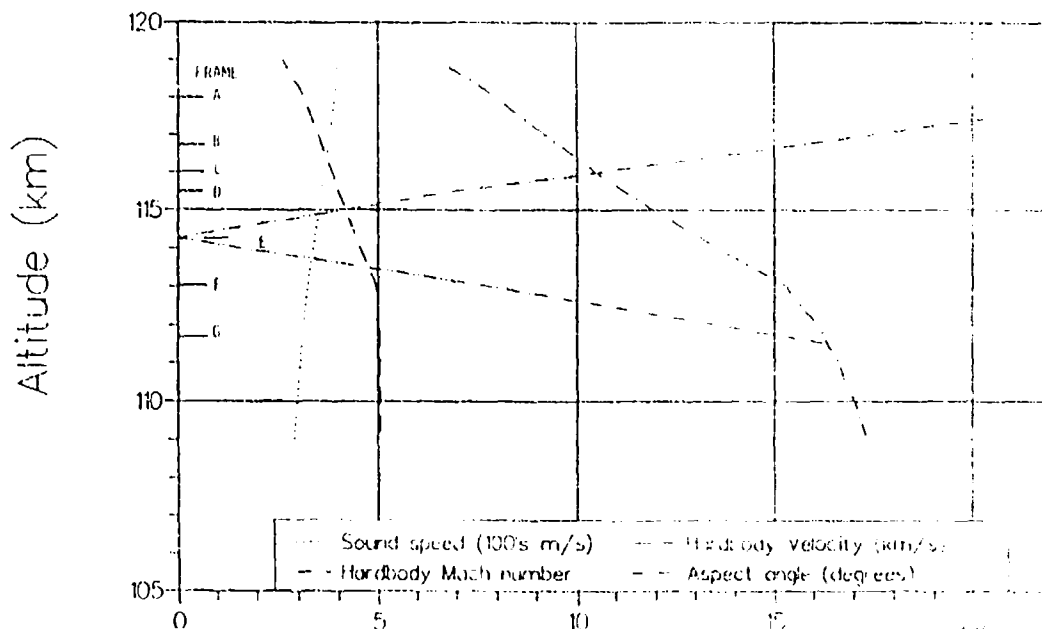


Figure 18. Strypi-XI flight parameters during the Star 27 burn (see also Table 3). The aspect angle refers to the trajectory direction.

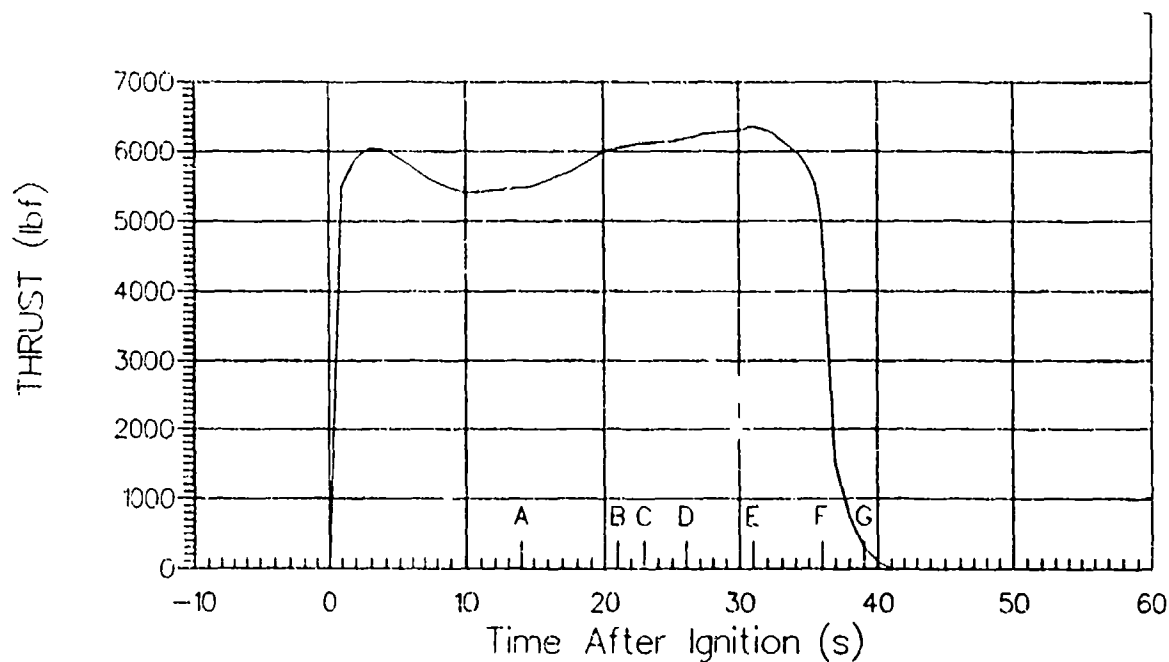


Figure 19. Star 27 engine thrust, as provided by the Bow Shock experiment support group. Ignition was at 239.1 s after liftoff.

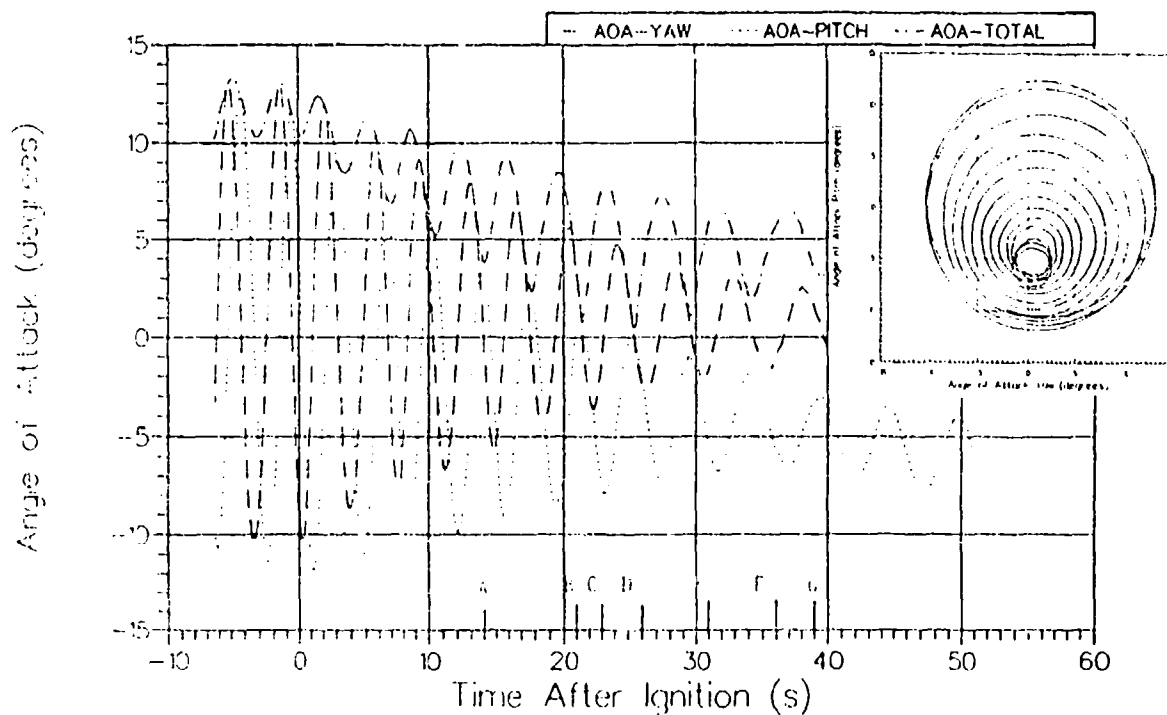


Figure 20. Angles [of attack] between the long axis and trajectory direction of the Strypi-XI. Positive pitch is up, positive yaw is to starboard. Inset of pitch vs. yaw shows the spiral coning of the attack angle.

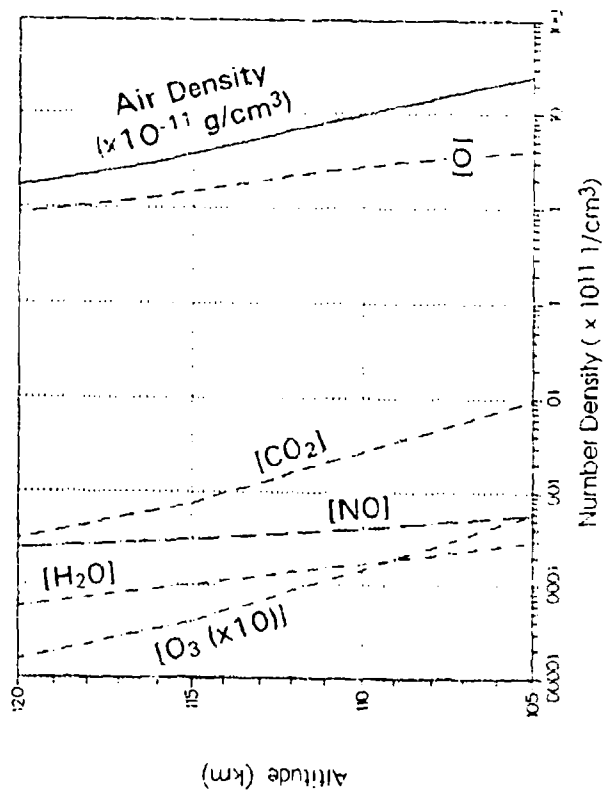


Figure 21. Densities of atmospheric species during the Bow Shock 2 experiment (see also Fig. 3).

Figure 22. Elevation view of the Strypi-XI body after its first two propulsion stages were jettisoned, with the pointing of its optical sensors. Dimensions are in inches.

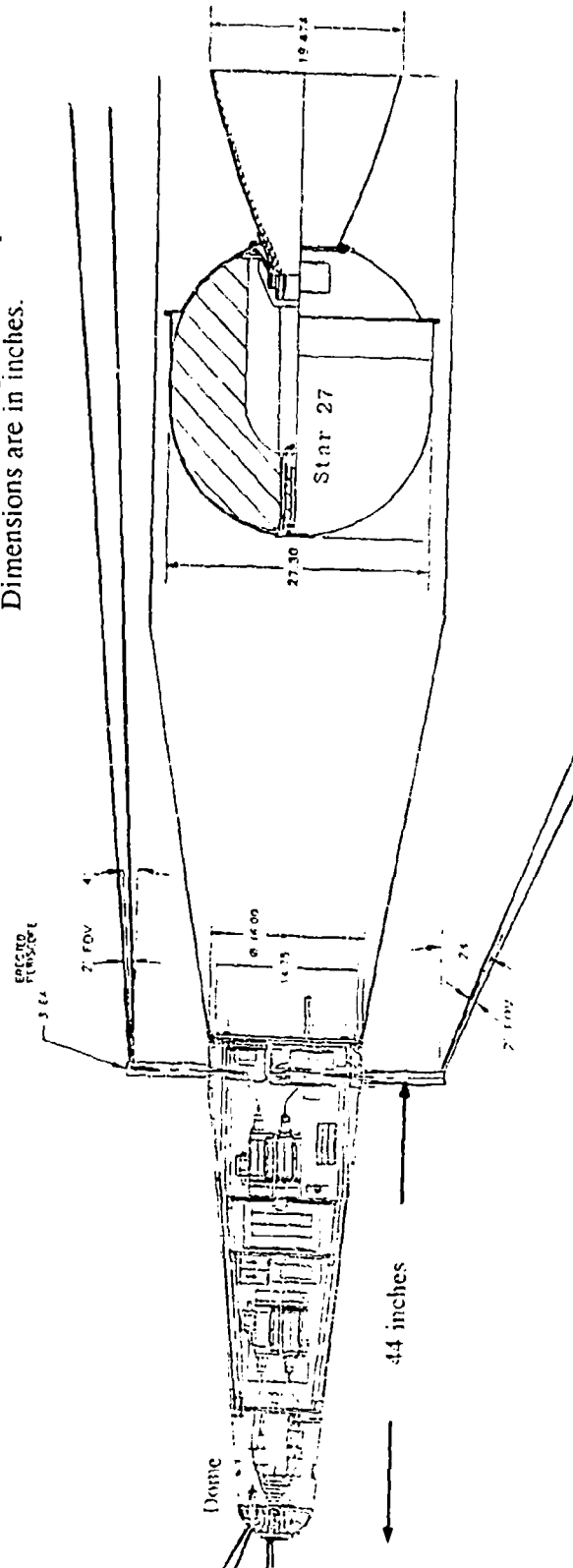


Table 3. Star-27 trajectory parameters\*

| PiSi<br>Camera<br>Image | Time<br>after<br>Liftoff<br>[s] | Altitude<br>[km] | Aspect Angle<br>to AMOS<br>[degrees] | Range<br>to<br>AMOS<br>[km] | Strypi-XI<br>Velocity<br>[km s <sup>-1</sup> ] | Air Density<br>[10 <sup>-11</sup> g cm <sup>-3</sup> ] |
|-------------------------|---------------------------------|------------------|--------------------------------------|-----------------------------|--|--|
| **                      | 181.0                           | 108.4            | 37.0                                 |                             | 2.05   | 13.1   |
| Ignition                | 235.0                           | 119.2            | 34.7                                 | 315.0                       |  |  |
|                         | 239.0                           | 119.0            |                                      |                             |  | (Apogee)   |
|                         | 240.0                           | 119.0            | 31.7                                 | 306.4                       | 2.63   | 1.91   |
|                         | 245.0                           | 118.7            | 28.4                                 | 299.0                       |  |  |
|                         | 250.0                           | 118.1            | 24.2                                 | 292.9                       |  |  |
|                         |                                 | 118.0            |                                      |                             | 3.14   | 2.19   |
| A                       | 253.0                           | 117.6            | 21.9                                 |                             | 3.28   | 2.33   |
|                         | 255.0                           | 117.4            | 20.3                                 | 287.7                       |  |  |
|                         |                                 | 117.0            |                                      |                             | 3.50   | 2.54   |
| B                       | 260.0                           | 116.5            | 14.2                                 | 281.4                       | 3.65   | 2.75   |
| C                       | 262.0                           | 116.1            | 11.2                                 |                             | 3.81   | 2.98   |
|                         |                                 | 116.0            |                                      |                             | 3.85   | 3.01   |
| D                       | 265.0                           | 115.5            | 6.7                                  | 276.5                       | 4.01   | 3.31   |
|                         |                                 | 115.0            |                                      |                             | 4.20   | 3.62   |
| E <sup>††</sup>         | 270.0                           | 114.3            | .0                                   | 274.8                       | 4.47   | 4.17   |
|                         |                                 | 114.0            |                                      |                             | 4.58   | 4.40   |
|                         |                                 | 113.0            |                                      |                             | 4.96   | 5.38   |
| F                       | 275.0                           | 112.9            | -8.3 <sup>†</sup>                    | 276.7                       | 4.97   | 5.50   |
| G<br>(Burnout)          | 279.0                           | 112.1            | -12.9                                |                             | 5.04   | 6.44   |
|                         | 280.0                           | 111.5            | -16.3                                | 283.0                       |  |  |
|                         |                                 | 111.0            |                                      |                             | 5.05   | 8.01   |
|                         |                                 | 110.0            |                                      |                             | 5.06   | 9.75   |
|                         | 285.0                           | 109.9            | -23.8                                | 292.1                       |  |  |
|                         | 290.0                           | 108.2            | -31.2                                | 305.6                       |  |  |

\*Refer also to Fig. 18 and Table 2.

\*\*Antares photograph in Fig. 15.

†Minus signifies retrograde direction from normal at 0 degrees.

††Refer to Fig's. 24 and 25.

When the outer infrared glow first became above threshold of the AMOS imager the forward velocity of the suborbital vehicle thus exceeded this initial retrograde gas velocity, by 0.35 km/s--very close to the speed of sound in the ambient atmosphere. The combustion gas has mean molecular weight 20.2 and additional internal and kinetic energy corresponding to its 1507K kinetic temperature and 1.292 ratio of specific heats (these thermodynamic properties are also calculated, and have not been directly measured; see Ref 12). This latter energy in fact exceeds the directed translational energy of the exhaust molecules relative to the static atmosphere over the period when infrared emission was measured. As Table 2 shows, the Antares engine has  $\sim 4\times$  greater thrust than the Star 27, and 650K higher temperature gaseous exhaust with typically factor-2 different relative abundances of the same principal chemical species (except HCl, which is an order of magnitude lower). Despite the comparable directed energy of this gas relative to the atmosphere at the up to 2.6 km/s velocities of this second stage Strypi-XI operation, the Antares produced no outer infrared glow above the sensitivity threshold of the AMOS imager.

**Onboard and Spaceborne Optical Sensors.** Inside the nose of the Strypi-XI was an array of ultraviolet-sensitive spectrometers and filter radiometers--the "UV Science Package"--viewing both the exhaust flowfield-related emissions by means of optical fields extended outward on erectable periscopes and ram-hemisphere air shocked by the hypervelocity hard body (and perhaps exhaust gases). A diagram showing the pointing directions of these instruments and the dimensions of the nose (310 cm from the exit plane of the Star 27 engine) and aeroshell skirt appears in Fig. 22. Preliminary results from these onboard sensors include observation of the expected A  $\rightarrow$  X bands of NO from the windward air volume when the Bo.v Shock vehicle was at altitudes below 93 km (Ref's 9,10), and unexpectedly high ( $\sim 10^{-9}$  W/cm<sup>2</sup> sr) radiances from the Antares and Star 27 wake volumes in the field of an outboard  $250 \pm 25$  nm-sensitive photometer pointed  $25^\circ$  from its long axis (Ref's 12,13). The latter has been provisionally interpreted as Cameron-band emission from essentially-metastable CO(a <sup>3</sup>II<sub>r</sub>) molecules (0.008 s lifetime, thus with 23 m exponential radiative path if as expected they originate from the combustion volume). The SWIR radiances, as we will see, are many orders of magnitude greater than these UV radiances and the visible radiances reported in Section 1.

The ultraviolet emissions from the region within a few Strypi-XI lengths were also "imaged" at low spatial resolution by the LACE satellite-borne multispectral camera (Ref 16), detailed results from which are pending. As the data so far released appear to be dominated by intense thermal emission from the particulate exhaust, we do not discuss them further here.

**Infrared Camera.** The IR imager (Ref's 34,35) is based on the AF Rome Air Development Center-developed platinum silicide Schottky-barrier photovoltaic detector (Ref 36), a monolithic CCD array (now RCA/TA11367) with 64 vertically  $\times$  128 elements each  $80\text{ }\mu\text{m} \times 40\text{ }\mu\text{m}$  with  $50\text{ }\mu\text{m} \times 25\text{ }\mu\text{m}$  active area. A flat tertiary mirror reflected the light beam from the secondary mirror of the 1.6 m AMOS "MOTIF" telescope into the camera, which was mounted on the side Blanchard surface of the telescope; a refractive lens then relayed a 3 arc minute square field of view onto this image plane. Nominal aperture ratio of the imager's optical system is f/6. Drift in apparent trajectory direction that results from the changing right ascension required to maintain track by the astronomical mount is small in the video replay compared with the regular oscillation due to the coning motion of the Strypi-XI body (Fig. 20), with whose long axis the bright particulate exhaust aligns. The decreasing-then-increasing range from AMOS (Table 3) produces a maximum variation of 6% in image scale among the Star 27 frames reproduced in Fig. 15, which we corrected out when reducing the image data. The corresponding component of scale along the trajectory vector, which would be the symmetry axis of optical radiation patterns were the thrust, velocity, and long axis of the body coaligned, varies over an 11% range.

The PtSi photodiode array was cryocooled to 65K and operated at a readout rate of 30 exposures/s, with automatic baseline subtraction and compensation for response nonuniformities across its imaged field. Its output currents are recorded with 12 bit precision, 8 bits of which is converted to a standard analog video signal/display. We assume here that these photocurrents remain directly proportional to irradiances at the pixels at the far below saturation irradiances produced by the outer glow. Figure 23a (from Ref 4) shows the intrinsic spectral response of this photodetector corrected for attenuation by a short wavelength cutoff cold filter in the optical system of the camera, and the transmission along the  $19^\circ$ -elevation atmospheric path between mountaintop observatory and infrared glow. (The telescope mirrors and final lens are spectrally flat over the wavelength range shown.) We calculated this transmission using LOWTRAN 5 (Ref 37) for a clear low-latitude standard atmosphere with 23 km sea-level visibility, a good approximation to the conditions that obtained during the Bow Shock 2 experiment period. Figure 23b, the product of these two factors, represents the spectral sensitivity of the AMOS infrared imager as moderated by the intervening air mass; it responds principally to photons with wavelengths between the  $\text{CO}_2$   $\nu_3$  fundamental at  $4.3\text{ }\mu\text{m}$  and the  $\text{H}_2\text{O}$  stretch modes- $\text{CO}_2$  intercombination bands near  $2.7\text{ }\mu\text{m}$ , with "wings" to the red and blue.

To assess the absolute radiometric response of the camera to the extended infrared source, we (1) applied its sensitivity to point sources stated in the AMOS users' handbook

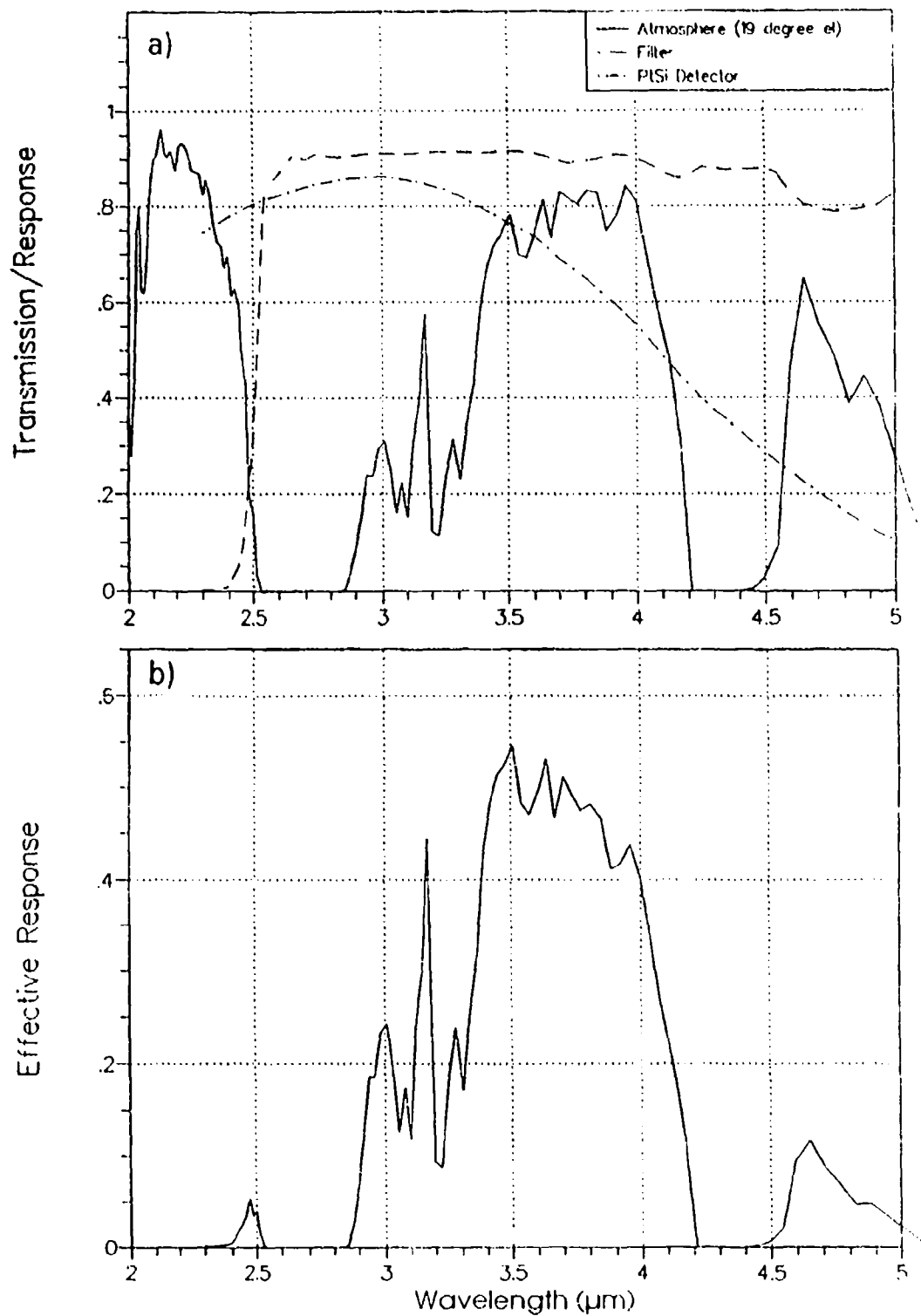


Figure 23. a) Intrinsic spectral response of the PtSi photodetector and transmission of the 19°-elevation clear atmosphere above AMOS. b) Product of these two factors (camera system sensitivity).



(Ref 11); (2) adopted data from its previous (1985) imaging of a control rocket exhaust-interaction volume; (3) referenced to the estimated in-band radiance of the particulate exhaust cloud at the downstream distance where its image photocurrents become equal to those from the outer infrared glow; and (4) derived the measured mean scene brightness *ab initio* from the noise equivalent irradiance of platinum silicide photovoltaics. The  $3\times$  noise equivalent radiance (1) calculated from the nominal threshold of the camera for detecting stars, which have "images" typically spread over  $2 \times 2$  pixels or  $2.4 \times 10^{-11}$  steradians in object space (Ref 11), was found to be  $3 \times 10^{-5}$  W/cm<sup>2</sup> sr. In the earlier application of this PtSi camera configuration (Ref 4) (2) we determined that the  $\sim 10^{-4}$  W/cm<sup>2</sup> sr SWIR radiance of Shuttle Orbiter's sunlit body produced mid-range output currents, a figure satisfactorily close to the handbook value (1) for extended sources.

For the estimate of thermal radiance of the exhaust particles (3) we applied the (rather gross) approximations that they have a uniform radius of  $3 \mu\text{m}$  (Ref 38); are initially solid at the 2300K  $\text{Al}_2\text{O}_3$  phase-transition temperature, where their emissivity averages 0.04 over the AMOS camera's spectral band (Ref 39; it then decreases rapidly as they cool); lose internal energy primarily by thermal radiation (heat transfer to/from the accompanying gaseous exhaust appears small (Ref 12)); and are uniformly distributed in the cone indicated by the high-resolution video image shown in Fig. 15. (This pattern indeed corresponds to the  $34^\circ$  effective engine nozzle opening illustrated in Fig. 22: the angle appears smaller in equi-brightness contour presentations, which do not directly define the "edge" of diverging streams.) The particle cloud furthermore is optically thin, as is the gas. The rate of loss of heat energy by the individual particles then leads to a brightness of about  $10^{-3}$  W/cm<sup>2</sup> sr in the SWIR response band. Since this calculated result is sensitive to the poorly-known size distribution, initial solid/liquid ratio (or enthalpy), and temperature-dependent spectral emissivity of (partially-contaminated)  $\text{Al}_2\text{O}_3$  condensate, it is much less reliable than the other three derived here.

For the last-mentioned estimate (4) we applied the PtSi detectivity of  $1 \times 10^{10}$  W/cm(Hz)<sup>1/2</sup> at  $3 \mu\text{m}$  and 65K (Ref 40), which leads to unit signal/noise from  $50 \times 25 \mu\text{m}$  pixels in one 1/30-s integration period for  $2 \times 10^{-7}$  W/cm<sup>2</sup> irradiance. The transmitted scene radiance that results in the observed mean signal/noise ratio of about 3 in the f/6 aperture ratio AMOS camera would then be  $3 \times (2 \times 10^{-7}) \times (4/\pi) \times (6)^2 \approx 3 \times 10^{-5}$  W/cm<sup>2</sup> sr; this is in fact the same number as we derived by method (1). In view of the usual other optical system losses and attenuation by the atmosphere we adopt twice this minimum figure as the best-estimate of the "average" exoatmospheric radiance of the outer infrared glow in its projection to AMOS.

Since the mean radius and radial "thickness" of this isotropically-emitting volume are about 40 m and 15 m (as Fig's. 24 and 27 show) its tangential column length would be ~30 m. Thus the mean volume emission rate producing this surface brightness becomes  $2 \times (3 \times 10^{-5} \text{ W/cm}^2 \text{ sr}) \times (4\pi \text{ sr})/(3000 \text{ cm}) \approx 2 \times 10^{-7} \text{ Watts/cm}^3$ ; and since the energy of the infrared quanta to which the filtered-PtSi detector responds averages 1/3 eV, this rate can alternatively be expressed as  $(1/3)^{-1} \times (6 \times 10^{18}) \times (2 \times 10^{-7}) \approx 10^{12.5} \text{ photons cm}^{-3} \text{ s}^{-1}$ . This rather large figure, which has a  $1\sigma$  uncertainty range that we estimate as  $\pm$  a factor 3. It refers to midrange output currents produced by photons with wavelength near 3  $\mu\text{m}$ ; SWIR features strongly attenuated by the atmosphere would have still higher volume emission rates.

**Visible Light-Sensitive Cameras.** As mentioned above the video camera that produced the higher spatial resolution image in Fig. 15 (Ref 11) was coaligned with the infrared sensor, while the shorter focal length camera was on a differently-tracked 1.2 m AMOS telescope ("MATS"). Nominal FWHM photon response of the two S-20R Intensified Silicon Intensifier Target imaging photocathodes, corrected for attenuation by the 19° elevation-angle atmosphere (which increases toward the blue), is 3850 to 6700Å; refer to Fig. 14. Enlargements of Star 27 scenes from the much wider field of view (3°-diagonal), more sensitive (f/5) camera to the same scale as the two narrow-field imagers convey little information beyond that indicated in Fig. 16.

The example frame in the top row of Fig. 15 from the 1.5-arc min horizontal field f/20 camera has been demagnified to match the angular scale of its corresponding PtSi image. (Its electronic gain was low, apparently to avoid excessive overexposure of the higher-thrust second propulsion stage that had operated ~1 min earlier.) These high-resolution photographs lend themselves to validating predicting of the dynamics and cooling of the condensed particles by the methods we have applied for quantifying AMOS images of control rocket exhaust (Ref 6) and water ventings (Ref 7) from space shuttle (this task is to be done separately). We use them here primarily to verify that the exhaust gas and condensed-droplet cloud are to a satisfactory approximation decoupled beyond a few m from the engine exit plane, as is qualitatively evident from the congruence of the beam at all Antares and Star 27 altitudes and the absence of detectable lateral scattering of the particles.

### **Theoretical Background**

The overexposed area of the SWIR images (instrumentally bloomed, and "reversed" near the rocket vehicle) is as mentioned also due to thermal emission from this microns-scale  $\text{Al}_2\text{O}_3$  condensate (Ref's 12,13), as is further evidenced by its close geometric similarity to the pattern of visible radiation recorded by the coaligned video system. (Limb enhancement is

present in both wavelength bands, which is attributable to a nonuniform initial angular distribution of the droplets and perhaps enhanced collisional cooling by the more dense paraxial exhaust gas.) As alluded to just above, this long-focus camera is not sufficiently sensitive to image the lower-brightness, much more widespread visible chemiluminescence described in Section 1, which shows in Fig's. 1 and 15 as extending forward to the Strypi-XI body.

In support of the Bow Shock experiments program, nonequilibrium reactive-flow calculations of the ultraviolet radiation intensities from air excited by a hypervelocity elliptically-blunted cone with skirt-type afterbody were made (Ref's 41, 42 and ref's therein). These were followed by a computational fluid-dynamical model of the densities and temperatures of the gaseous and condensed components of the exhaust (and ambient air), from which results for the Antares at 109.6 km and moving at 1.97 km/s [only] have been presented (Ref 12). The initial UV Diagnostic Experiment planning focused on excitation of nitric oxide gamma bands ( $A^3\Sigma^+ \rightarrow X$ ) near 2200Å in the high-temperature air volume near the stagnation streamline. Photometers sensitive to some of the ultraviolet electronic bands from other species prominent in laboratory air shocks (such as OH,  $N_2^+$ , CO, and CN) were also fielded as part of the Ultraviolet Science Package.

The clear association of the outer SWIR glow with the Star 27 engine burn shows that it results from the flow of combustion products, rather than passage of the Strypi-XI body. The calculated densities and temperatures of this exhaust gas and the air that it sweeps out and heats can in principle be post-processed to estimate the rates of vibrational emission from pre-existing and newly created molecules (see Fig. 20 and Table 4). As of now, however, neither the planning for or the initial UV spectroradiometry results from Bow Shock directly associate this outer glow observed from AMOS with known infrared transitions. As mentioned above, we make use of the information presented in Ref 12 on the lower Strypi-XI-velocity Antares burn (predictions for the Star 27 are reported as performed but are not yet released).

These engine exhaust gases initially push out and compress the local atmosphere somewhat like a large (compared with the vehicle diameter) elastic body (Ref's 18,21,22,26). The numerical flowfield calculations for Antares predict maximum kinetic temperatures of order 2800K in the "contact surface" where this expanding, but not yet posigrade-directed, gas is reheated as it piles up and incorporates ambient air. As we will show after assigning numerical values to the AMOS images, the radial thickness and outward velocity of the observed infrared-emitting volume are at least semiquantitatively consistent with the expected behavior of this interface. Furthermore, as is suggested by the comparison in Fig. 16 of spatial distributions of the SWIR and the visible wake emissions, these data lead to the conclusion that one or more of the above-mentioned combustion gases is being excited, rather

than that the glow is a result of the thermodynamic properties of strongly-shocked air at the 113 - 117 km altitudes of Bow Shock 2.

### Image Data

**Qualitative Overview.** The infrared photographs labeled A - G in Fig. 15 are single 1/30 s PtSi camera frames from which an 8-frame average scene-plus-detector noise baseline, recorded just before the Star 27 engine ignited, has been subtracted. Further efforts to coadd and otherwise process these images resulted in small improvements in signal/noise, the principal limitation being the misregistration noted just below. Test computer projections of hollow cones showed that the effect of the narrow range of aspect angles to the trajectory on the measured spatial distributions is so small compared with errors in reading the relative radiances from the video records that it can be neglected. Local horizontal in Fig. 15 is approximately 3° clockwise of the centerline of the off-scale  $\text{Al}_2\text{O}_3$  particle emission, and (as Fig. 20 shows) the trajectory vector is generally a few degrees from the exhaust symmetry axis in planes near-parallel and perpendicular to the view direction from AMOS.

The higher thrust Antares solid-propellant engine operated in the 35.4 s ending 48.6 s before the Star 27 ignited, accelerating the Strypi-XI from 0.3 km/s to 2.6 km/s at upleg altitudes between 105.2 and 110.9 km (about one density scale height below the third-stage operation range); refer to Fig. 17 and Tables 1 and 3. It has not inconsiderably different calculated relative abundances of its gaseous species: in HCl (1/10 Star 27),  $\text{H}_2\text{O}$  and  $\text{CO}_2$  (1/3 Star 27), and CO and  $\text{N}_2$  (2 Star 27). The Antares stage remained within the field of the infrared camera until 3 s before it burned out, always producing overexposed SWIR images of the hot  $\text{Al}_2\text{O}_3$  particles such as the example in Fig. 15 as well as the 10's km-long, several s-persisting visible wake analyzed in Section 1. The particulate exhaust extends over a smaller solid angle and appears to have a steeper gradient toward the retrograde end of its saturated image area than that from the Star 27, because the Strypi-XI was then at longer range and shallower aspect from AMOS. These infrared photographs of Antares show no evidence of an outer glow.

Modulation of the angle of attack of the third Star 27 stage (caused by a low-velocity collision with the still-smoldering jettisoned second stage; see Fig. 20) appears as a regular angular oscillation of the overexposed image area in replays of both the infrared and visible-light video frames. Tracking error introduces a further frame-to-frame jitter of typically 1/20 SWIR scene height and width (~5 microradians). These rotations and translations of the images are sufficiently small to allow some smoothing of one-dimensional photocurrent traces by coadding short sequences of frames. In practice, the higher dynamic range CCD output

data from the original digital PtSi camera record (Ref 43) did not provide significantly better signal/noise than the as-corrected and -reproduced analog video presentation.

The outer glow becomes just visually detectable over the normal fluctuations in scene and dark-current baseline in the original of Frame A. Its mean brightness afterward increases, and then shows a decrease in Frame F where the engine thrust--which, as in Section 1, we take as the nominal rate of exhaust energy output--has fallen to about  $\frac{1}{4}$  of its previous average (see Fig. 19). Despite the increasing free-stream velocity and air density the glow volume then goes below radiance threshold just before Frame G, in which the thrust has decreased by about another factor of 15. (This propellant burnout period is also to be treated separately.) The mean lateral displacements of the radiance maximum decrease slowly over the data period, with a dependence on Strypi-XI velocity and ambient density that we present below. In Frame G, near total burnout, the length of  $\text{Al}_2\text{O}_3$ -condensate cloud that is off-scale in the infrared images has fallen to 35 m from its previous average of 85 m; then as expected this thermally-emitting region appears still smaller when the Strypi-XI moves completely out of the field of view within the next 1 s.

As is interpreted above, the high-resolution video camera detects only the visible gray-body emission from this particulate exhaust. In the photographs from the higher-sensitivity wide angle camera this inner quasiconical region is severely overexposed; the glow that we have associated with the exhaust gases extends backward along the general direction of the trajectory with limb brightening and a lateral width that approaches an asymptote at about 1 km upstream from the thruster as is shown in Fig. 1 and suggested by Fig. 16.

The images in Fig. 15 are in effect snapshots of a moving coordinate system, in which an atmospheric "wind" blows toward the nose of the Strypi-XI at its velocities listed in Table 3. In consequence the time scale of events in the static reference frame of the undisturbed atmosphere becomes shorter as this free-stream velocity increases from 3 to 5 km/s over the data period. The  $\sim 10^{-3}$  g cm<sup>-2</sup> mass/area alumina droplets move largely unimpeded by the accompanying gas (Ref 12 indicates that only their submicron component experiences marginally significant lateral scattering). Since these particles emerge from the engine at (calculated) 2.93 km/s, their velocity along the trajectory relative to the outside atmosphere or AMOS is in the direction of the Strypi-XI velocity in all the Star 27 images included in Fig. 15; and since the radiating cloud exhibits essentially stationary behavior and so can be considered attached to the moving hard body, it provides a time scale applicable to the region of image near the trajectory. In contrast the gaseous combustion products initially expand laterally, at mean outer-surface speeds that generally exceed this retrograde droplet velocity (Ref's 18,24,26,27), with the result that they are slowed by collisions with the atmospheric (and previously-exhausted) molecules. The time scale at other points within this

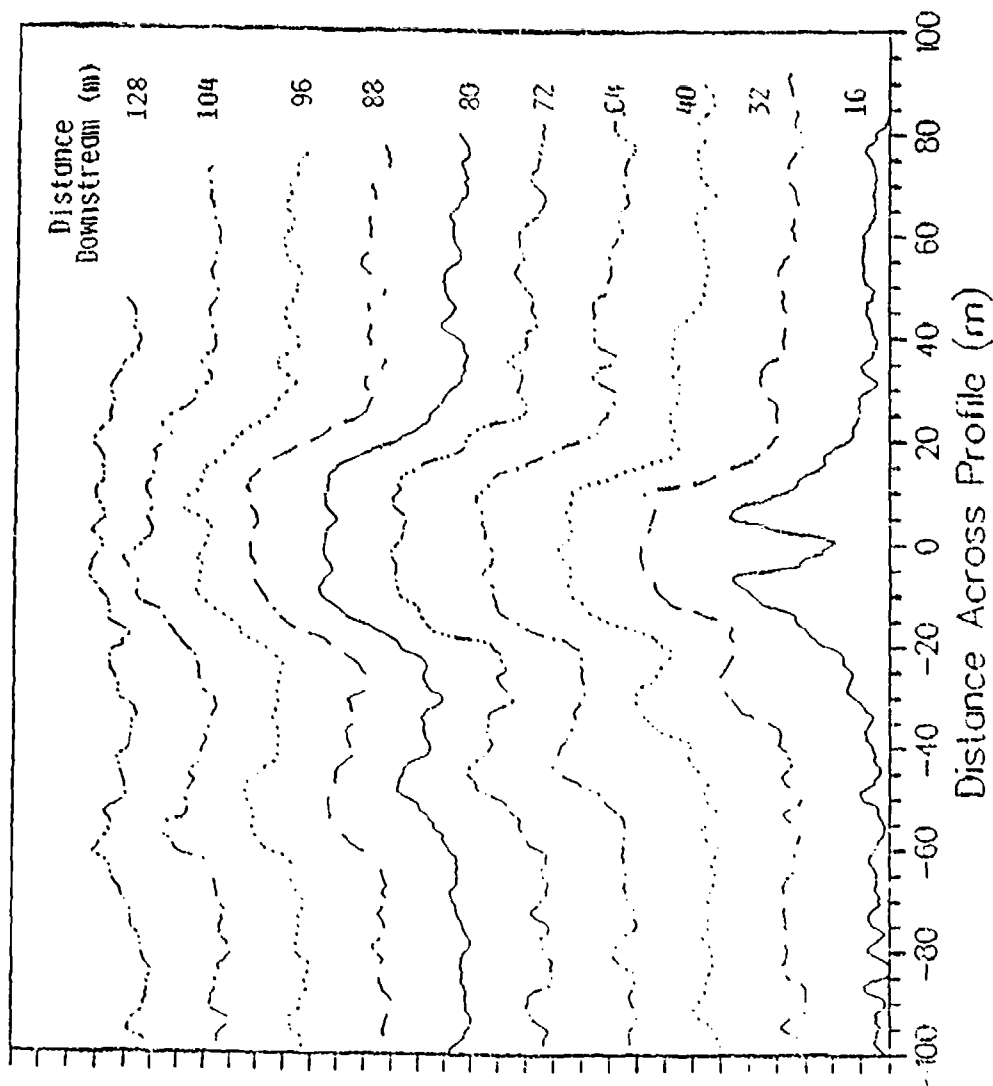


Figure 24. Photocurrents averaged over five adjoining pixels in scans perpendicular to the symmetry axis of the outer glow in Frame F. The retrograde distances refer to the moving coordinate system. The minimum in the image of the alumina-particle cloud at 16 m is an effect of its severe overexposure.

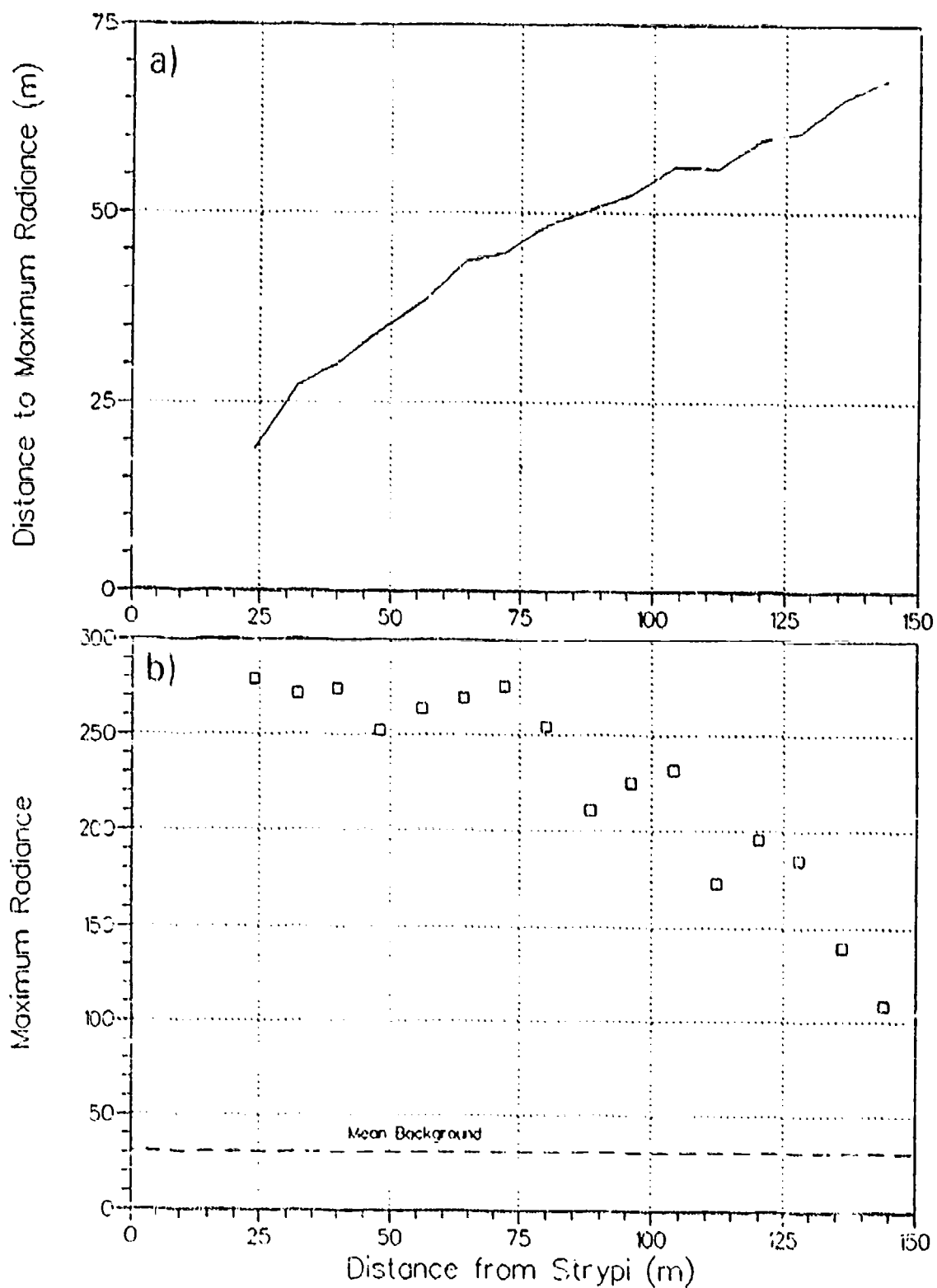


Figure 25. a) Position and b) magnitude of the low-altitude side radiance maxima in Frame E, derived from Fig. 24 as described in the text.

exhaust-gas volume can thus be determined only from a quantitative description of the flowfield. Unfortunately both the velocity of the Strypi-XI and the densities of air and O atoms are increasing at roughly the same fractional rates over the data set, so that the effects of these parameters on the geometry and brightnesses of the glow are not readily isolated by purely heuristic means; hence the theoretical guidance presented below.

Figures 24 - 32 are numerical data extracted from the SWIR images, intended for developing phenomenological descriptors of and semi-empirical scaling rules for the photogrammetry and photometry of the outer glow. (We have limited this scaling effort in view of the pending availability of information from the numerical model.) Since the radiances--the experiment observable--are products of densities of chemical species and their temperature-dependent reaction rate coefficients summed along columns projected to AMOS (after correction for transport of the resulting long-lived excited molecules), interpretation is needed to relate them to the three-dimensional flowfield. We apply principally the maxima of these radiances, not because they have any greater physical significance than other image descriptors such as gradients and positions of "edges" but because they are subject to less measurement error (see in particular Fig. 24); furthermore the maxima represent a readily-communicated element of the optical signature of the hypervelocity missile. We review first the spatial distribution of brightness under a single set of Bow Shock 2 experiment conditions, and then turn to the dependences on Strypi-XI velocity and air density.

**Reduction-Analysis of a Typical PISI Camera Frame.** Figure 24 is a series of five adjoining transverse pixel-averaged scans normal to the symmetry axis in particularly high signal/noise, perpendicular-to-trajectory viewed Frame E, when this velocity was 4.47 km/s and the altitude 114.3 km. Figures 25a and b show the magnitude and position of the photocurrent maximums on the low-altitude side of the trajectory, where the glow appears brighter. The relative radiances, taken as depending linearly on the incremental photocurrents, were determined by subtracting the extrapolated signal from the instrumentally bloomed exhaust-particles cloud. This more or less subjective correction procedure can be seen to give progressively less reliable results approaching the rocket engine. The distances from the symmetry axis of the particles to the radiance maximum in the outer glow were read from these one-dimensional traces by the image-processing computer, without correction for shifts that could be caused by a sloping underlying background; nonetheless in practice these data points align very closely with those that we took manually from hard copy of the smoothed video scene. The outer infrared glow appears to converge to the head of the reversed area of the images of the droplet cloud, which is perceivedly most overexposed and thus would be at or within a few m of the thruster exit plane.



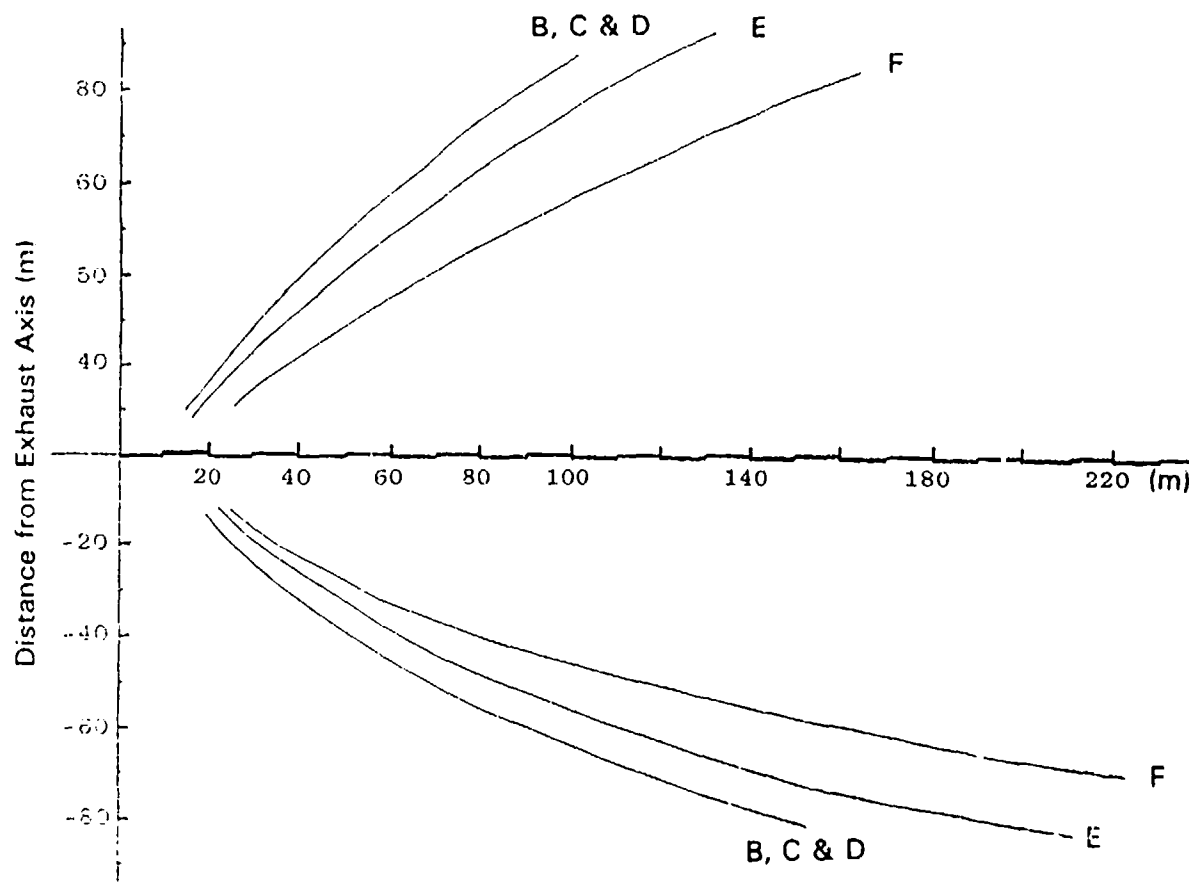


Figure 26. Manual overlay of the radiance maxima in Frames B - F, relative to the centerlines of the particle cloud. The scene magnifications have been standardized, and the view aspect angles are uncorrected.

As the initial slope in Fig. 25a indicates, the maximum of the brightnesses initially moves transverse to the trajectory at a constant velocity comparable with that of the Strypi-XI relative to the atmosphere. This contact surface--as we provisionally interpret the locus of radiance maximum--shows first experimental evidence of departure from linear expansion at a radial distance where the exhaust gas has encountered very roughly 1/10 of its mass. We return to this growth pattern after reviewing the images of the glow at further vehicle velocities.

Within the resolution of these rather noisy cross-track traces, the distance between half-maximums of the radiance enhancement remains constant at about 15 m. In contrast the full width to background increases away from the thruster engine, concurrent with both the leading and trailing edges of the peak becoming less steep. (The contact surface between the explosion and ambient gases is well known to thicken as the interior overpressure decreases; refer to Section 1.) The ratio of the maximum projected radiance of the outer glow to the average

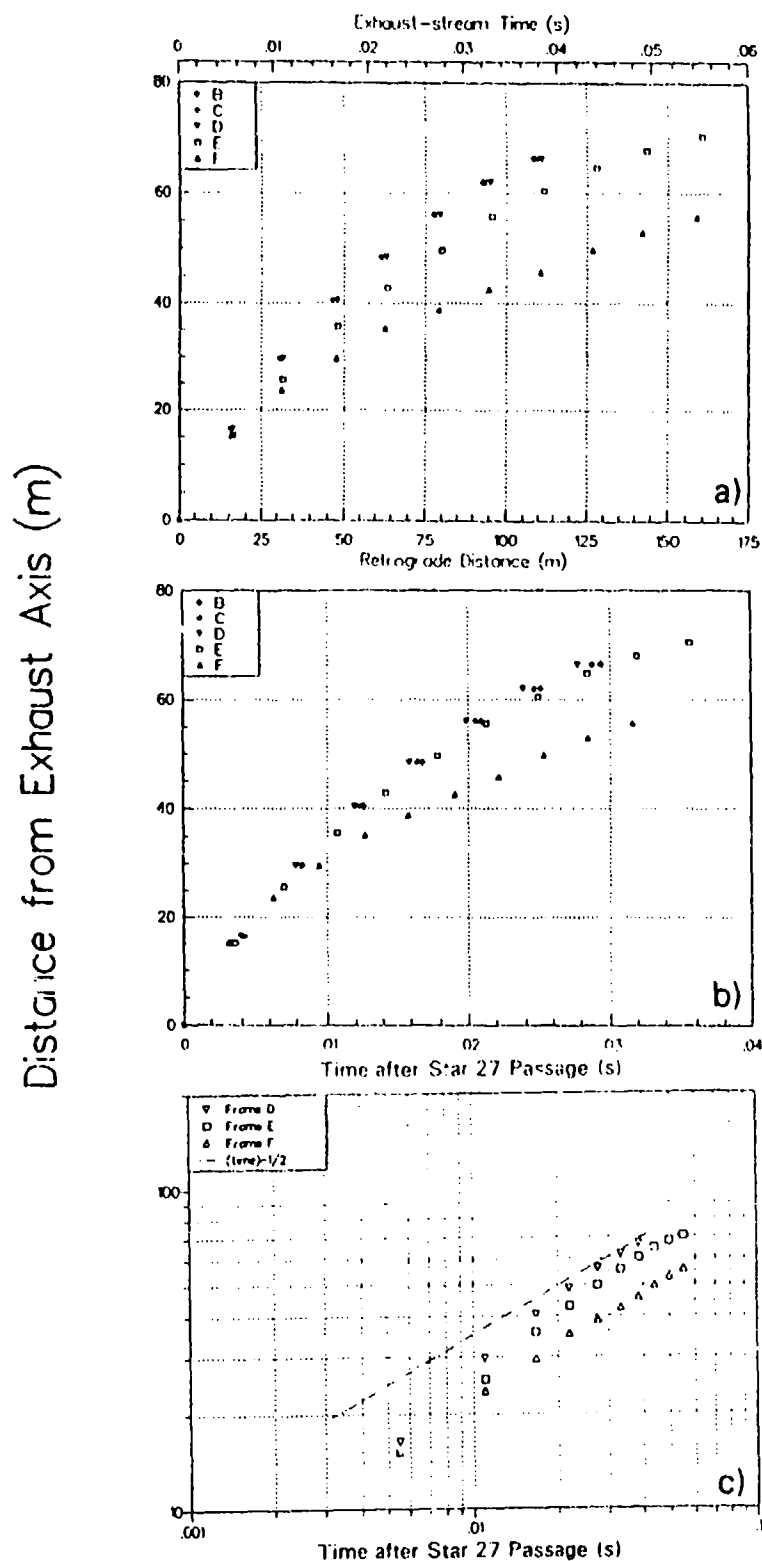


Figure 27. Lateral displacements of the lower-altitude radiance maxima in Frames B - F from the symmetry axis of the particulate exhaust, as a function of a) retrograde distance along the particle cloud and b), c) time since the Strypi passed the trajectory position (free-stream time).

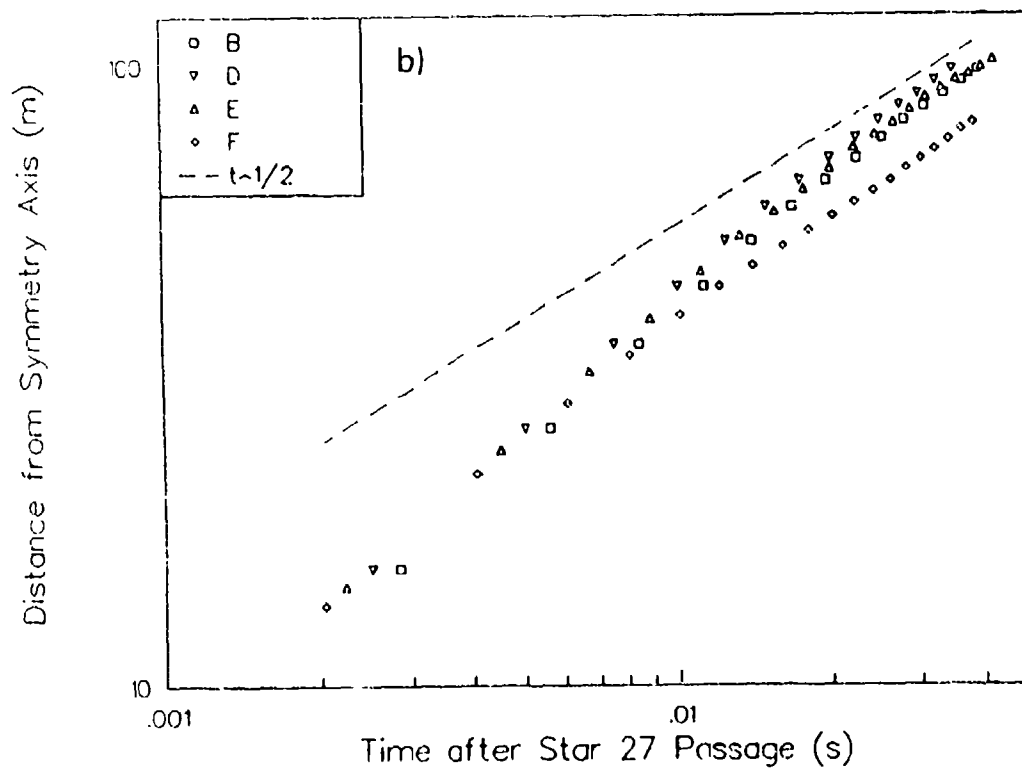
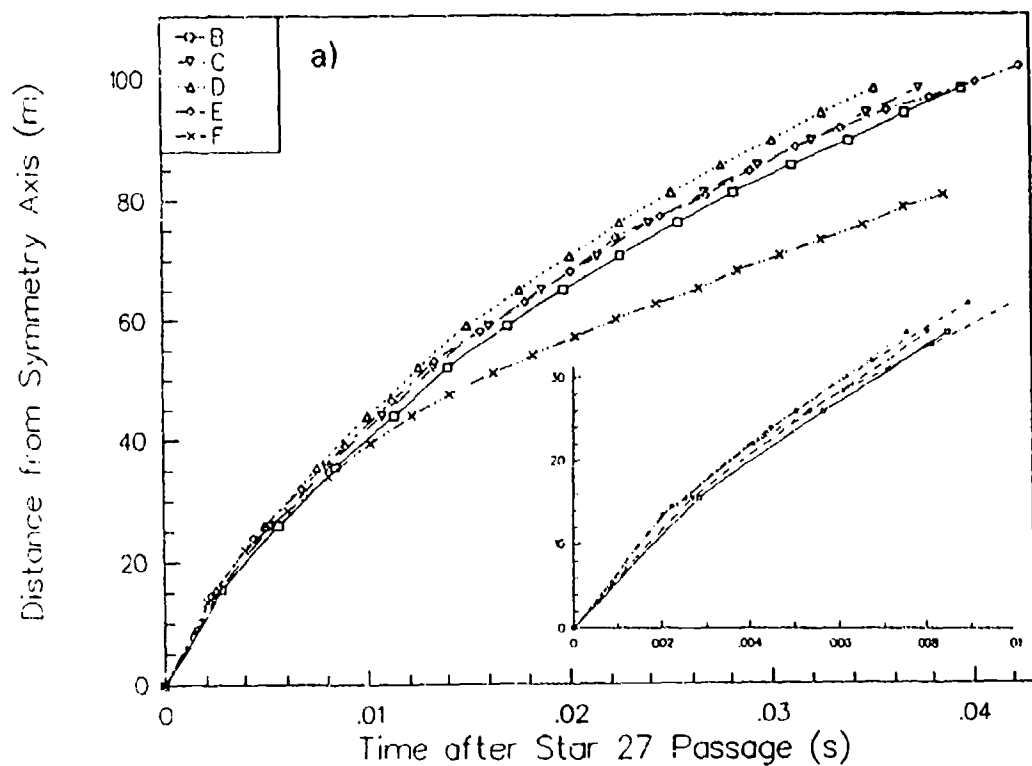


Figure 28. Repeat of the displacement data in Fig. 27, measured from the symmetry axis of the outer infrared glow.

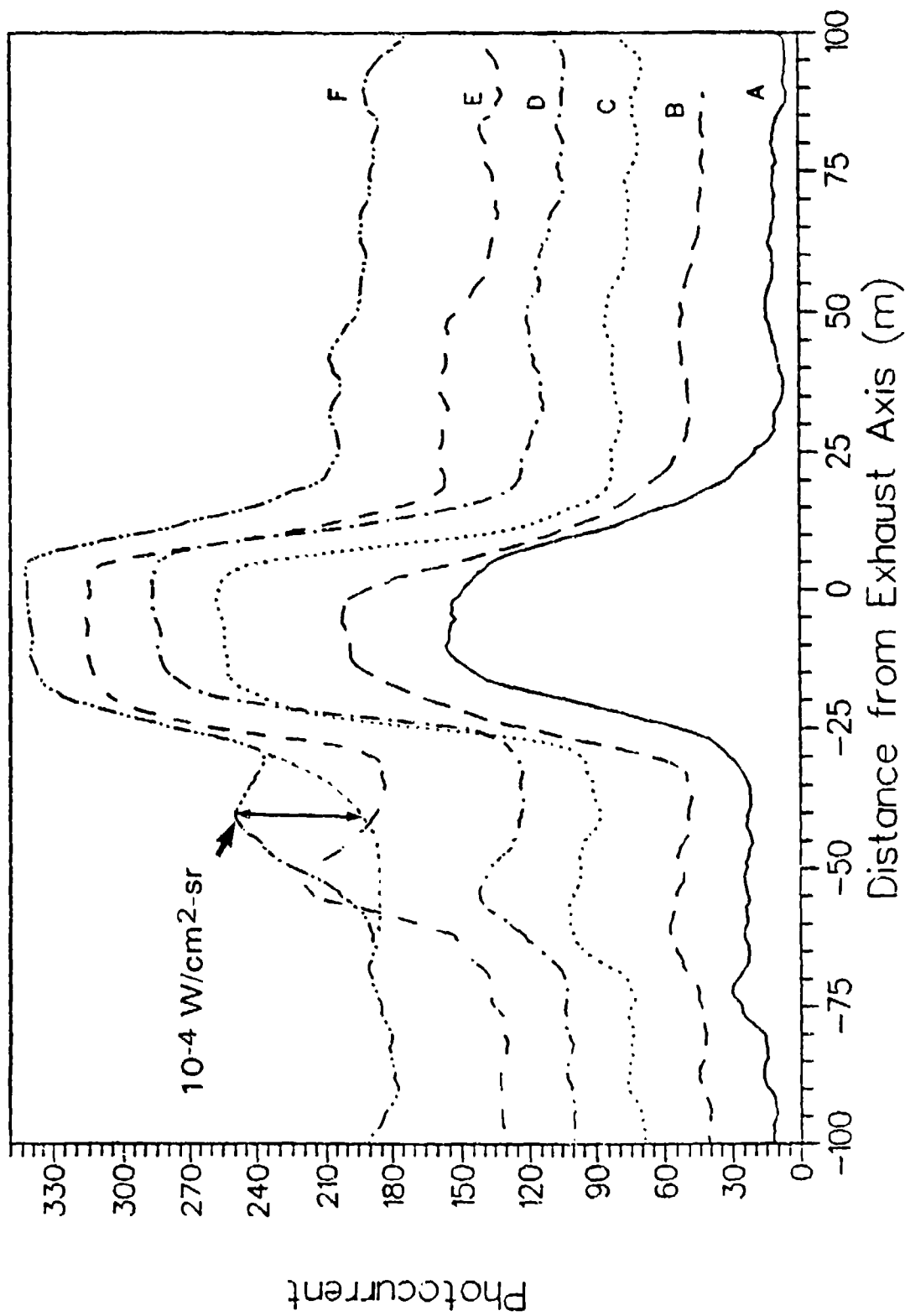


Figure 29. Transverse scans of Frames A - F at 75 m behind the exhaust exit plane (average of 10 adjoining pixels). The absolute peak radiance over baseline ( $3\text{--}5 \mu\text{m}$ ) is accurate to a factor of 3.

radiance viewing inward from the peak (both above dark-noise baseline) remains about 2; with the assumption that the volume emission rate is constant within an annulus this figure turns out to be geometrically consistent with the observed ratio of the displacement of the center of the peak to its full width. The low quality of these data precludes extraction of further reliable geometric descriptors of the SWIR glow.

The maximum low altitude-side radiances transmitted to AMOS (Fig. 25b) decrease by about a factor 3 over the outer glow data length/period, at an accelerating rate, while the space-integrated radiances decrease more slowly. These relatively slow falloffs may indicate that the excitative-reaction rate coefficients do not depend particularly strongly on temperature of the gases, whose calculated maximum initially decreases much more rapidly away from the thruster engine (as indicated in Ref 12); alternatively, in view of the transit times involved they may be an effect of the finite lifetime of the emitting species (see Table 4). The 15-m transverse halfwidth of the brightness peak exceeds the predicted thickness of the contact surface, which is about twice the 2-m ambient mean free path (Ref 18 and ref's therein). (The halfwidth of the numerically-calculated Antares temperature peak shown in Ref 12, which is applicable to a net velocity of the exhaust gas in the retrograde direction, is also near 4 m.) This larger than expected lateral spread is also suggestive of a relatively weak temperature dependence of the reaction(s) producing the infrared radiation; again an alternative explanation is that the broadening is due to diffusion of vibrationally-excited molecules before they emit, as is further mentioned below.

**Frames at Other Strypi Velocities-Air Densities.** The lateral displacements of the outer-glow maxima are intercompared in the manual tracings from frames A - F in Fig. 26, for each of which we oriented four sequential coadded images at a standardized magnification along the centerline of the particulate exhaust. (No correction was made here for the changing view aspect, or for the lower gas-exhaustion rate of Frame F; as Fig. 19 shows, the engine thrusts at the other times considered are all within < 10% of one another.) As is indicated in Fig. 20, this axis is not aligned with the trajectory vector. The rotation to achieve symmetric displacements from the particle-exhaust axis varies among frames between  $1\frac{1}{2}^\circ$  and  $7^\circ$  (as best as can be determined from the low-contrast images), uncorrelated with the small always-positive pitch angle or yaw angle of the Strypi-XI. The mean radial displacement of the peak is always somewhat lower and the maximum brightness is substantially greater on the low-altitude side of the trajectory. This asymmetry may be an effect of the (unknown) azimuthal distribution of the propellant burn of the spinning and coning but always positive pitch angle Star 27 (refer again to Fig. 20).

# Normalized Peak Photocurrent

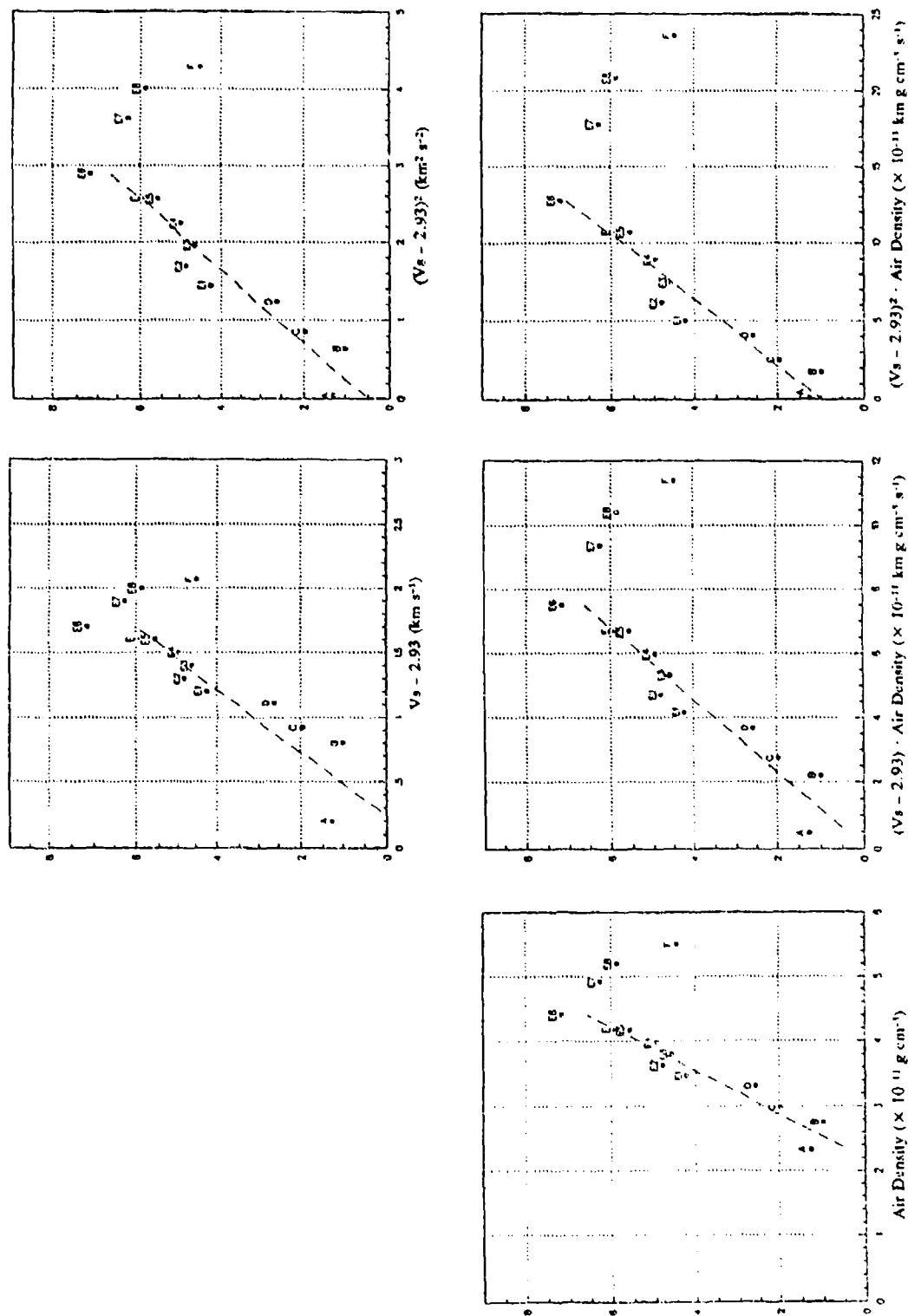


Figure 30. a) Maximum SWIR radiances at 75 m retrograde distance, as taken directly from Fig. 29 (with further E's added) and normalized to the thrust of the Star 27 engine, plotted against experiment parameters.

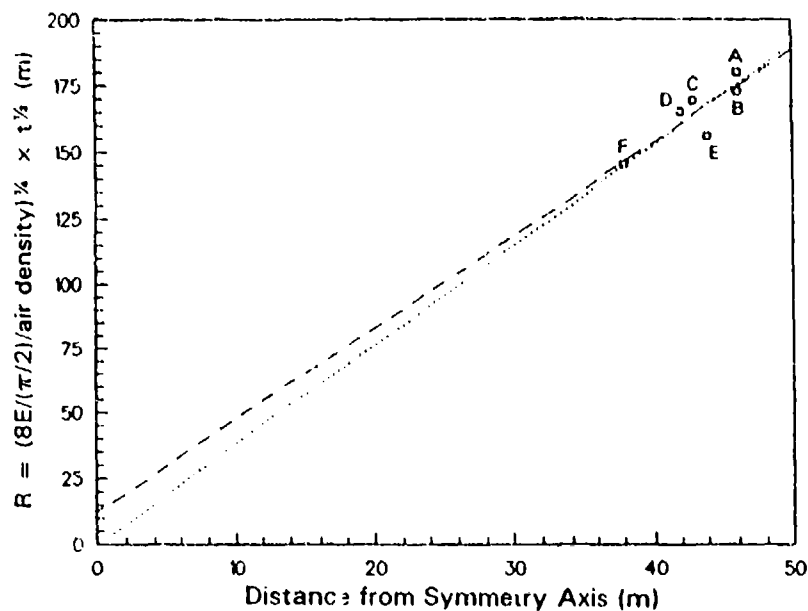


Figure 31. Radius of exhaust interaction front at 0.015 s after passage of Star 27 as compared to the similarity-theoretical expansion radius. The dashed line is a least-squares fit to data and the dotted line is a similar fit forced through the origin. E refers to exhaust energy per unit length along the trajectory, and t to free stream time.

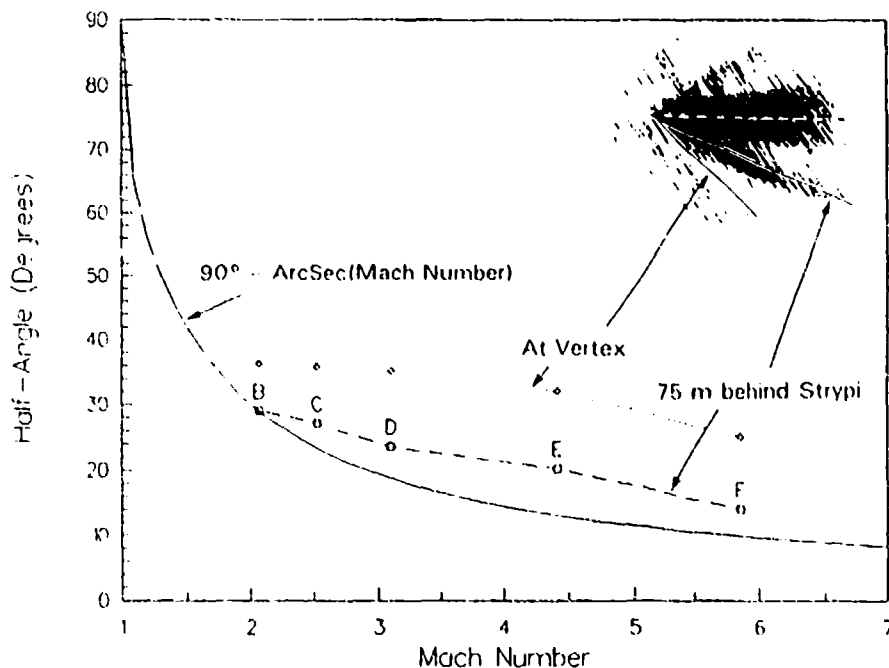


Figure 32. Angles of the maximum radiance line (shock/interface) as a function of the posigrade Mach number of the exhaust gas in the ambient atmosphere. The solid line is the half-angle for expansion of gas from an incompressible body at the ambient sound speed. F has not been corrected for decrease of engine thrust.

The manually measured displacements from the symmetry axis of the particle stream are plotted against distance backward along the particle cloud (Fig. 27a) and against time in the free stream on linear (Fig. 27b) and logarithmic (Fig. 27c) scales. As in Fig. 25, the lateral expansion rates are at first constant because the exhaust gas does work on only a small relative mass of atmosphere. These radial positions of the radiance maximum later increase with (free stream time)<sup>1/2</sup>, the functional dependence predicted from similarity arguments for cylindrical explosions (Ref's 27,28), as discussed in the next subsection. Figure 28 is a plot of the two side-averaged displacements from the symmetry axis of the outer glow (not the particles), from which the same conclusion emerges.

Figure 29 shows a set of radiance traces perpendicular to the symmetry direction at the fixed wake distance of 75 m from the exhaust exit plane (interpreted as the farthest-downstream position in the reversed image area). These data, which were smoothed by averaging ten adjoining pixels from four sequential coadded frames, are the basis for the plots of the magnitude and position of the maximum radiance in Fig's. 30 and 31. The peak photocurrents were again determined by subtracting the estimated baseline due to the hot condensed exhaust (an example is included). Figure 30 includes eight further such brightness maxima (identified as E1 - E8) extending over both sides of the onset of consumption of the solid propellant, to emphasize the effect of combustion rate on optical yield.

Figure 30 plots these radiances at 75 m backward along the trajectory normalized to the engine thrust against the products of powers of [air density  $\rho$ ] and [initial mean posigrade velocity of the exhaust gases (= Strypi velocity  $v_s$  - 2.93 km/s)]. The optical emission rates from shocks around incompressible bodies are well known to increase with  $\rho$ ; and the first power and square of the posigrade velocity of the gas are applied more in the spirit of heuristic fitting than as representations of its momentum and kinetic energy in the reference frame of the atmosphere (as will become clear when we address the glow geometry). This approach implicitly takes into account the observation that the glow volume comes above the AMOS sensor threshold when the mean velocity of the exhaust gas along the trajectory becomes supersonic.

The dashed lines in Fig. 30 are least-squares best fits to the equally-weighted data points from Frames A through E6, and giving zero weight to the three remaining brightnesses measured after the engine thrust began to decrease. (These last points depart even further when they are not normalized to thrust.) The maximum radiances appear to be increasing more rapidly than linearly with thrust, a behavior consistent with the SWIR excitation being due to reactions of the reheated combustion products among themselves rather than with the atmospheric gases intermixed into the contact surface (although other interpretations are possible).



With neglect of the potential effect of this additional uncertainty (actually, an experiment variable), the best fit line of these radiances during full engine burn passes equally close to the origin of coordinates--nominally, zero infrared excitation--when a dependence on  $\rho(v_s - 2.93)$  or  $(v_s - 2.93)^2$  is adopted. This conclusion is unchanged when the two lowest signal/noise points, from Frames A and B, are discarded along with otherwise-questionable E7, E8 and F. In view of the large scatter in the photocurrent data, standard statistical measures that compare goodness of fit of the (assumed-linear) dependences are not appropriate; as anticipated earlier in this report, the concurrent about-equal fractional rates increase of  $v_s$  and  $\rho$  during the AMOS measurements precludes discrimination between these two qualitatively-best fits. We stress again that the maximum radiances 75 m upstream, which refer to a position (or direction) within the sensor's field of view rather than to a fixed time after combustion gas is exhausted, do not represent a fundamental physical quantity that leads to improved understanding of the exhaust-flow phenomenology. The variation of these radiances with experiment conditions in Fig. 30 should be interpreted as merely elements of an optical signature with potential application to scaling the outer infrared glow to other conditions of solid-composite engine operation.

The outward displacement of the two side-averaged radiance maximum at a fixed retrograde distance along the stream of condensed particles is a similarly useful element of this signature. In Fig. 31 we have plotted these radial displacements at 75 m against  $[(\text{energy output in exhaust gas per unit Strypi-XI path})/\rho]^{1/4} \times [\text{scaled free-stream time } (=0.015 \text{ s})]^{1/2}$ . This dependence is predicted by the aforementioned similarity calculations of the transport of cylindrical overdense gas clouds in rarefied air (Ref's 26,27), as further discussed below; the energy output is the sum of the directed posigrade kinetic energy of the gas and its thermal energy. The extrapolated displacement intercepts the origin within the error of the data points. Figure 32 is a plot of the apparent Mach angles of the radiance peak in the two definitions shown. We interpret the smaller than expected Mach angles as due to the supersonic transverse expansion of the exhaust gas combined with its compressibility. The bow shock wave from the Strypi hardbody would behave according to the solid curve in Fig. 32, but this Mach angle is larger than the angle of the exhaust gas contact surface (so the hardbody shock is within the plume boundary and was not observed). [The sound speed within plume is 2-3 times longer than ambient sound speed. This may bring the hardbody shock "out" to coincide with the plume shock.] The compressible nature of the exhaust gas front leads to deformation (flattening out) near the vertex where the pile up of atmosphere is greatest.

### Interpretation

**Background.** Before further considering this spatial distribution of the outer glow, we investigate the reaction processes that could be responsible for emission of  $10^{12\frac{1}{2} \pm \frac{1}{2}}$  per  $\text{cm}^3\text{-s}$  photons with wavelengths at which the PtSi camera responds and the atmosphere above AMOS transmits (Fig. 23b). This volume emission rate is some four orders of magnitude greater than that found in Section 1 to be taking place in the persisting visible wake trail (although the ratio of total optical yields is of course very much less). We ascribed this latter glow to the quasicontinuum from  $\text{AlO}_2^*$  excited by chemiluminous reactions between  $\text{AlO}$ -containing small molecules present at trace concentrations and  $\text{O}$  atoms swept into the contact surface and later mutually diffusing with the pressure-equilibrated, relatively cool exhaust gas. The SWIR excitation is in contrast taking place over a much shorter period, at more limited distances from the Strypi-XI. As we show shortly, it appears to be a result of the high energy densities of an essentially classical Rankine-Hugoniot "bow" shock produced by the engine exhaust, with its elevated gas temperatures. The recent computational fluid dynamical model of Strypi-XI flowfields (Ref 12) shows such a contact surface extending from Antares (which puts out  $\sim 4 \times$  as much gas per unit time as Star 27) when its velocity was 1.97 km/s, with  $\sim 1000\text{K} - 3000\text{K}$  kinetic temperatures extending over the expected  $\sim 4$  m contact surface, where the total densities of the background and continuous-explosion gases are each a few times ambient.

All of the nonhomopolar principal combustion products of the Star 27 thruster, as well as virtually all of those molecules that would result from reactions with (and of) the atmosphere's major species, have fundamental vibrational band systems that extend to wavelengths at which the PtSi camera system is sensitive. Its relative response to these infrared features, rotationally broadened to reflect the expected kinetic temperatures in the contact surface, is listed in Table 4. (Rovibrational bands normally considered to be strongly absorbed by the atmosphere's water vapor and carbon dioxide would be partially transmitted to AMOS.) Table 4 also lists the relative abundances of the exhaust components and the radiative lifetimes of the first vibrational state of the perceivedly-principal impact excited or reaction product species, all of which (except  $\text{H}_2\text{O}$  and  $\text{CO}_2 \nu_3$ ) are of order  $1/20$  s.

With the approximation that the decrease in diffusion coefficients that would result from the increased gas density in and near the contact surface is counterbalanced by the increase associated with the higher mean temperature (and steeper gradients) there the rms molecular diffusion length in  $1/20$  s would be 15 m at the "mean" altitude of Frames A - F. The observation that the halfwidths at  $1/e$ -maximum brightness are marginally smaller--near 10 m (Fig's. 24 and 29)--suggests that either a species with somewhat less than this "average" upper-state lifetime is the principal source of the SWIR radiation, or that collisional quenching

Table 4. Candidate infrared radiation-producing exhaust molecules

| <u>Exhaust Species</u> | <u>Mole Fraction of Gas</u> | <u>PtSi Camera System Sensitivity*</u>  | <u>Radiative Lifetime, s<sup>†</sup></u> |
|------------------------|-----------------------------|---|--|
| H <sub>2</sub>         | 0.277                       | OH 0.18                                 | 0.054                                    |
| CO                     | 0.227                       | CO 0.05                                 | 0.030                                    |
| HCl                    | 0.181                       | HCl 0.38<br>OH 0.18                     | 0.029<br>0.054                           |
| H <sub>2</sub> O       | 0.187                       | $\nu_3$ 0.1<br>$\nu_2$ 0.005<br>OH 0.18 | 0.012<br>0.044<br>0.054                  |
| N <sub>2</sub>         | 0.092                       | NO 0.005<br>NO (2, 0) 0.2               | 0.075<br>0.038                           |
| CO <sub>2</sub>        | 0.085                       | $\nu_3$ 0.02<br>CO 0.05                 | 0.0024<br>0.030                          |

\* Referred to the response characteristic in Fig. 23b and mean value in the text to provide an indication of the absolute system sensitivity; assumes 2000K rotational temperature of the vibrational fundamental band of the species identified (except NO 2, 0); refer also to Fig. 33.

† Of the first vibrational state of the molecule identified in the third column.

of the vibrationally-excited molecules as they diffuse into the cooler gas layers is limiting their transport. This latter depopulation would of course require correspondingly increased rates of excitation(s) to produce the measured infrared photon emission rates.

**Excitation Processes.** We consider the hypotheses that this radiation arises from reactions involving

- the infrared-active minor species permanently present at the altitudes of the Bow Shock 2 (Fig. 21), for example NO and CO<sub>2</sub>;
- only the major atmospheric constituents N<sub>2</sub> - O<sub>2</sub> - O, whose principal SWIR-exciting reaction in the expected temperature range is  $N_2 + O \rightarrow NO^+ + N$ ;
- only combustion products, those major components listed in Table 4 and/or any of the several lower-concentration chemical species; or
- both these exhaust gases and the ambient atoms and molecules.

The first two types of processes can be dismissed out-of-hand on energetics grounds. As the densities of the minor atmospheric molecules are all  $\leq 10^8/\text{cm}^3$  and the total density is  $\leq 10^{13}/\text{cm}^3$ , to achieve  $10^{12.5}$  excitations per  $\text{cm}^3\text{-s}$  would require a population rate coefficient greater than  $10^{-9} \text{ cm}^3/\text{s}$ , which far exceeds the maximum physically attainable. (Furthermore the necessary time between excitations of the minor species would be very much shorter than the radiative lifetimes of their upper vibrational states.) As for the major ambient species, the rate coefficients in Table 5 for the above-mentioned ( $\sim 3\frac{1}{2}$  eV endothermic) reactions forming NO in its first or second vibrational state are at least two orders of magnitude too low at the expected, or even substantially higher, maximum temperatures in the contact surface to produce the measured rates of emission of SWIR photons. In addition not enough new ground-state nitric oxide or other radiative molecules could be chemically produced within the time scale of the AMOS measurements to result in significant thermal infrared emission. In view of the absence of other candidate such atom-interchange reactions (energetic collisions of course cannot lead to vibrational radiation from homopolar N<sub>2</sub> and O<sub>2</sub> molecules), we may conclude that heating of the major species present in lower-thermospheric air by the energetic exhaust gas also fails to contribute substantially to the outer SWIR glow.

The estimates in Table 5 of rate coefficients for the latter two above processes refer to vibrational population of exhaust molecules by direct impact (in single-mode, single-quantum  $T \rightarrow V$  processes), and formation of new species in excited states by exchange with the high atmosphere's reactive and relatively abundant oxygen atoms. All these chemical reactions that could result in population of upper states of the product molecule are endothermic, and thus like the excitative collisions of reheated exhaust (for example H<sub>2</sub>O with H<sub>2</sub>O or N<sub>2</sub> exciting its bending or stretch modes) their rate coefficients increase with temperature over the expected

Table 5. Vibrational excitation coefficients ( $\text{cm}^3 \text{s}^{-1} \text{ molecule}^{-1}$ ) between major exhaust and atmosphere constituents at 2500K

| T → V | Collision§       | Energy<br>(eV) ‡ | H <sub>2</sub> | H <sub>2</sub> O      | HCl                   | CO                                     | CO <sub>2</sub>       | N <sub>2</sub>        | O                           |
|-------|------------------|------------------|----------------|-----------------------|-----------------------|--|-----------------------|-----------------------|-----------------------------|
|       | H <sub>2</sub> O |                  |                |                       |                       |  |                       |                       |                             |
|       | $\nu_2$          | 0.20             |                | $2.4 \times 10^{-11}$ |                       |  |                       | $1.2 \times 10^{-12}$ | $5.0 \times 10^{-12}^{***}$ |
|       | $\nu_1, \nu_3$   | 0.45             |                | $7.8 \times 10^{-13}$ |                       |  |                       | $4.5 \times 10^{-14}$ | $1.6 \times 10^{-13}^{***}$ |
|       | HCl              |                  |                |                       |                       |  |                       |                       |                             |
|       | ( $\nu=1$ )      | 0.37             |                |                       | $5.4 \times 10^{-13}$ | $1.8 \times 10^{-13}$                  |                       | $1.8 \times 10^{-14}$ | $5.3 \times 10^{-15}$       |
|       | CO               |                  |                |                       |                       |  |                       |                       |                             |
|       | ( $\nu=1$ )      | 0.27             |                |                       |                       | $3.4 \times 10^{-15} \dagger \ddagger$ |                       | $1.5 \times 10^{-12}$ |                             |
|       | CO <sub>2</sub>  |                  |                |                       |                       |  |                       |                       |                             |
|       | $\nu_3$          | 0.28             |                | $2.5 \times 10^{-13}$ | $3.6 \times 10^{-14}$ | $6.0 \times 10^{-15}$                  | $2.6 \times 10^{-15}$ | $9.0 \times 10^{-16}$ | $1.7 \times 10^{-12}^{***}$ |

| Interchange<br>Reaction | CO                               | Energy* | CO <sub>2</sub>       | Energy* | H**                 | Energy* | O               | Energy* | †                     |
|-------------------------|----------------------------------|---------|-----------------------|---------|---------------------|---------|-----------------|---------|-----------------------|
| H <sub>2</sub>          |                                  |         |                       |         |                     |         |                 |         |                       |
|                         | HCO                              | 3.7     | CO + H <sub>2</sub> O | 0.45    |                     |         | OH              | 0.09    | $6.9 \times 10^{-13}$ |
| HCl                     |                                  |         |                       |         |                     |         |                 |         |                       |
|                         | HCO                              | 3.7     | OH                    | 5.5     | H <sub>2</sub> + Cl | -0.05   | OH              | 0.04    | $3.1 \times 10^{-13}$ |
| H <sub>2</sub> O        |                                  |         |                       |         |                     |         |                 |         |                       |
|                         | CO <sub>2</sub> + H <sub>2</sub> | -0.45   |                       |         | H <sub>2</sub> + OH | 0.61    | OH              | 0.62    | $6.9 \times 10^{-13}$ |
| CO                      |                                  |         |                       |         | HCO                 | -0.75   | CO <sub>2</sub> | 5.45    | $5.0 \times 10^{-15}$ |
| CO <sub>2</sub>         |                                  |         |                       |         | CO + OH             | 1.06    | CO              | 0.33    | $3.3 \times 10^{-16}$ |
| N <sub>2</sub>          |                                  |         |                       |         | NH                  | 5.3     | NO ( $\nu=1$ )  | 3.26    | $1.1 \times 10^{-17}$ |
|                         |                                  |         |                       |         |                     |         | NO ( $\nu=2$ )  | 3.50    | $3.6 \times 10^{-18}$ |

§ All rates except those otherwise indicated are calculated from [experimentally measured rate coefficient for the inverse process] · [exponential Boltzmann factor]. Data from several standard sources.

† Of the first vibrational state. ‡‡ From a calculated quenching rate.

\* Above the ground configuration. \*\* Possible minor combustion product species. \*\*\* From a measured excitation rate.

†† To first vibrational state. Adopts extrapolated laboratory rate coefficient for the reaction with O reduced by the Boltzmann factor for populating the first vibrational state of the product species indicated, except CO<sub>2</sub> + O.

range. Note that the last two types of process overlap, in that (for example)  $\text{H}_2\text{O}$  molecules in the combustion gas could be excited by impact on  $\text{N}_2$  molecules also present in the exhaust or in the background atmospheric gas.

These estimates of reaction rates were made from standard data sources, including the recent survey in Ref 44; the laboratory database on excitative processes is sparse, and theory provides only limited guidance. All except the few so indicated involve application of the measured rate coefficient for the reverse or depopulating process, or extrapolation of the laboratory rate for the forward reaction that produces the new species primarily in its ground state. Each of the former rates has been reduced by the Boltzmann factor for "mean" 2500K translational temperature in the contact surface, and the latter also by including the energy threshold corresponding to the upper state. While such a direct application of the backwards rate coefficient violates the principle of microscopic reversibility in that it fails to balance in detail the (generally poorly known) resulting distributions in velocity and internal-excitation states, it remains the method of choice in the absence of other information. Similarly, far extrapolations of rate data from laboratory chamber ("bulb") or molecular beam experiments are notoriously unreliable (among other reasons, they account poorly for initial vibrational excitation of the reactants). The considerable uncertainty in these rate coefficients--those omitted are altogether unknown--hampers assessment of the contributions of individual excitation processes to the PtSi camera signal.

The responses of this imaging system listed in Table 4 are relative to its mean radiance sensitivity that we estimated above,  $10^{-4-1/3} \text{ W/cm}^2 \text{ sr}$ . They were calculated for 2000K rotational temperature as illustrated in the example comparisons of exoatmospheric rovibrational band profiles with the transmitted and quantum efficiency-normalized profiles, Fig. 33. (As the vibrationally-excited molecules in the contact surface on average experience several elastic collisions before radiating, their rotational temperature would be near the local kinetic temperature.) Error from these camera response factors is expected to be substantially smaller than from the uncertainties in the rate coefficients in Table 5.

**Radiating Species.** The relative infrared signal from each process in Table 5 would then be the product

$$\begin{aligned} & (\text{Mol fraction of reacting species in the exhaust}) \times \\ & (\text{Mol fraction of its collision partner}) \times \\ & (\text{Reaction rate coefficient}) \times \\ & (\text{Camera system response [from Table 4]}). \end{aligned}$$

The fractions of  $\text{N}_2$  and  $\text{O}$  in air at the altitudes where the Star 27 operated are to a satisfactory approximation 0.75 and 0.2. We neglect the effect of radiative lifetime on the SWIR

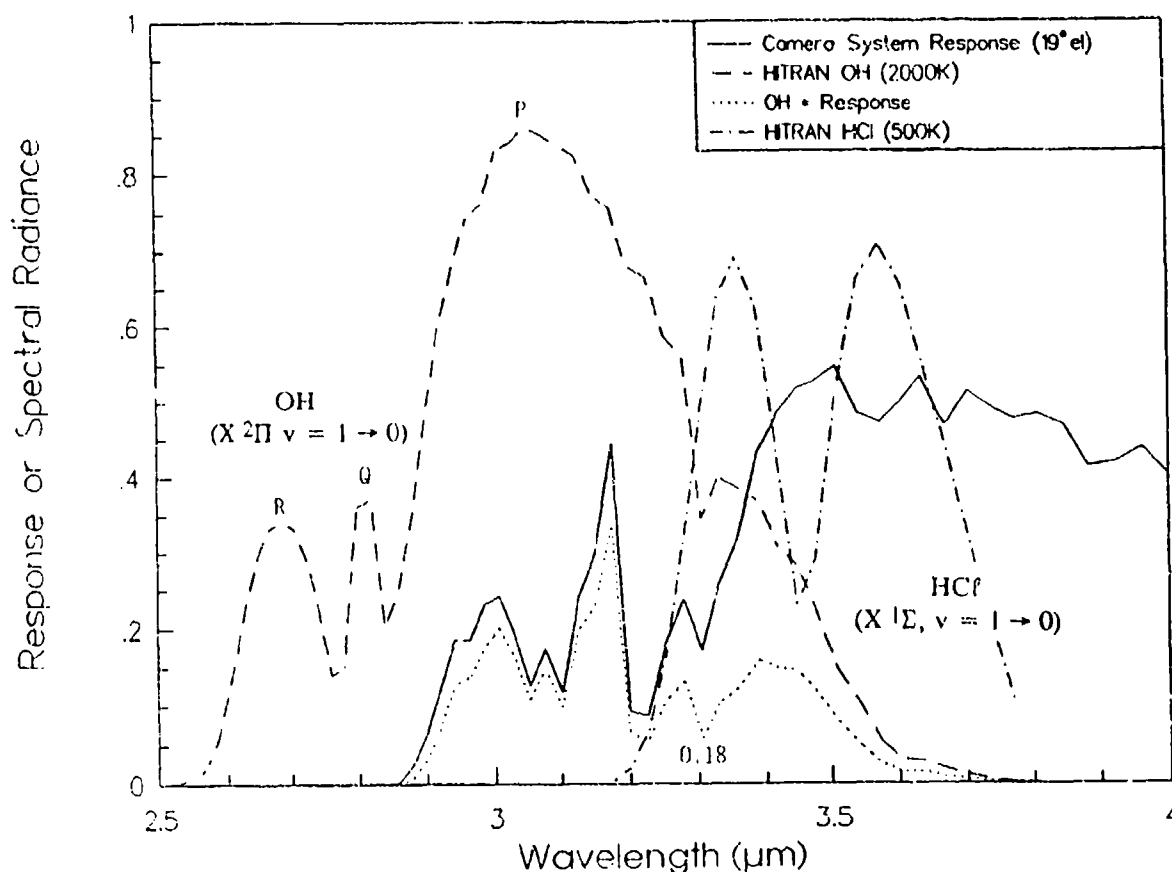


Figure 33. Response of the PtSi camera-plus-intervening atmosphere (from Fig. 23b) to two of the candidate vibrational emission bands.

brightnesses, as the lifetimes of the candidate infrared-active species are comparable and, as shown above, broadly consistent with the observed width of the outer glow.

A comparison of the signals resulting from the  $T \rightarrow V$  (translational converting to vibrational energy) and oxygen atom interchange processes listed in Table 5 identifies no clearly dominant source of the outer-glow emission. Further, with adoption of  $3 \times 10^{12} \text{ cm}^{-3}$  as the total density of each of the two gases (which follows from the hydrodynamics of the exhaust (Ref's 18 and 22)), the individual absolute volume emission rates predicted are at least some  $1\frac{1}{2}$  orders of magnitude lower than those derived from the PtSi camera measurements. Increasing the mean temperature of the reacting gases from 2500K to 3500K increases most of the excitative rate coefficients by only a modest factor (except of  $\text{N}_2 + \text{O} \rightarrow \text{NO}^\dagger$ , whose absolute reaction rate still remains far too low to produce appreciable signal), and with the concurrent broadenings of band profile taken into account fails to bring out a viable single excitation mechanism. Additionally, unrealistic rate coefficients for reactions involving the minor combustion products would be needed to produce the high mean infrared yields that are observed.

On the basis of the input data in Tables 4 and 5,  $T \rightarrow V$  collisions with atomic oxygen and among exhaust species (in particular  $H_2O$  on  $H_2O$ ,  $HCl$  on  $HCl$ ), and the atom exchange reactions that lead to  $OH$  ( $X, v = 1$ ), produce roughly comparable numbers of counted SWIR photons. The sum of emissions from the about-10 such favored processes, at a somewhat higher contact-surface temperature and gas density than we have estimated, could bring the radiances of the outer glow within the expected uncertainty of the response of the AMOS PtSi camera.

### Hydrodynamics

Computational fluid-dynamical models, such as that in Ref 12 for the conditions of Bow Shock 2's thruster engines and those presented and referenced in Ref 22, provide theoretical "snapshots" of exhaust flowfields at discrete spacecraft velocities and air densities. In addition the earlier-developed analytical similarity solutions for pulsed, initially-isotropic point or line explosions in the atmosphere that we applied in Section 1 give physical insight that is effective in scaling these experiment data. "Similarity" (as already mentioned) refers to the assumption--or constraint--that the quantities describing the gas flow have the same dependence on time and position. While this simplification would not produce predictions as accurate as those from numerical integrations of the equations of motion of the explosion and background gas, its application has been shown to give reasonable agreement with measurements on particle and wave transport from explosives whose gas velocities are several times the ambient sound speed (producing "strong" shocks), as is indeed the case for the solid-propellant engines.

Pending availability of the detailed numerical calculations for the Star 27 burn, we briefly compare the results of similarity calculations for uniformly-loaded explosive cylinders long compared with the radial extent of the flow (Ref's 26,27) with the observations here of the continuous injection of high-temperature, high directed-velocity combustion gases along the Strypi-XI trajectory. Since the latter process is intermediate between the former and a series of spherically-symmetric explosions, a fully quantitative fit to the transport data in the images is not expected. As alluded to above and in Section 1 and detailed in Ref's 18 and 26, a Rankine-Hugoniot shock is considered to form at approximately fifteen ambient mean free paths from the explosion; the even earlier-developing  $\sim 2$  mean free paths-thick contact surface follows the scaling outlined below out to a radial distance  $0.2 \times [(\text{energy per unit length in the explosion gas})/(\text{pressure of the ambient gas})]^{1/2}$ . (Should the former characteristic dimension exceed the latter, as in for example outgassing from--or even operation of attitude-controlling rocket motors on--spacecraft at low earth orbital altitudes, the released gas in effect diffuses outward without coherently developing a peripheral shell of swept out air that separates it from



the background atmosphere.) Where the Star 27 thruster (whose energy output per unit length is defined immediately below) is producing detectable SWIR glow the ambient mean free paths are between 1 and 3 m, and the radial distances out to which these similarity calculations are valid remain within <15% of 270 m. In consequence to the extent that the theory for simultaneous explosions into undisturbed air applies to the rocket engine burn an "air shock" would form within the AMOS camera fields illustrated in Fig. 15, and furthermore the predictions of the theory extend to beyond these fields.

Similarity theory for cylindrical explosions predicts that the velocity of the contact surface is initially constant with the value

$$[(2/\alpha\alpha') \cdot (\text{energy relative to the atmosphere per unit mass of released gas})]^{1/2}.$$

The "geometry" factor  $\alpha$  (Ref's 27,28 and ref's therein) is the ratio of the average kinetic energy of gas parcels in the explosion volume to this energy in parcels in the expansion front, and is 1/2 for fully isotropic cylindrical explosions into uniform-density air (it is 3/5 for spherical explosions, for which the exponent is 2/5). We have introduced here a further multiplier  $\alpha'$ , expected to be less than 1 and not necessarily constant over the Strypi-XI trajectory, to take into account the anisotropy and partially-serial nature of the energy output from the rocket engine.

The mean total energy of the exhaust molecules at the Star 27 exit plane is  $[1/2 m (v_s - 2.93)^2 + k 1507/(\gamma - 1)]$ , where their average mass  $m$  is 20 atomic units,  $\gamma$  is the calculated ratio of specific heats of the gas (1.292), and  $k$  is the Boltzmann constant (as noted above the calculated exhaust-gas temperature is 1507K). This initial outward velocity would then be  $3.0/\sqrt{\alpha'}$  km/s in Frame A where the SWIR glow first becomes detectable, increasing to  $3.3/\sqrt{\alpha'}$  and  $4.2/\sqrt{\alpha'}$  km/s in Frames D and F respectively. As the exhaust gas incorporates an increasing relative mass of ambient air, the radial displacement approaches

$$\{(8/\pi\alpha\alpha') \cdot (\gamma - 1)\gamma^{-1} \cdot [\text{total energy input per unit pathlength}]/\rho\}^{1/4} \times (\text{time})^{1/2}.$$

That is, the radial distance from the explosion then increases as  $\sqrt{(\text{time})}$ , rather than linearly as when the mass (and energy) of swept-up air was much less than that of exhaust gas. The term in square brackets, which is the mean total energy per molecule multiplied by (number of molecules exhausted per unit time)/ $v_s$ , in practice remains within 5% of 15 cal/cm between Frames A and E.

Since the time scale in the images formed while the AMOS camera tracks on the Strypi-XI body is as mentioned not uniquely defined, some ambiguity exists in interpreting these simple scaling relationships. In Fig. 31 we have plotted the predicted radial positions of the contact surface for the conditions of Frame D with the assumption--applicable just outside this mixing region--that the free-stream time applies in calculating its outward transport, and with  $\alpha' = 0.5$ . Its so-defined initial velocity is roughly 50% greater than predicted from

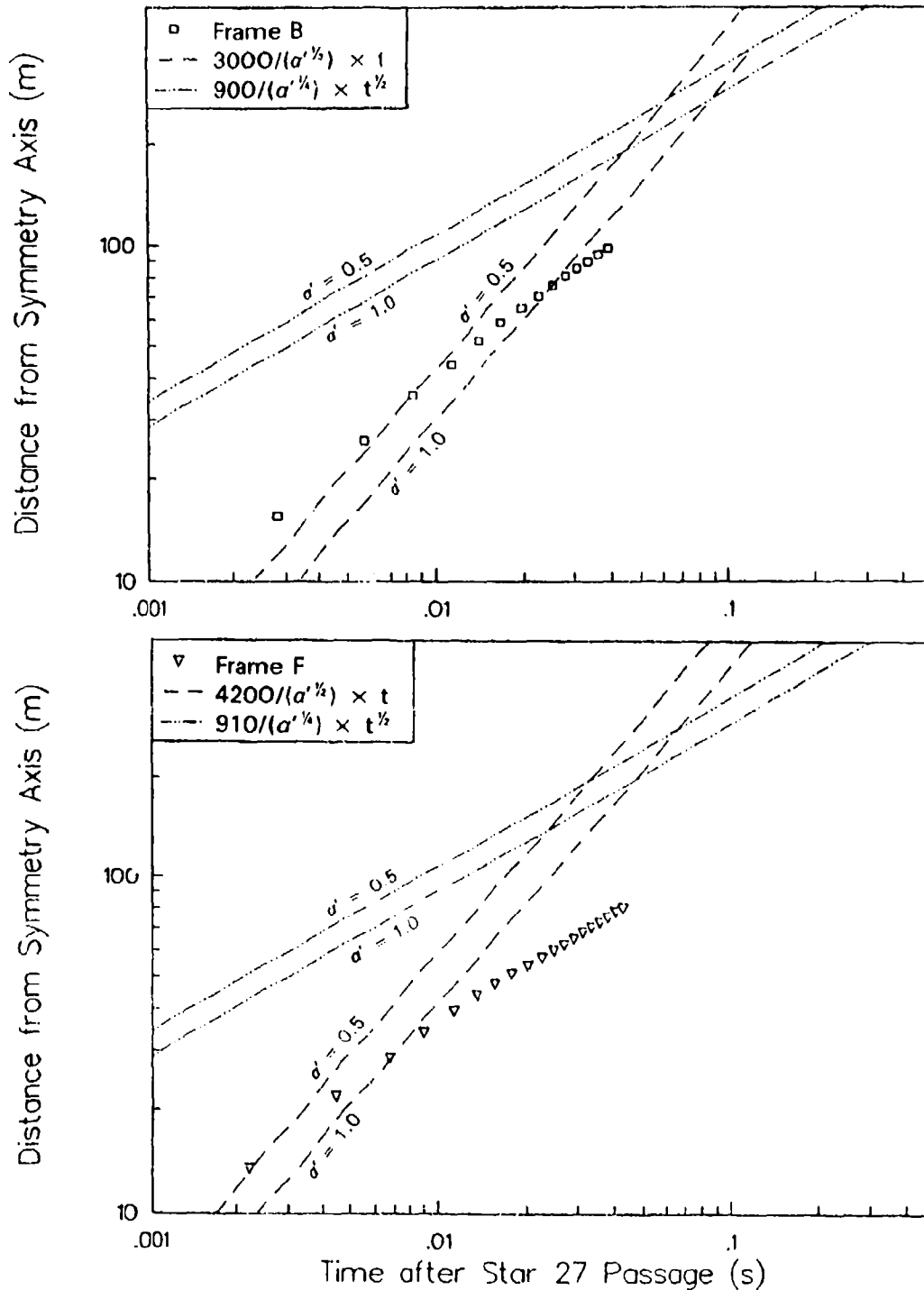


Figure 34. Distance to the outer infrared radiance maxima compared with the theoretical (linear with time) initial expansion and to the later  $\sqrt{\text{time}}$  behavior. With  $\alpha' = 1$  the calculated initial expansion rates for the conditions of Frames B and F are 3000 m/s and 4200 m/s. The later-time theoretical expansion constant (curly bracketed expression in the text) is 900 m/s<sup>1/2</sup> for Frame B and 910 m/s<sup>1/2</sup> for Frame F.

similarity. The displacements during the later period indeed have the predicted functional dependence on  $\sqrt{(\text{time})}$ , but with this  $\alpha'$  about 50% lower absolute values than similarity predicts. However, the weak dependence on  $(\text{power output})/(\rho v_s)$  in the above radial displacement expression is semiquantitatively consistent with the very slow decrease along the flight path of radial displacements at a fixed free-stream time, evidenced in Fig's. 27 and 28. This function is plotted in Fig. 31.

Interpreting the initial time scale as that along the trajectory proper reduces these initial expansion velocities. However doing so also increases the discrepancy between the later outward transport of the region that we are interpreting as the contact surface and the above prediction for explosions that simultaneously and isotropically inject energetic gas from a  $\geq 250$  m-long straight line.

### Concluding Comments

These similarity-solution arguments, while suitable for scaling the radii at which pressure-equilibration taken place (as observed in Section 1), predict the general course but not the magnitude of the radial growth of the "bow shock" of its exhaust gases in the first 1/10 s after passage of the Star 27 rocket motor. The contact surface between the combustion gas and the cold ambient gas at  $\sim 110$  km altitude initially moves out at a constant velocity, and then as more atmosphere is incorporated and heated its displacement increases as expected with  $\sqrt{(\text{time})}$  over the full lengths of contact surfaces within the PtSi camera field (see in particular Fig. 28b). Unlike for static explosions at high altitudes both the zero point and scale of this "time" is ill-defined from the image data, which may underlie the lack of absolute agreement. Another reason, qualitatively speaking, is that the exhaust from the  $\sim \pi/10$ -steradian solid angle engine nozzle encounters previously released gas that is much denser than the atmosphere and, when the SWIR glow appears, is moving relative to the direction of the engine, and so is given additional initial transverse velocity.

The molecular species primarily responsible for the relatively intense short wavelength infrared radiation is not yet identified. We anticipate that the temperature and density distributions predicted by the computational fluid dynamical model (Ref 12) will apply in refining the excitative-reaction rates in Table 4, and so provide guidance for isolating the dominant process(es). On the basis of past experience we provisionally judge the most plausible candidate to be impact excitation of  $\text{H}_2\text{O}$  to its 010 and 001 vibrational states, more photons from which reach the PtSi camera as rotational development broadens,  $\nu_2$  and  $\nu_3$  the emission bands. These detailed calculations are also expected to identify the quantitative, or even qualitative, differences in the flowfield that result in above-threshold SWIR radiances from the "classical" contact surface only when the velocity of the Strypi-XI exceeds by the

ambient sound speed the calculated directed velocity of the exhaust gases at the exit plane of the solid rocket motor.

An estimate of the average transmitted IR power from the entire outer-glow bolume during Frames B-C-D is 20 kW, which is 0.03% of the total Star 27 thruster power (62 MW). If this radiation is rotationally-broadened  $\text{H}_2\text{O } \nu_1$  and  $\nu_2$ , which is strongly absorbed by the atmosphere and produces the relative sensor response in Table 4, the exoatmospheric SWIR yield rate is comparable with the visible and IR yield rates we derived in Section 1.

Figures 24 - 29 quantify the development and surface brightnesses of this outer glow as taken from the PtSi camera images, and Fig's. 30 - 32 plot the data against experiment parameters having physically reasonable interpretations. The concurrent increase of density and velocity of the freestream air over the experiment period hampers extraction of heuristic descriptors of these radiances and dimensions, and the engine thrust appears to be a further experiment variable. (The radial extent and radiances of the outer SWIR glow appear to be varying faster than linearly with this thrust, that is, with the rate of output of high directed-and internal-energy gases.) For better development of empirical scaling rules for the outer SWIR glow--desirable in view of the inherent unreliability of *ab initio* theory--further Bow Shock experiments should be designed to separate the effects of vehicle velocity, air density, and engine performance factors.

In sum, it is clear that the more or less hollow infrared-radiating region in Fig. 15 is the bow "shock" not of the hypersonic hard body of the Strypi-XI (a phenomenon focused on by the early experiment planning), but of its engine exhaust gases when their velocity along the trajectory exceeds the local sound speed. We associate the glow with the contact surface known to develop from explosions in air when the energy input exceeds the local energy density by some modest factor. The Figures and supporting phenomenology arguments in this Section characterize the infrared signature of this outer glow--an absolute SWIR radiance, judged to be accurate to within an order of magnitude, in Fig. 29-- and provide a basis for heuristic scaling to other vehicle velocities and ambient air densities.

## SECTION 3

### LABORATORY ION-NEUTRAL REACTION EXPERIMENTS

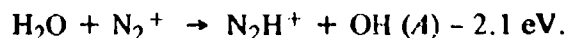
#### Overview

PhotoMetrics provided support to the Spacecraft Interactions Branch (WSSI) Chemistry Laboratory of AF Phillips Laboratory in three major projects: measurements and analysis of hydroxyl chemiluminescence excited in ion-neutral reactions, measurements of rates of reactions of hydrazine with atomic oxygen and other ions, and related experiments made possible by a recently-installed charge coupled device optical detector. This continuing effort is briefly described here.

#### OH $A^2\Sigma^+ \rightarrow X^2\Pi$ Chemiluminescence

Ultraviolet emissions resulting from OH  $A^2\Sigma^+ \rightarrow X^2\Pi$  transitions contribute to optical contamination of the low-earth orbital environment. The upper state of the hydroxyl radical can be excited in atom-transferring collisions of high-velocity  $H_2O$  molecules on the neutral O atoms of the atmosphere (Ref's 3,4,45), and also in part from the interaction of water vapor with ambient  $N_2^+$  ions, which at 250 km altitude is present in concentrations of about  $10^3 \text{ cm}^{-3}$ . This vapor is released through outgassing from space vehicle surfaces (Ref 46), as a combustion product of aspect control engine firings (Ref 45), and in connection with ventings of excess liquid water (Ref's 2,7).

Electronically excited hydroxyl can be produced in the endothermic ion-neutral reaction



The kinetic energy available in the center of mass of this system is 3.5 eV at the orbital velocity of  $7.8 \text{ km s}^{-1}$ , the mean speed relative to the static atmosphere of  $H_2O$  molecules both outgassed and evolved from vented water. The collision energy of engine-exhaust  $H_2O$  depends on the angle between the trajectory and firing-axis vectors, varying between 1.1 eV for retrograde firings and 7.3 eV when the exhaust is directed into ram. Thus sufficient translation energy is available in these ion-neutral collisions to access the OH (A) state both in impacts of outgassed/vented water and water exhausted from the onboard control engines in directions other than those near the spacecraft's wake.

Using the PL/WSSI double mass spectrometer system (DMS, Ref 47), we measured and analyzed of the ultraviolet emissions from this reaction and from the analogous reaction of  $Ar^+$  with  $H_2O$ . The radiations, spectrally resolved with an Optical Multichannel Analyzer (OMA), appear above 5 eV center of mass energy. Simulations of the spectra have shown that the electronically excited OH is formed by two dynamic pathways, the dominant one

producing hydroxyl that is vibrationally and rotationally excited. Emissions were observed from OH (*A*) produced in both the  $v = 0$  and  $v = 1$  levels; the electronic bands from higher vibrational states were not present, possibly due to their pre-dissociation (Ref's 48,49). The rotational excitation corresponds to a Boltzmann distribution with a characteristic temperature of 1000K at 6 eV collision energy and 3400K at 19 eV collision energy, as shown in Fig. 34.

This pathway consists of a two step reaction. First, charge transfer occurs between  $N_2^+$  (or  $Ar^+$ ) and  $H_2O$ , resulting in  $H_2O^+$  that is known to be both electronically excited and highly vibrationally excited ( $v = 12 - 16$ ) in the  $\nu_2$  bending mode (Ref 50); and second, a proton transfer occurs between the  $H_2O^+$  and  $N_2$  (or  $Ar$ ), with the  $H_2O^+$  vibrational angular momentum resulting in high rotational angular momentum of the OH fragment. Similar vibrational to rotational energy transfer has been found to take place in experiments with neutral species that selectively excite the  $\nu_2$  bending mode of  $H_2O$ , and then cleave one of the O-H bonds resulting in a rotationally hot hydroxyl radical (Ref's 51, 52).

The second dynamical pathway produces vibrationally and rotationally thermal OH ( $v = 0$ , rotational temperature 300K). This path requires a small impact parameter stripping of a hydrogen atom by the  $N_2^+$  (or  $Ar^+$ ), and accounts for  $\leq 30\%$  of the total ultraviolet emission from OH over most of the experiment conditions.

(A description of this work was prepared for the journal literature (Ref 53), and was also presented at an international conference (Ref 54).)

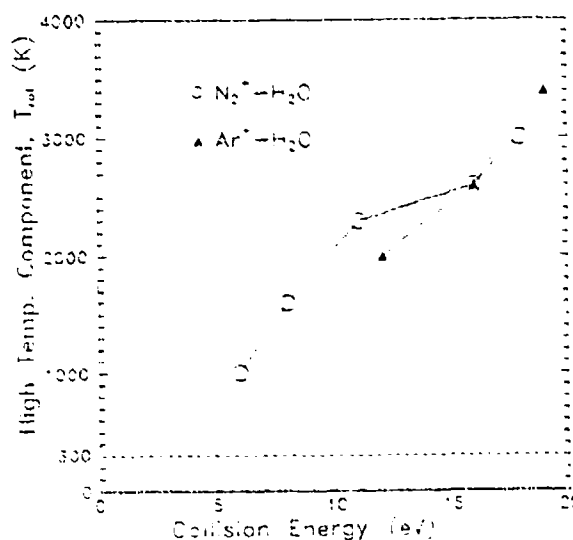
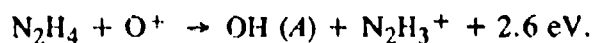


Figure 34. Dependence of the rotational temperature ( $T_{rot}$ ) on collision energy for the high temperature component of the two-component simulation required to simulate the OH *A*  $\rightarrow$  X chemiluminescence spectra.

### Reactions of $N_2H_4$ with $O^+$

Hydrazine ( $N_2H_4$ ), which with its monomethyl and dimethyl derivatives is used as fuel in liquid-bipropellant thruster rocket engines, is a further source of optical contamination. Its reactions with the principal ambient ion  $O^+$  produce ultraviolet emissions resulting from both the above-mentioned  $OH A^2\Sigma^+ \rightarrow X^2\Pi$  and  $NH A^3\Pi_i \rightarrow X^3\Sigma^-$  transitions. Formation of electronically excited OH is exothermic:



The OH emission intensity is found to decrease as the collision energy is increased over the range 4 – 50 eV, consistent with the decreasing total cross section for this reaction. Formation of electronically excited NH is in contrast endothermic:



The NH emission intensity is found to increase as the collision energy increases, as is fairly typical for endothermic reactions.

The reaction cross sections and kinetic energy of the product ions were also measured for collisions of  $N_2H_4$  with  $Kr^+$ ,  $Ar^+$ ,  $CO^+$ , and  $CO_2^+$ . In all cases more than one product ion type was observed, consistent with the large exothermicity of the basic charge transfer process for all of these collision pairs (the minimum exothermicity is 6.0 eV, for  $O^+$ ). In addition the distributions of product ions from reactions of hydrazine with atomic ions were markedly different than from the two molecular ions.  $N_2H_3^+$  (as in the first reaction above) was the dominant product from the former process, with a reaction cross-section 5 – 10 times larger than that resulting in the simple charge transfer product ion  $N_2H_4^+$ . In reactions with the molecular primary ions, however, the cross-section for producing  $N_2H_4^+$  was comparable to (for  $CO^+$ ) or larger than (for  $CO_2^+$ ) the cross section for formation of  $N_2H_3^+$ . This qualitative difference is illustrated in Fig. 35, where the data for  $O^+$  and  $CO_2^+$  reactions are compared.

Kinetic energy measurements showed that nearly all product ions resulted dynamically from a pathway of charge transfer followed by exothermicity-driven bond cleavage. For the atomic primary ions, all of the reaction exothermicity is being channeled into internal energy of  $N_2H_4^+$ , and so is available to produce its high degree of fractionation/dissociation. The molecular primary ions, however, can share in the partitioning of the exothermicity into internal modes, and thus more non-dissociated  $N_2H_4^+$  survives. (A journal article describing this work in detail (Ref 55) was prepared and published.)

### Similar Experiments with a Charge Coupled Device Detector

We tested, installed, and used a new charge coupled device (CCD) optical detector in the WSSI DMS apparatus. In the red to near-infrared spectral region this CCD is up to an

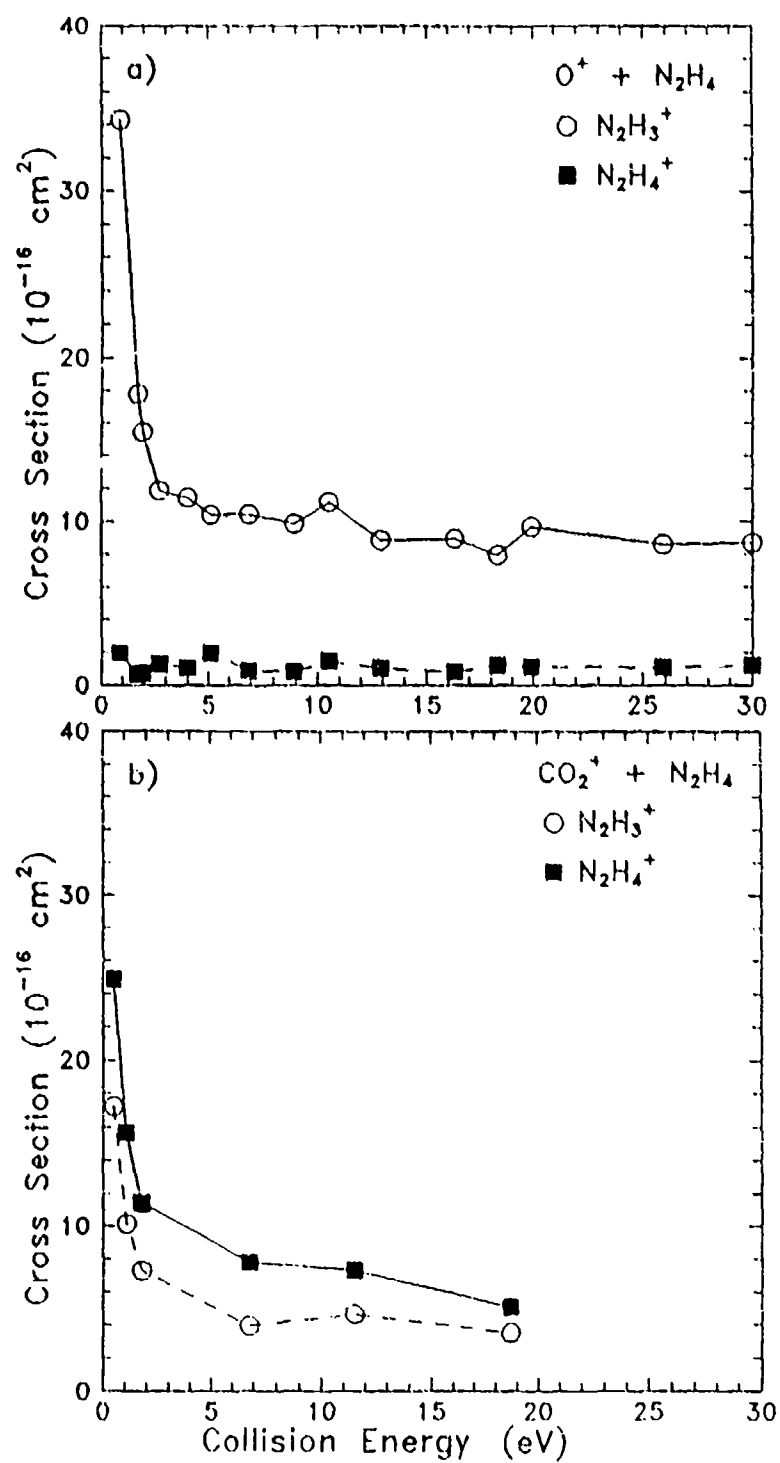
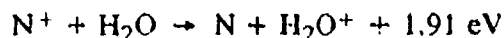


Figure 36. Collision energy dependence of the reaction cross sections for the production of  $N_2H_3^+$  and  $N_2H_4^+$  in collisions of (a)  $O^+ + N_2H_4$  and (b)  $CO_2^+ + N_2H_4$ .



order of magnitude more sensitive than the aforementioned previously-employed OMA, as shown in Fig. 36. The CCD image plane has the further throughput advantage of operating at a (nearly) 100%-on duty cycle, while the OMA is restricted to a 50%-on duty cycle.

Measurement of the optical emissions from the exothermic charge transfer reaction



requires very high sensitivity to the resulting red and near-infrared photons. Although the energetics of this process favors formation of electronically and vibrationally excited  $\text{H}_2\text{O}^+$  ( $\tilde{A}^2A_1$ ,  $\nu_2$  with  $v \approx 9$ ), previous experiments using the OMA had not detected the expected  $\text{H}_2\text{O}^+$  emissions at wavelengths near 650 nm. At a center of mass energy of  $\sim 50$  eV, no  $\text{H}_2\text{O}^+ \tilde{A} \rightarrow \tilde{X}$  emissions were detectable in measurements with the CCD, thus establishing an upper limit to the cross-section of the reaction forming  $\tilde{A}$  state  $\text{H}_2\text{O}^+$  of  $1 \times 10^{-17} \text{ cm}^2$  at this energy. (Emissions have been observed at 1125 eV, where the collision process may be considered similar to impact excitation by high energy electrons or other charged particles (Ref 50).) These recent data support our previous report (Ref 56) that the above reaction is strongly governed by conservation of electronic orbital angular momentum, which forbids formation of the  $\tilde{A}$  state of  $\text{H}_2\text{O}^+$ . Instead the exothermicity is expected to be partitioned into internal excitation (vibrational, rotational) of the  $\text{H}_2\text{O}^+ \tilde{X}^2B_1$  ground electronic state.

We also performed preliminary experiments using the CCD to measure the intensities of ultraviolet and visible emissions from reactions of ions with methylhydrazine ( $\text{N}_2\text{H}_3\text{CH}_3$ ). Radiation believed to be attributable to electronically excited NH and CH were observed in low energy collisions with  $\text{Ar}^+$ . In addition NH  $\tilde{A} \rightarrow \tilde{X}$  and CH  $\tilde{A} \rightarrow \tilde{X}$  emissions are readily observed in high center-of-mass energy (750 eV) reactions between  $\text{O}^+$  and  $\text{N}_2\text{H}_3\text{CH}_3$ , and evidence was found for OH  $\tilde{A} \rightarrow \tilde{X}$  emissions at low collision energies of these reactants.

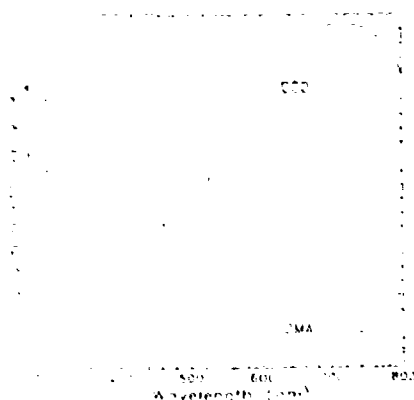


Figure 37. Wavelength dependence of quantum efficiencies for the CCD (solid line) and OMA (dashed line) detectors.

## REFERENCES

1. I. L. Kofsky, D. L. A. Rall, and R. B. Sluder, Measurement and Interpretation of Contaminant Radiations in the Spacecraft Environment, PL-TR-91-2174, 28 June 1991, ADA241756.
2. I. L. Kofsky, N. H. Tran, M. A. Maris, D. L. A. Rall, and C. A. Trowbridge, Photometric-Photogrammetric Analysis of Video Images of a Venting of Water from Space Shuttle Discovery, *Scientific Report No. 2*, GL-TR-90-0187, 15 June 1990, ADA233452.
3. I. L. Kofsky, N. H. Tran, M. A. Maris, and C. A. Trowbridge, Measurement of Optical Radiations in Spacecraft Environments, *Scientific Report No. 1*, GL-TR-89-0168, 15 June 1989, ADA213814.
4. I. L. Kofsky, J. L. Barrett, T. E. Brownrigg, P. J. McNicholl, N. H. Tran, and C. A. Trowbridge, Excitation and Diagnostics of Optical Contamination in the Spacecraft Environment, AFGL-TR-88-0293, 01 July 1988, ADA202429.
5. I. L. Kofsky, Excitation of N<sub>2</sub> Lyman-Birge-Hopfield bands emission by low earth-orbiting spacecraft, *Geophys. Res. Lett.* 15, 241-244, 1988.
6. E. Murad, D. J. Knecht, R. A. Viereck, C. P. Pike, I. L. Kofsky, C. A. Trowbridge, D. L. A. Rall, G. Ashley, L. Twist, J. B. Ilgin, A. Setayesh, A. T. Stair, Jr., and J. E. Blaha, Visible light emission excited by interaction of space shuttle exhaust with the atmosphere, *Geophys. Res. Lett.* 17, 2205-2208, 1990.
7. I. L. Kofsky, D. L. A. Rall, M. A. Maris, N. H. Tran, E. Murad, C. P. Pike, D. J. Knecht, R. A. Viereck, A. T. Stair, Jr., and A. Setayesh, Phenomenology of a water venting in low earth orbit, accepted for publication in *Acta Astronautica*, 1992.
8. J. A. Gardner, II, D. L. A. Rall, I. L. Kofsky, A. Setayesh, and E. Murad, Liquid dispersal study: A proposed space shuttle liquid release experiment, Paper AIAA-92-0793, 30th Aerospace Sciences Meeting, Reno NV, 6-9 Jan 1992.
9. P. W. Erdman, E. C. Zipf, P. Espy, C. Howlett, R. Loda, R. J. Collins, D. A. Levin, and G. V. Candler, Flight Measurements of Low Velocity Bow Shock Ultra-Violet Radiation, Paper AIAA 91-1410, 26th AIAA Thermophysics Conference, Honolulu HI, June 1991.
10. D. A. Levin, L. H. Caveny, D. M. Mann, R. J. Collins, C. Howlett, P. Espy, R. W. Erdman, and E. Zipf, Ultraviolet Emissions from In-flight Plume and Hardbody Flow Fields, 19th JANNAF Exhaust Plume Technology Conference, May 1991.
11. *AMOS User's Manual*, Revision 7, AERLM 1175, Avco Corp., Everett MA, May 1989.
12. G. Candler D. A. Levin, J. Brandenburg, R. J. Collins, P. W. Erdman, E. C. Zipf, and C. Howlett, Comparison of Theory with Plume Radiance Measurements from the Bow Shock Ultraviolet 2 Rocket Flight, Paper AIAA 92-0125, 30th Aerospace Sciences Meeting, Reno NV, Jan 1992.

13. P. W. Erdman, E. C. Zipf, P. Espy, C. Howlett, R. J. Collins, C. Christou, D. A. Levin, and G. V. Candler, In Situ Measurements of UV and VUV Radiation from a Rocket Plume and Re-Entry Bow Shock, Paper AIAA 92-0124, 30th Aerospace Sciences Meeting, Reno NV, Jan 1992.
14. M. Shorr and A. J. Zahringer (eds.), *Solid Rocket Technology*, Wiley, New York, p. 367, 1967.
15. A. E. Hedin, MSIS-86 thermospheric model, *J. Geophys. Res.* 92, 4649-4662, 1987.
16. H. W. Smathers, D. M. Horan, J. G. Cardon, E. R. Malaret, M. Singh, T. Sorensen, P. Laufer, M. Corson, J. A. McKay, and R. R. Strunce, Jr., Naval Research Laboratory Draft Strypi Report Ultraviolet Plume Instrument Observations from Space: Strypi Rocket Plume, 28 October 1991.
17. W. H. Warren, Jr., Documentation for the machine-readable character-coded version of the SkyMap Catalogue, NASA Report NSSDC/W DC-A-R&S, 05 July 1981.
18. G. V. Groves, Initial expansion to ambient pressure of chemical explosive releases in the upper atmosphere, *J. Geophys. Res.* 68, 3033-3047, 1963.
19. NOAA/NASA/USAF, *U. S. Standard Atmosphere, 1976*, Washington DC, p. 7, 1976.
20. D. Golomb and M. A. MacLeod, Diffusion coefficients in the upper atmosphere from chemiluminous trails, *J. Geophys. Res.* 71, 2299-2305, 1966.
21. P. A. Bernhardt, High altitude gas releases: Transition from collisionless flow to diffusive flow in a nonuniform atmosphere, *J. Geophys. Res.* 84, 4341-4354, 1979.
22. P. A. Bernhardt, B. A. Kashiwa, C. A. Tepley, and S. T. Noble, Spacelab 2 upper atmospheric modification experiment over Arecibo, I, Neutral gas dynamics, *Astrophys. Lett. Comm.* 27, 169-184, 1988.
23. R. R. O'Neil, F. Bien, D. Burt, J. A. Sandock, and A. T. Stair, Jr., Summarized results of the artificial auroral experiment, *Precede, J. Geophys. Res.* 83, 3273-3280, 1978.
24. H. S. Hoffman and G. T. Best, The initial behavior of high altitude barium releases-II. The expanding vapor cloud, *J. Am. Terr. Phys.* 36, 1475-1486, 1974.
25. N. W. Rosenberg, Chemical releases at high altitude, *Science* 152, 1017-1027, 1966.
26. H. L. Brode, Blast wave from a spherical charge, *Phys. Fluids* 2, 217-229, 1959.
27. H. L. Brode, Analysis of gas expansion in a rarefied atmosphere, *Phys. Fluids* 15, 1913-1917, 1972.
28. M. M. Klein, Similarity solution for cylindrical gas cloud in rarefied atmosphere, *Phys. Fluids* 12, 964-965, 1968.
29. T. G. Slanger and J. Black, Reaction rate measurements of  $O(^3P)$  atoms by resonance fluorescence II,  $O(^3P) + CO + M \rightarrow CO_2 + M$ ;  $M = He, Ar, N_2$ , *J. Chem. Phys.* 53, 3722-3728, 1970.

30. N. W. Rosenberg, D. Golomb, and E. F. Allen, Jr., Chemiluminescence of tri-methyl aluminum released into the upper atmosphere, *J. Geophys. Res.* 68, 5895-5898, 1963.
31. S. B. Oblath and J. L. Gole, On the continuum emissions observed upon oxidation of aluminum and its compounds, *Combustion and Flame* 37, 293-312, 1980.
32. D. Golomb and J. H. Brown, Chemiluminescence of trimethyl aluminum in active oxygen and nitrogen, *Combustion and Flame* 27, 383-389, 1976.
33. T. C. Degges and H. J. P. Smith, A High Altitude Infrared Radiance Model, AFGL-TR-77-0271, 30 Nov. 1977, ADA059242.
34. A. T. Stair, Jr., C. P. Pike, E. Murad, W. F. Denig, I. L. Kofsky, J. T. Brownrigg, P. J. McNicholl, F. D. Shepherd, W. S. Ewing, R. W. Taylor, J. B. Elgin, and G. W. Ashley, Ground-Based Imaging Observations of Space Plumes, *Proceedings of the 1989 Meeting of the IRIS Specialty Group on Targets, Backgrounds, and Discrimination*, IRIA-IRIS, Vol. 2, pp. 175-195, June 1990.
35. W. S. Ewing, F. D. Shepherd, M. M. Weeks, R. W. Taylor, G. W. Ashley, S. Hill, E. Murad, A. T. Stair, Jr., and C. P. Pike, Staring-Mode Infrared Imaging of Space Objects, *Proceedings of the 1986 Meeting of the IRIS Specialty Group on Targets, Backgrounds, and Discrimination*, IRIA-IRIS, Vol. 1, pp. 315-325, July 1987.
36. F. D. Shepherd, Jr., Silicide Infrared Camera Technology, in *Advanced Infrared Sensor Technology*, J. Besson (ed.), Proc. SPIE 395, pp. 114-118, 1983.
37. F. X. Kneizys, E. P. Shettle, W. O. Gallery, J. H. Chetwynd, Jr., L. W. Abreu, J. E. A. Selby, R. W. Fenn, and R. A. McClatchey, Atmospheric transmittance/radiance: Computer code LOWTRAN 5, AFGL-TR-80-0067, Feb 1980, ADA088215.
38. W. R. Cofer III, G. C. Pergold, E. L. Winstead, and R. A. Edahl, Space shuttle exhausted aluminum oxide: A measured particle size distribution, *J. Geophys. Res.* 96, 17,371-17,376, 1991.
39. W. Jeffrey (Institute for Defense Analyses), private communication, March 1991.
40. J. M. Mooney, F. D. Shepherd, W. S. Ewing, J. E. Murguia, and J. Silverman, Responsivity nonuniformity limited performance infrared staring cameras, *Optical Eng.* 28, 1151-1161, 1989.
41. G. V. Candler and C. Park, The computation of radiation from nonequilibrium hypersonic flows, AIAA Paper 88-2678, June 1988.
42. D. A. Levin, R. Loda, G. V. Candler, and C. Park, Theory of radiation from low velocity heated air, AIAA Paper 90-0133, 28th Aerospace Sciences Meeting, 8-11 Jan. 1990.
43. D. J. Knecht (PL/WSSI), private communication, Dec. 1991.
44. National Institute of Standards and Technology, NIST Chemical Kinetics Database, Version 1 and 2, ed. W. G. Mallard et al., Gaithersburg MD, 1989.

45. J. B. Elgin, D. C. Cooke, M. F. Tautz, and E. Murad, Modeling of atmospherically induced gas phase optical contamination from orbiting spacecraft, *J. Geophys. Res.* **95**, 12197-12108, 1990.
46. S. J. Young and R. R. Herm, Model for radiation contamination by outgassing from space platforms, *J. Spacecraft Rockets* **25**, 413-420, 1988.
47. J. A. Gardner, R. A. Dressler, R. H. Salter, and E. Murad, Laboratory study of ion-neutral collisions at suprathermal energies, Geophysics Laboratory Technical Report, GL-TR-89-0345, 1989. ADA222117
48. K. R. German, Radiative and predissociative lifetimes of the  $v' = 0, 1$ , and 2 levels of the  $A^2\Sigma^+$  state of OH and OD, *J. Chem. Phys.* **63**, 5252-5255, 1975.
49. D. E. Heard, D. R. Crosley, J. B. Jeffries, G. P. Smith, and A. Hirano, Rotational level dependence of predissociation in the  $v' = 3$  level of OH  $A^2\Sigma^+$ , *J. Chem. Phys.* **96**, 4366-4371, 1992.
50. R. A. Dressler, J. A. Gardner, R. H. Salter, and E. Murad, Luminescence measurements of  $Ar^+ + H_2O$  and  $N_2^+ + H_2O$  suprathermal charge transfer collisions: Product state distributions from  $H_2O^+ A^2A_1 \rightarrow X^2B_1$  analysis, *J. Chem. Phys.* **96**, 1062-1076, 1992.
51. A. Sinha, J. D. Thoemke, and F. F. Crim, Controlling bimolecular reactions: Mode and bond selected reaction of water with translationally excited chlorine atoms, *J. Chem. Phys.* **95**, 372-376, 1992.
52. M. J. Bronikowski, W. R. Simpson, B. Girard, and R. N. Zare, State-to state reaction dynamics:  $H + HOD$  and  $H + D_2O$ , presented at 1991 Conference on the Dynamics of Molecular Collisions, Lake George NY, 7-12 July 1991.
53. J. A. Gardner, R. A. Dressler, R. H. Salter, and E. Murad, OH  $A^2\Sigma^+ \rightarrow X^2\Pi$  Chemiluminescence measurements of  $N_2^+$ ,  $Ar^+ + H_2O$  hydrogen atom transfer reactions at suprathermal energies, *J. Chem. Phys.*, in press.
54. J. A. Gardner, R. A. Dressler, R. H. Salter, and E. Murad, Ion -  $H_2O$  reactions studied in a double mass spectrometer coupled with luminescence detection, presented at the 12th International Mass Spectrometry Conference, Amsterdam, 26-30 Aug 1991.
55. J. A. Gardner, R. A. Dressler, R. H. Salter, and E. Murad, Reactions of  $N_2H_4^+$  with  $O^+$  and other ions at suprathermal energies, *J. Phys. Chem.* **96**, 4210-4217, 1992.
56. J. A. Gardner, R. A. Dressler, R. H. Salter, and E. Murad, A laboratory study of charge transfer and hydrogen atom pickup reactions in  $N^+ - H_2O(D_2O)$  collisions at suprathermal energies, *Chem. Phys. Lett.* **181**, 5-9, 1991.